National Aeronautics and Space Administration

NASA

John F. Kennedy Space Center

2005 Annual Report

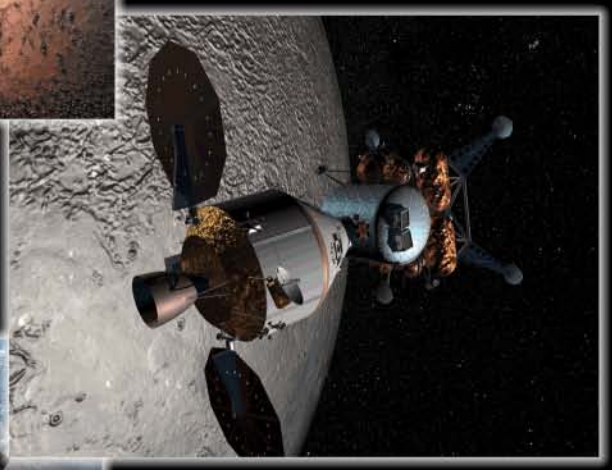

center director's discretionary fund

Center Director's Discretionary Fund 2005 Annual Report

National Aeronautics and
Space Administration

John F. Kennedy Space Center
NASA Technical Publication 2007-214731

Introduction

Bill Parsons, KSC Director

The Center Director's Discretionary Fund (CDDF) for FY 2005 has been allocated to enhance the NASA mission through innovative (high-risk) concepts that are consistent with Kennedy Space Center (KSC) strategic goals. KSC projects support a portfolio of technology development areas that are aligned with the high-priority technology needs defined by our primary stakeholders. Providing the opportunity to investigate highly creative ideas for their potential value to the Agency and commercial use plays a leading role in the arena of spaceport technology development for the future. KSC's technology development activities encompass the efforts of the entire KSC team, consisting of Government and contractor personnel working in partnership with academic institutions and commercial industries. The CDDF investment enhances KSC personnel capabilities while providing a foundation for future concepts and ensuring increased capabilities of new programs.

The FY 2005 CDDF projects were selected from the following spaceport and range technology and science areas: fluid system technologies; spaceport structures and materials; command, control, and monitoring technologies; and biological sciences (including support for environmental stewardship). Eight new projects and four continuation projects were approved for $950.5K FY 2005 CDDF.

The FY 2005 CDDF research projects involved development of the following:

- Capacitance-based moisture sensors to optimize plant growth in reduced gravity
- Commodity-free calibration methods
- Application of atmospheric plasma glow discharge to alter the surface properties of polymers for improved electrostatic dissipation characteristics
- A wipe-on, wipe-off chemical process to remove lead oxides found in paint
- A robust metabolite profiling platform for better understanding the "law" of biological regulation
- An explanation of the excavation processes that occur when a jet of gas impinges on a bed of sand
- "Smart coatings" to detect and control corrosion at an early stage to prevent further corrosion
- A model that can produce a reliable diagnosis of the quality of a software product
- The formulation of advanced materials to meet system safety needs to minimize electrostatic charges, flammability, and radiation exposure
- A lab-based instrument that uses the electro-optic Pockels effect to make static electric fields visible
- A passive volatile organic compound (VOC) cartridge to filter, identify, and quantify VOCs flowing into or emanating from plant flight experiments

KSC's CDDF Program is currently managed by the Applied Sciences Division, and comments should be directed to Orlando Melendez/KT-D at (321) 867-9407 or <Orlando.Melendez@nasa.gov>.

Contents

Contents (cont'd)

Capacitance-Based Moisture Sensing

Leaders: Mark Nurge, NASA

Other In-House Members of the Team: John Catechis, Jessica Prenger, and Oscar Monje, Ph. D., Dynamac Corp.

Initiation Year: FY 2003

Purpose

The purpose of this project is to develop capacitance-based moisture sensors (CBMSs) to provide the information needed to minimize moisture stress to plants. Improved sensors are needed for studying and understanding the mechanisms of water transfer and diffusion in reduced-gravity root zone environments and other terrestrial-based bulk-media applications. A capacitance-based bulk-moisture sensor is to be developed and tested to determine if it can address limitations of point sensors. In addition, a three-dimensional (3-D) electrical-capacitance tomography system will be developed for possible use in imaging moisture distribution in soils in reduced-gravity applications.

Background

Measurement and feedback control of moisture in plant root zones is critical to the development of healthy plants in reduced gravity. Adequate moisture content and distribution in media of space-borne nutrient delivery systems (NDSs) is required for optimal growth in plant-based life support systems. Current moisture sensor technologies suffer from interferences such as air bubbles, contact area of media, and root growth. Because most are point sensors, the measurements are localized over a small volume at the point of insertion. This makes it difficult to get an accurate representation of true moisture content and distribution in the bulk media. In addition, a network of point sensors is required, increasing the cabling, data acquisition, and calibration requirements. A bulk sensor could therefore address many of these limitations.

In space-borne applications, the microgravity substrate environment operates in a force balance between surface tension and capillary forces, making it difficult to measure and understand the distribution and availability of nutrients in plant growth experiments. Over the past few years, Kennedy Space Center has been exploring a new area in the development of a system to provide 3-D imaging of dielectric objects using an array of capacitors, referred to as electrical-capacitance tomography (ECT). This is a relatively undeveloped field in the United States (prior work has been done in England), and the hope is that it will lead to a new method for imaging objects, such as moisture in soil, using safe low-frequency electromagnetic radiation and a very inexpensive sensing system. The primary reason this has not been accomplished previously is that a very large amount of processor power is required, which has not been available until recently. Algorithmic development and electronic performance are critical and key to determining the capability of this new imaging system. An ECT system could potentially be applied to help further our understanding of soil moisture distribution in microgravity environments, thus promoting improvements to the NDS.

Approach

Bulk-Moisture Sensor

Capacitors respond to changes in the relative dielectric constant of the material between electrodes. This response is a function of the geometry of the capacitor and the distribution of the dielectric material within. Because of the presence of gravity, water will stratify in terrestrial plant growth containers. It is possible to construct a sensor that will vary in an almost linear fashion with water content by placing electrodes on the insides of the growth containers, with surfaces along the direction of gravity. However, capillary forces and absorption properties of growth media, salinity of the nutrient solution, and presence of plant root mass all have the potential to bias the capacitance reading. The thrust of this work was to build and test a capacitance-based sensor to detect moisture, while reducing the sensitivity to these biases for terrestrial applications.

Capacitance-Based Imaging System

The operation of the capacitive array is based on the measurement of capacitance changes introduced by materials placed close enough to affect the electric field between electrodes. The permittivity (dielectric constant) of a material determines the amount of charge needed to create a voltage across the material. Therefore, the capacitance presented by a material of a certain geometrical configuration will increase as the permittivity of the dielectric increases. Air has a permittivity close to unity, while freshwater has a permittivity of about 80, although it is dependent on temperature to some extent. Most nonconducting materials have relatively small dielectric constants with values typically less than 10. Oils, for example, have a value of about 2, silica glass about 4, Teflon about 2, and cryogenic fluids around 1.5. An accurate measurement of capacitance can be used to determine the presence of dielectric materials affected by the electric field generated by the capacitor's electrodes. The effect that a dielectric has on the measured capacitance depends on various factors, such as the geometrical configuration of the dielectric, its distance to the capacitor's plates, and the presence of other dielectrics or conductors nearby. The operation of the capacitive array sensor is based on the application of a small and fixed current to an electrode, which in combination with the surrounding ground plane and grounded elements; composes the capacitive element of interest.

Work done from FY 2002 through FY 2004 helped to develop an experience base in ECT electronics and image reconstruction techniques. Extensions for FY 2005 focused on integrating a new commercial capacitance-to-digital converter into a 3-D ECT system for possible application to zero- or low-g environments. The majority of ECT systems in literature are 2-D with a ring of electrodes surrounding a nonconductive pipe used to produce a cross-sectional image of material in the pipe. In addition, the image reconstruction techniques assume that capacitance readings are linearly related to the dielectric distribution within the pipe. This assumption is not valid for materials that have high contrast between the dielectric constants of constituents in the pipe. New image reconstruction techniques have been pursued that avoid these limitations and extend them for producing 3-D images.

Accomplishments

Bulk-Moisture Sensor

A sensor and test fixture were designed and fabricated. The test fixture was designed to precisely control the amount of nutrient solution within the sensor. A cylindrical-based capacitor design was implemented for the prototype sensor because it adapted best to the test fixture and was easily modeled electrically. A photo of the sensor in the test apparatus is shown in Figure 1. A test plan was implemented to determine the frequency response of the sensor to different media (glass beads and Turface, a claylike medium) and with different nutrient solutions. Literature suggests that at certain frequencies, capacitance values will be independent of the ion content (salinity) of the nutrient solution. This frequency was found to be about 300 kHz for both 1-mm and 2-mm glass bead substrates with different Hoagland's nutrient solutions. A plot of the capacitance versus volumetric water content is shown in Figure 2.

An empirical relationship was found for determining volumetric water content from a capacitance measurement. However, salinity still has a small effect on the capacitance reading, even at 300 kHz. It is well known that conductance of an electrolytic solution is related to the salinity. By using both capacitance and conductivity measurements on the same set of sensing electrodes, the water content could be found more accurately, with the added benefit of obtaining the salinity. This is important because variable salinities occur in plant applications, organic tissues, and porous media. Empirical relations were found for the test data from the 2-mm glass beads.

Figure 1. Bulk-moisture sensor in its test fixture without the moisture control plumbing attached.

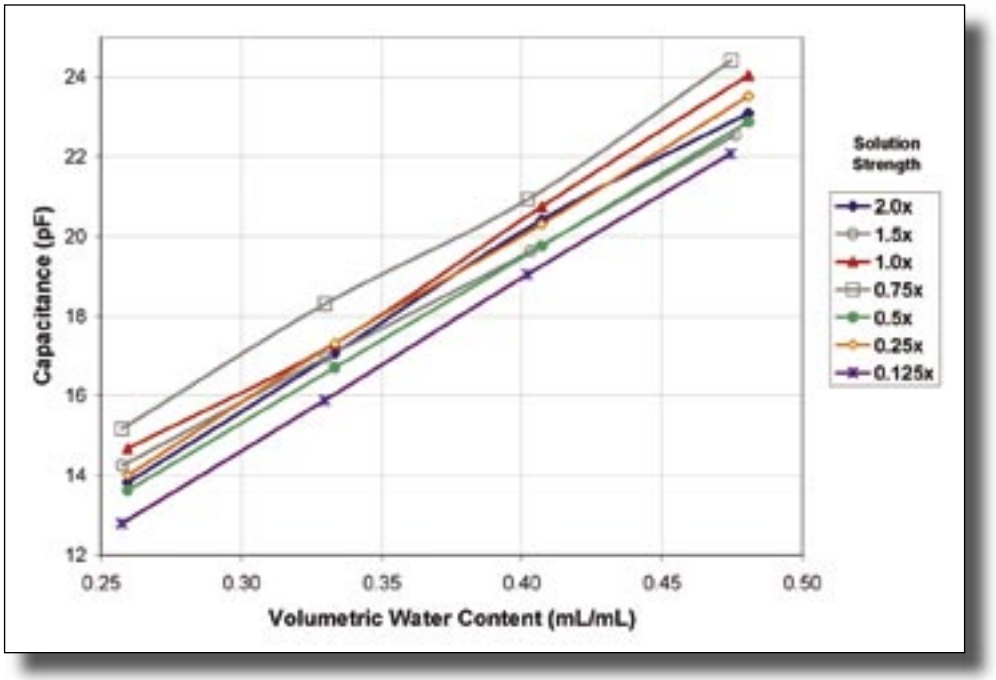

Figure 2. Bulk-moisture sensor capacitance output versus volumetric water content for 2-mm glass bead substrate with different salinity solutions.

Capacitance-Based Imaging System

Two 4×4 sets of electrodes were used to construct a 3-D ECT system with rectangular geometry rather than the typical 2-D system with 8 to 12 electrodes. Figure 3 offers a front view for one of the two electrode arrays on the left and a side view showing both arrays and the surrounding guard. The measurement electronics were designed around a new capacitance-to-digital-converter integrated circuit produced by Analog Devices, Inc., the AD7746. To simplify the initial design, the EVAL-AD7746 evaluation kit was used to provide an interface to the chip from both the sensing array and a computer. A switch network was designed and fabricated to switch between each of the electrode configurations to fully measure the capacitance matrix associated with the 32 electrodes. A simplified circuit diagram showing the basic element of the switch network appears in Figure 4.

The performance of an ECT system is dependent on many factors, such as geometry, number and size of electrodes, the material to be imaged, and the required speed and image detail. So, there is no single set of performance requirements that will apply to all ECT systems. However, salient characteristics mentioned in literature for an 8- to 12-electrode system are a resolution of 0.3 fF, a dynamic range of 0.3 fF to 2.0 pF, a root mean square (rms) noise level of less than 0.1 fF, low baseline drift, and an acquisition rate of 10 ms for one frame of data. This application focused on evaluating the electronics performance, where image detail is more important than acquisition rate. Therefore, the emphasis was on characterizing range, resolution, noise, and drift of the system.

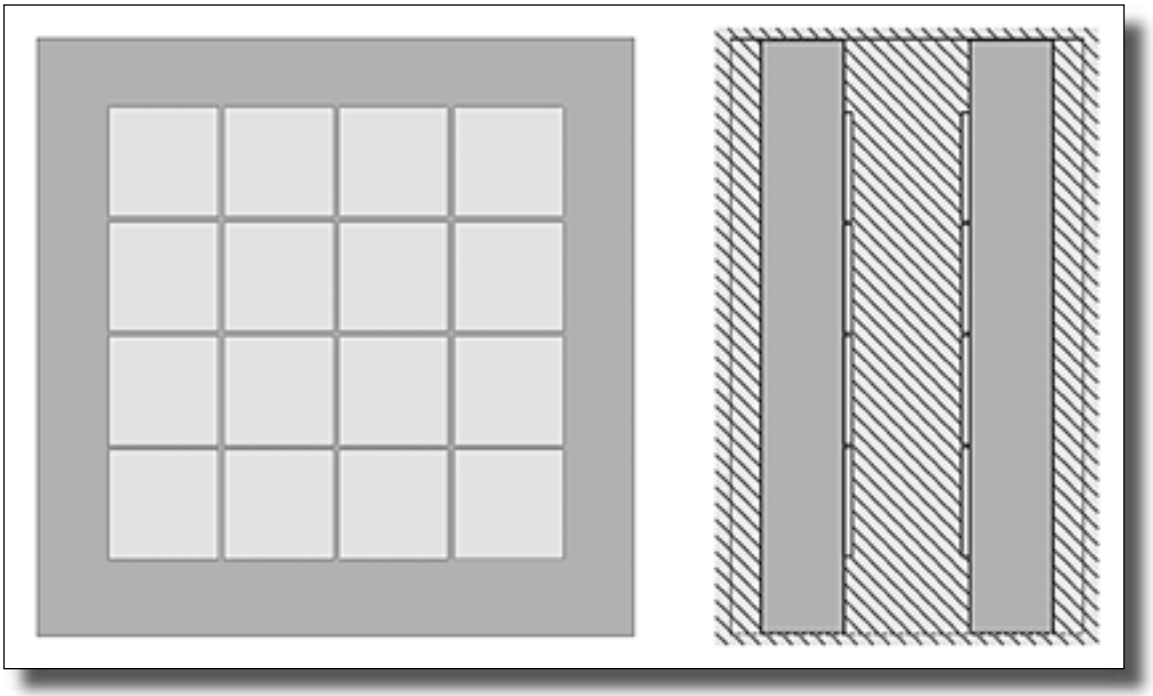

Figure 3. Front (left) and side (right) views of the electrode geometry used for the 3-D electrical-capacitance tomography (ECT) system. The side view shows the position of both electrode arrays and the surrounding guard.

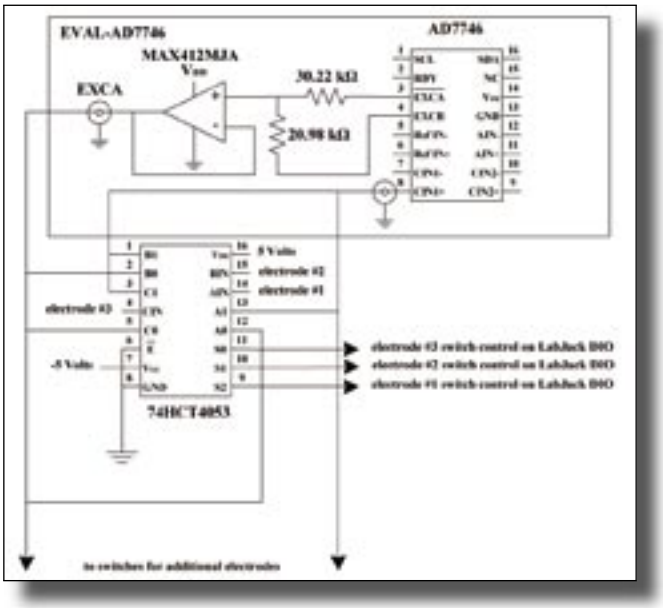

Figure 4. Basic electronics used in construction of the 3-D ECT system.

The external switch network used to change the electrode configuration system produced a large amount of offset capacitance. The addition of circuitry to divide the excitation signal on the AD7746 by a factor of 10.57 compensated for this. The resulting electronics are capable of removing 199.5 pF of offset capacitance, while increasing the range to ±42.3 pF and reducing the resolution to 42 aF. However, noise levels were increased from the switch network, which coupled an rms noise of 6.2 fF into the system. This is higher than desired but was reduced to an acceptable level by using a moving average on the data. The drift was 380 fF over 24 hours, but this was largely due to changing moisture content in the air. Desiccant was introduced to control the background moisture in the ECT test cell.

A number of algorithms have been created to reconstruct the image, with varying degrees of success. Each technique begins by creating a discrete model of the space between the electrode arrays. Discrete forms of Maxwell's equations are used to render a mathematical description of the space. A guess is made regarding the distribution of dielectric material, and the equations are then solved to calculate the capacitances. These calculated capacitances are then compared to the measured capacitances to determine how close the guess is to the actual solution. A figure of merit is used to assign a single value to quantify the quality of the guess. The guess is then either accepted or rejected, and a new guess is made based on some perturbation to the most current best solution. This repeats until the figure of merit is sufficiently small, indicating a good solution has been obtained. The method yielding the best result is based on a technique referred to as simulated annealing. Synthetic capacitance data was calculated for a given profile. This capacitance data was then used to test the quality of the different methods and figures of merit. The resulting image for the simulated annealing is shown in Figure 5. The dielectric profile used to generate the capacitances is shown on the left, and the reconstructed image is shown on the right.

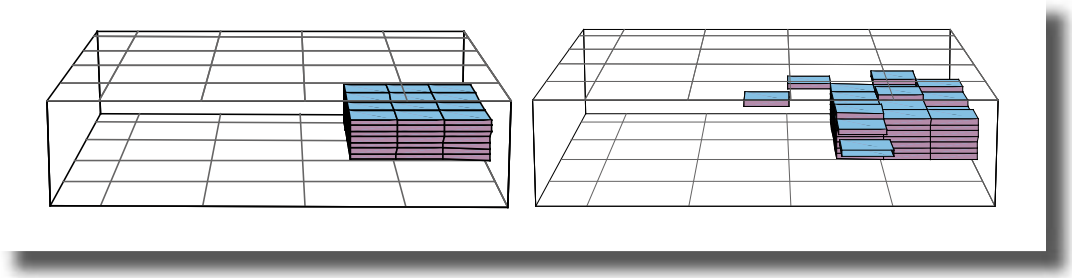

Figure 5. Left: a simulated sample between the conductor arrays (on top and bottom). Right: the image reproduced with a simulated annealing image reconstruction algorithm. The errors in reconstruction are with volume elements located toward the center of the arrays, where detection is least sensitive.

Images are being reconstructed from data taken with the ECT system described above. To get the best-fidelity image, the measured capacitance readings must be accurate to about 0.3 fF for the chosen geometry. The circuitry used provides this accuracy, but the technique requires that data be taken both with and without the sample present. The reconstructed image is then based on the difference between the two sets of capacitance readings. In the course of taking data, it was found that slight disturbances to the system while the sample was being inserted or removed caused large changes in the background capacitance. This results in poor image reconstruction. Consequently, the ECT hardware and cabling are being reworked to substantially reduce this source of error.

Publications

Nurge, M.A., "Capacitance Measurement with a Sigma Delta Converter for 3D Electrical Capacitance Tomography," NASA New Technology Report No.5020234, submitted November 29, 2005.

One paper is in progress summarizing the work on the development and experimental data from the capacitance-based bulk-moisture sensor. This will be submitted to a peer-reviewed journal in FY 2006 for publication.

A paper is in work related to the New Technology Report above that will include 3-D images produced by our ECT system. This will be submitted in FY 2006 to a peer-reviewed journal for publication.

A paper on ECT image reconstruction techniques is planned for FY 2006 and will be submitted to a peer-reviewed publication.

Status of Investigation

Work continued in FY 2006 to characterize the response of the bulk-moisture sensor with 1- to 2 mm Turface media and to determine the effect of root mass on capacitance and conductance. In addition, the peer-reviewed publications are in preparation.

The image reconstruction algorithms are being improved to increase execution speed and quality of the images produced. The ECT system will be used to acquire capacitance data from different samples. The algorithms will then be tested to characterize and optimize their performance with real data.

Planned Future Work

The bulk of this work was performed between mid FY 2005 and mid FY 2006. Funding of related activity beyond FY 2006 will be contingent upon the final results from the project.

Funding Authorized for FY 2005:

CDDF – $15K, Royalty Reinvestment – $50K

Actual or Expected Expenditures of FY 2005 Funding:

In-house procurements – $10K

In-house Contract – $55K

Completion Date: September 2006

Commodity-Free Calibration

Leader: Timothy Griffin, Ph.D., NASA

Other In-House Members of the Team: Carlos Calle, Ph.D., NASA
Andrew Nowicki and Mindy Ritz, ASRC Aerospace Corp.

Initiation Year: FY 2004

Purpose

In general, commodity-free calibration uses the reaction rates of compounds inherent in the analysis system to determine the concentration of the compound being monitored. This will help in developing a technique that truly can replace or enhance existing methods. This work will help to determine the strengths and weaknesses in the proposed techniques. Preliminary experiments have been performed to better grasp what is necessary to make advances in the new calibration technique.

All sensors, transducers, and instruments must be calibrated to provide optimum performance. In general, an instrument (sensor, transducer, etc.) is calibrated offline. Most commonly, instruments are removed from service and calibrated in another location. Alternatively, the calibration might be performed in the same location, but the instrument is still usually taken offline. Although this is usually an insignificant process, there are many applications where this method is extremely difficult, if not impossible. For example, how will instruments be calibrated on the Moon or Mars? A resupply ship most likely will not arrive every three months as is the case with the International Space Station (ISS).

Existing calibration techniques fail to consider several concerns that are vital to aerospace operations and space missions:

- electrical-power requirements,
- mass and volume of equipment,
- logistics involved in transporting calibrants to the instrument, and
- autonomous operation.

The space industry places a premium on such issues and hence, traditional calibration schemes are insufficient. NASA needs high-quality information for decisions that affect the lives of astronauts and personnel working around the vehicle. This project focuses on gas phase, although the general concept applies to any calibration and instrument method.

Commodity-free calibration is a novel approach to calibrating a variety of gas-monitoring systems. This technique will use reaction rate calibration techniques to design systems capable of simultaneous calibration and analysis. All of the necessary reactants will be inherent in the system. In practice, this will eliminate the need to add external calibration gas commodities. Thus, the present need to purchase, transport, store, and handle numerous gas cylinders containing varying concentrations of the gas of interest will be eliminated. Also eliminated will be the numerous limitations and drawbacks associated with the use of these gas standard commodities. The resulting gas-monitoring systems will cost less and be smaller, more accurate, more rugged, and safer to operate.

Background

Analytical instruments used for measuring gases require a method of calibration. Existing calibration techniques involve generation of a calibration curve by measuring instrument signal response to a variety of standards of the gas of interest over a range of concentrations. This concentration range is produced using numerous stock bottles containing calibrated standards (external-calibration commodities). From this data, a plot of instrument responses versus known concentrations results in an calibration curve and the equation of the best fit line through these data points are determined. Gas samples of unknown concentration are quantified by interpolation or extrapolation.

An advantage of this method is the simplicity of the caclulations used to approximate the unknown concentrations. However, the calibration curve technique has many shortcomings and disadvantages. For instance, the gas cylinders used to generate the calibration curve are generally large and heavy, and numerous cylinders are required for measurement over the calibration concentration range. Consequently, a vast amount of space is sacrificed for gas cylinder storage. In addition, it is often necessary to place these cylinders near the instrument, presenting significant logistical challenges. The pressurized tanks pose safety hazards and must be handled by trained personnel. As a result, supplementary labor costs are incurred by commodities that are often prohibitively expensive in and of themselves. Other safety concerns exist. For example, concern about the presence of a particular chemical is often the primary reason for performing an analysis. Increasing the amount of the chemical, often at toxic concentrations, even though for the purpose of analysis, increases the potential safety hazard.

Moreover, the accuracy using these gas standards for calibration is typically only 2 percent because it relies not only on the instrument and method but also on the accuracy of the stock bottle commodity concentrations. One major contributer to the overall inaccuracy of this technique is propagation of error stemming from the need for primary, secondary, and tertiary standards in the field.

Stock bottle commodities generally do not account for the matrix surrounding the analyte gas. Consequently, these interactions are disregarded and accuracy is compromised. Other factors contributing to the overall unreliability of these concentrations are molecular degradation and adsorption of the analyte molecule on the storage bottle surface. Furthermore, generating a calibration curve requires downtime, when the instrument is not able to monitor the sample. Although the simplistic calculations offered by the calibration curve technique are advantageous, accuracy, safety, and punctuality are more important and should not be sacrificed.

Commodity-free calibration will improve on the accuracy of the traditional calibration curve technique by shifting the focus from quantitative measurements (signal versus concentration) to measurements of time (signal versus time). The propagation of error associated with using standards of varying concentration is eliminated because there is no need for secondary or tertiary standards. And in cases where the reactant is present in great excess (e.g., psuedo-first-order reactions), accuracy is also not limited by the manufacturer of the primary calibration standard. Also, rather than trying to minimize physical phenomena occurring within the instrument, the commodity-free method exploits them. By incorporating these events into the calibration, instrumental error is reduced and accuracy is improved. Thus, the marriage of chemical and instrumental phenomena enables commodity-free calibration to mitigate the shortcomings of traditional calibration methods.

Calibration Curve Methods

Traditional Calibration Curve

Existing calibration technology involves generation of a calibration curve by measuring instrument response to a blank and over a range of concentrations of the analyte. These ranges are produced by external calibration standards of the analyte (external-calibration commodities). From this data, a plot of the best fit line of instrument response versus known concentration results in a calibration curve is determined. Samples of unknown concentration are quantified using the equation of the calibration curve in conjunction with measured instrument response to the sample.

Internal-Standard Method

This method is useful for analyses in which the quantity of sample analyzed or instrumental response varies from run to run for reasons that are difficult to control. The internal standard is a substance that is different from but similar to the analyte. The relative response of the detector to the analyte and standard is usually constant over a wide range of conditions. Thus, if the concentration of the standard is known, the correct concentration of analyte can be derived. A known mixture of standard and analyte is prepared to measure the relative instrumental response of the detector to the two species. From this, a response factor is determined and used to calculate the concentration of the unknown.

Reaction Rate Techniques

Some of the shortcomings of the calibration curve technique are mitigated through the use of calibration via reaction. The analyte sample interacts with one or more benign reactants that are inherent in the analytical system. By eliminating the need for external-calibration gas bottles, many concerns associated with the calibration curve method are eliminated. For example, multiple pressurized gas bottles, if any, are no longer required. Also, there is no need to transport high concentrations of hazardous commodities into the field. The accuracy is shifted to the instrument and method alone, no longer limited by the manufacturer of the calibration standard. And, the calibration and the monitoring occur simultaneously, allowing the instrument to operate with reduced downtime. In addition, concentration is not a limiting factor as it is with the calibration curve technique. This shortcoming is mitigated through reaction rate calibration because the unknown concentration is not determined by interpolation.

Reaction rate calibration techniques observe the rate of reaction of the analyte with one or more other reactants to determine the initial concentration of the analyte. This is possible because the rate of reaction is dependent on the concentration of the reactants. Both the initial concentration of the reactants or products formed and the reaction rate are directly proportional to the experimentally determined rate constant k. This rate constant is reaction-specific. Research determines the value of k for a given reaction. The reaction rate information is stored in a database, and this database replaces the calibration standards of the commodity. One can observe the reaction rate of the analyte with known amounts of the other reactants already present in the monitoring area by measuring the signal of one of the reactants or products formed versus time. The observed reaction rate can then be used to determine the initial concentration of the analyte. Since the concentration of the analyte is determined by measuring signal versus time, there is no need to bring varying concentrations of the analyte of interest to the field or sampling site as is required for traditional calibration curve methods.

General Method of Reaction Rate Calibration

The reaction rate calibration technique determines concentration by monitoring the reactions of the analyte with other compounds. Consider the reaction $A + B \rightarrow C + D$; the general rate equation for this reaction is rate = $k\,[A]^m\,[B]^n$, where $[A]$ and $[B]$ are reactant concentrations, m and n represent the order of the reaction with respect to the reactant, and k is a rate constant specific to that reaction. A reaction rate equation relates concentration and reaction rate for any given reaction to a specific, experimentally determined rate constant. This reaction is graphically represented in Figure 1. Established techniques exist for the empirical determination of the variables r, k, A, B, m, and n. It follows from inspection of the rate equation that if k is known, concentration can be determined from an experimental reaction rate. Herein lies the basis for reaction rate calibration. Specifically, reaction rates are monitored and unknown concentrations are calculated using the observed reaction rates in conjunction with previously determined rate constants.

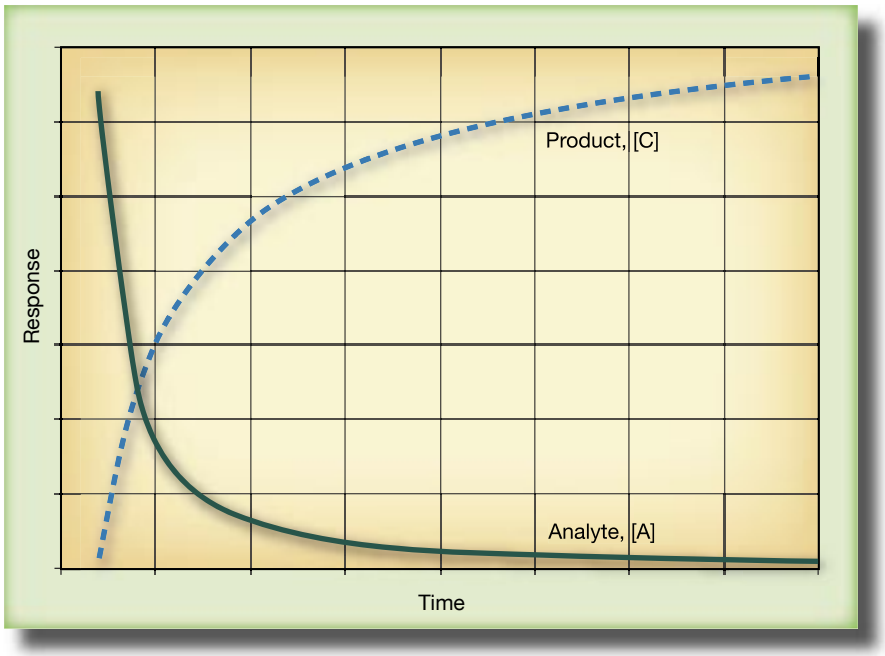

Figure 1. General method of reaction rate calibration.

Existing Reaction Rate Calibration Methods

Rate of reactions, or kinetics, has been used extensively to study reaction pathways. By monitoring process of formation or removal of the species, it has been possible to gain insights into the pathways that reactions follow.

It has been shown that once a reaction profile is determined, the concentration of a compound can be determined at a set time. This method has been used to follow batch processes in the laboratory and in industry. This technique has not been used as a calibration technique for monitoring of compounds during long-duration processes, such as possible leak sources.

The field of mass spectrometry has started to use reaction rates for calibration, with the idea that the species to be monitored is exposed to a specific ion species, such as water. The time is controlled by different methods, such as flight tubes, acceleration lenses, or trapping times. A newer technique that has shown promise is the proton transfer reaction (PTR) mass spectrometer. This technique uses the background water as the known reaction species. The water is ionized and then exposed to the sample for a set time. The reaction profile rate can then be determined and hence the concentration. Because the water must be kept at a set concentration or at a concentration exceeding that of the sample, the locations where this technique can be used are limited without the need for adding water vapor to the sample. For example, many processing locations at Kennedy Space Center, such as cryogenic lines, can have most of the humidity removed or greatly changed during the process being monitored.

One of the greatest drawbacks of PTR mass spectrometry is that the compound of interest must react with the water ions. This can be a major consideration when the compound of interest does not have the correct energy profile. Another drawback is that because the PTR is a mass spectrometry technique, it requires the reactions to be performed in a high-vacuum environment. The ionization and subsequent reaction steps can only be controlled under vacuum high enough to prevent interference from unwanted molecules.

The PTR technique is only one of the reactions that can be performed in the mass spectrometer system. Any compound that can be introduced into the vacuum system and ionized has the potential for use in this technique. While these requirements limit its use, many other compounds besides water could be used.

Approach

Commodity-free calibration is a reaction rate calibration technique that does not require the addition of any commodities. This technique is a specific form of the reaction rate technique where all of the necessary reactants, other than the sample being analyzed, are either inherent in the analyzing system, or one specifically added or privided to the system for a reason other than calibration.

After introduction, the component of interest will be exposed to other reactants already present in the system. The instrument detector will record the increase in the response of the reaction product, a decrease in the signal of the analyte response, or a decrease in the signal from the inherent reactant to determine the rate of reaction. This data will be used to calculate the initial concentration of the analyte.

This type of system would offer the same advantages as the reaction rate technique, including simultaneous analysis and calibration, reduced risk of false positives and exposure to toxic vapors, and improved accuracy. Moreover, having an excess of the reactant already present in the system abolishes the need to add commodities, which further reduces cost, logistics problems, and potential contamination. Also, the calculations involved can be simplified by comparison to those of the reaction rate technique.

Several conditions are necessary to make such a functional system practical. The reactant compounds must be present in excess so the calculations can be simplified. This may impose limitations on the concentration range of the analyte gas that can be analyzed. Another requirement is that the reaction system be reversible or have a continuous supply, such as background air or heat. Otherwise, the lifetime of the analytical system will be restricted.

Before commodity-free calibration can be implemented, a method development plan must first be satisfied. The plan is as follows.

a. Determine analyte of interest.

b. Determine reaction involving analyte with analytical system.

c. Demonstrate reactivity in analytical system:

   (1) Depletion of analyte/reactant?

   (2) Formation of product.

   (3) Analytical detectability (timescale, sensitivity, etc.).

d. Characterize reactivity in analytical system:

   (1) Propose and determine rate equation.

   (2) Determine effect of temperature.

   (3) Determine effect of interferences (humidity, air, etc.).

   (4) Determine transferability of data to other multiple instruments.

   (5) Demonstrate ability to quantify analyte.

e. Create database:

   (1) Record temperatures.

   (2) Record interference concentrations.

f. Test under field conditions.

One challenge in developing the reaction to use is that quite often the bond that is formed results in a lower molecular energy than the reacting molecules posses independently. Thus, energy input is required to break the covalent bond. This is a challenge for commodity-free calibration because if the analyte and a reactant inherent in the system react to form a permanent bond, then the reactant in the system is depleted. Unless the reactant is a compound that is in continuous supply or the reaction can be reversed, the reactant must ultimately be replenished. Therefore, commodity addition is required and the system cannot be classified as commodity-free. This must be kept in mind when selecting a reactant for development of a commodity-free calibration method for any given analyte. The reactant either must interact reversibly with the analyte or should be made available to the reaction system in unlimited supply.

Accomplishments

Flow Desorption Technique

The flow desorption (FD) system uses a gas chromatograph (GC) column for adsorption and desorption of the sample. The sample flows through a "reactive" column before reaching the analyzer. Two methods can be used on this system. The first is the adsorption/desorption comparison method, in which the sample typically flows through the blank/unreactive column until a calibration is to be performed. At that time, the reaction column is filled with the sample. The reaction column is then isolated for a set time and the subsequent measurement is compared to the blank-column measurement. The difference in the measurements is proportional to a known concentration based on the time that the sample was exposed to the reaction column.

The second method involves acquiring the reaction profile, either adsorption or desorption, for the sample when it is exposed to the reaction column. This profile, such as the one illustrated in Figure 2, can then be used in traditional reaction kinetics to calculate the concentration as previously discussed.

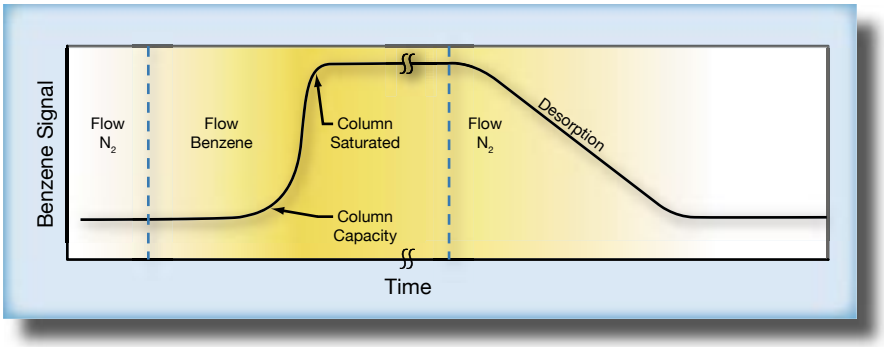

Figure 2. Acquiring the reaction profile.

The first-generation FD system (Figure 3) was hampered by timing problems arising from the plumbing and valving. To remedy the problems, a second-generation FD system was built up from an autosampler system. The reactive and blank columns, temperature controls, and valving constitute the automatic FD system, which is fed by a Kin-Tek vapor standard generator for testing purposes. Data collection with this software-driven system is pending.

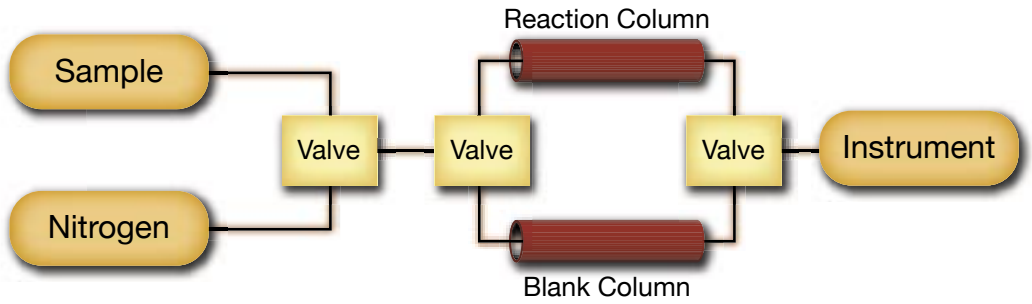

Figure 3. First-generation FD system.

A Peltier device (thermal electric cooler [TEC]) allows for thermal control. Initially this was intended to provide variable isothermal conditions for the flow desorption experiment. However, the Peltier was designed to allow both cooling and heating capabilities (by switching the polarity of the provided power). This heating and cooling capability inspired the idea that this technique could be extended to thermal desorption (with rather slow ramp rates) as well. This technique is assembled and ready for testing.

Thermal Desorption Technique

Tests are under way using the other experimental system developed for this project, a thermal desorption (TD) system. This system is similar to the FD system with a heating block incorporated around the reactive and blank columns for thermal desorption control. The heating block allows for rapid heating, an impractical use of a Peltier. To provide the ability to cool at a reasonable rate and to provide temperature control for rough isothermal operation, two large fans are available to flow ambient air across the desorption tube. Some minor electrical details must be resolved before data can be collected using this system.

An example of the instrument response transient is illustrated in Figure 4. Two primary reation rate regimes are desorption during rapid heating and desorption during the cooling cycle.

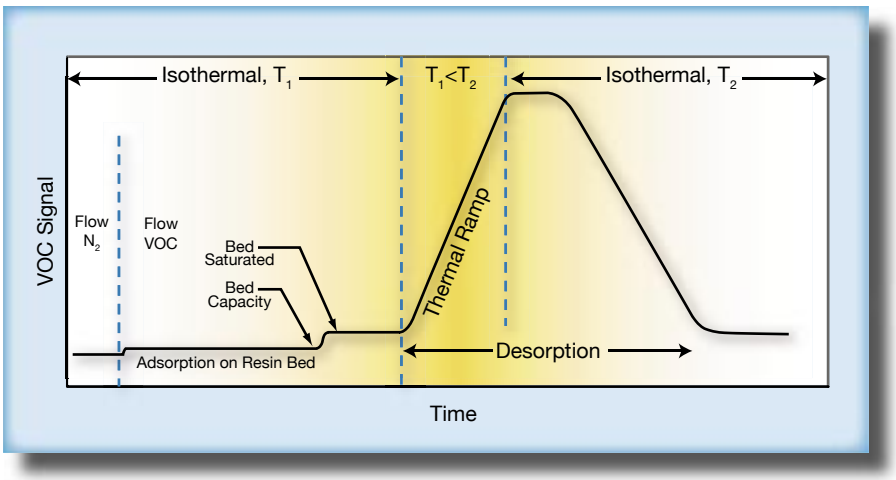

Figure 4. Example of instrument response transient.

Nitrogen Tetroxide

Tests to validate the method have been performed using hypergols. Hypergols are prime candidates for commodity-free calibration because they are highly toxic and exceptionally reactive. Consequently, these vapors present considerable challenges in handling and quantification. To use a reaction for calibration, it must first be characterized. Identification of the reaction rate constant k is of paramount importance. Preliminary reaction characterization studies were performed on dinitrogen tetroxide, (N_2O_4) otherwise known as nitrogen tetroxide (NTO) or hypergolic oxidizer, for further development of a commodity-free calibration system. Specifically, the reaction of NTO with N-(1-naphthyl)ethylenediamine dihydorochloride in acidic solution was studied. The naphthyl derivative product of this reaction exhibits an absorbance at 550 nm. Therefore, product formation over time can be monitored using a UV-Vis spectrophotometer.

These preliminary characterization experiments were conducted by first collecting NTO vapors at low concentrations (~10 ppm) in a fixed-volume gas collection tube. At $t = 0$, immediately after vapor collection, an acidic N-(1-naphthyl)ethylenediamine dihydorochloride ("diamine") solution (Figure 5) was injected into the collection tube containing the trapped vapors through a septum. The NTO vapors were allowed to react with the absorbing solution for a reaction time, t. At the given reaction time t, the contents of the collection tube were emptied into a cuvette and an absorbance measurement was taken using a UV-Vis spectrophotometer.

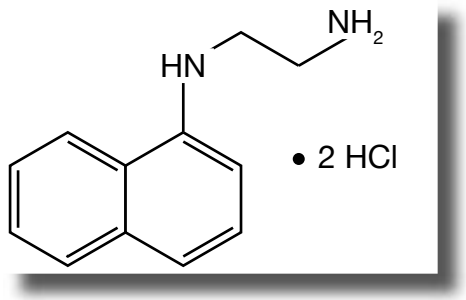

Figure 5. Molecular structure of N-(1-naphthyl)ethylenediamine dihydorochloride ("diamine").

Separate experiments were conducted with reaction times ranging from t = 1 min to t = 15 min. The data of this collection of experiments were plotted to generate a reaction profile of instrument response versus time for this reaction (Figure 6). The resultant curve is merely an approximation of the actual reaction profile as it was generated from a series of reactions rather than by monitoring a single reaction over time. However, these results do look promising (compare the observed reaction curve in Figure 6 to the theoretical reaction curve in Figure 1) in that the reaction proceeds at a reasonable rate to be used for analysis.

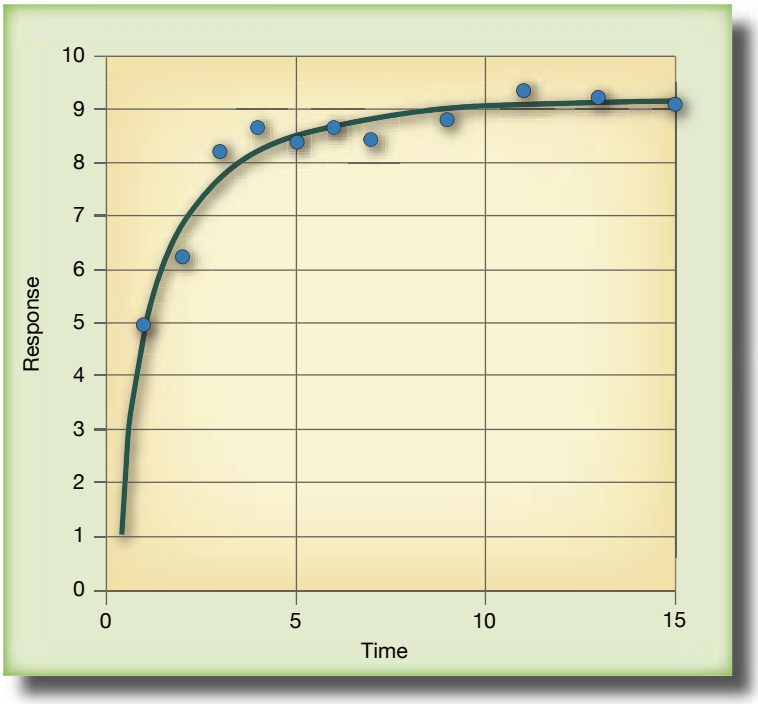

Figure 6. Reaction rate profile.

To monitor the kinetics of a single reaction, a custom UV-Vis cuvette was designed (Figure 7) that will contain the NTO vapors and allow for reaction with the diamine solution while time-based absorbance measurements are taken. The spherical bubble on top of the cuvette contains the NTO vapors and maximizes the solution-vapor interaction under these restricted reaction conditions. Upon delivery of the cuvette, reaction profiles from singular reactions over time can be generated. The plot of the log of the absorbance intensity, which is proportional to the product concentration, versus reaction time should be linear with a slope that represents the reaction rate constant k.

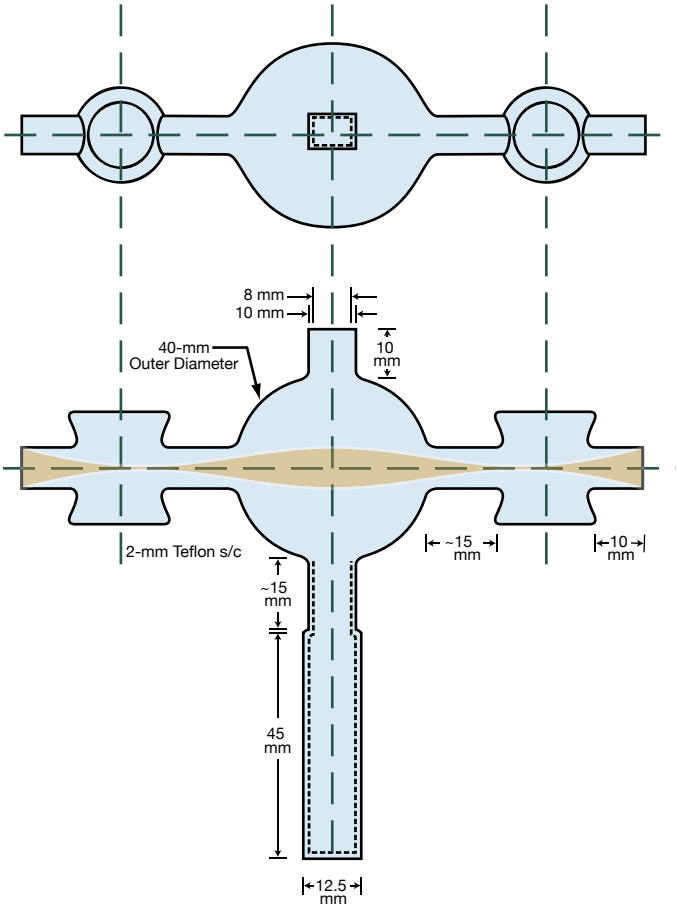

Figure 7. Custom-built UV-Vis cuvette.

A proposal for advancement of this burgeoning reaction rate calibration technique to commodity-free status suggested development of a cuvette, similar to the one in Figure 7 but coated in some way with an excess of the N-(1-naphthyl)ethylenediamine dihydorochloride reactant. A cuvette coated in this manner could be placed in the spectrophotometer and a gas sample introduced at $t = 0$. Time-based absorbance measurements would monitor the formation of the product, and from this data, the concentration of the NTO vapors could be calculated. Reaction reversibility is crucial for this procedure to fit the commodity-free requirement. If the reaction were not reversible, commodity addition would be necessary since the coating would need to be replaced.

Hydrazine-Derivative Colorimetric Technique

Another test of approach feasibility uses color change for exposure to the hypergolic fuel, hydrazine. The reaction of hydrazine with p-dimethylaminobenzaldehyde (PDAB) results in the formation of a benzaldehyde derivative (Figure 8).

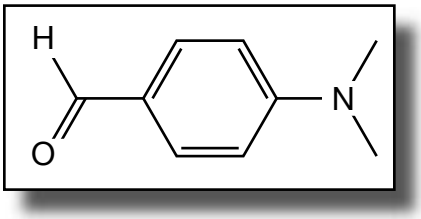

Figure 8. Molecular structure of benzaldehyde derivative.

A scheduled experiment will monitor the color change of a PDAB safety dosimeter badge with exposure to low-level hydrazine vapors in a fume hood over time. A plot of the overall color change, ΔE, versus reaction time should result in a suitable reaction profile. This reaction is also known to take place in solution. Thus, a custom UV-Vis cuvette similar to the one built for the reaction of NTO can be pursued in the case of hydrazine vapor with PDAB solution.

References

Gemperlin, P., G. Puxty, M. Maeder, D. Walker, F. Tarczynski, and M. Bosserman, "Calibration-Free Estimates of Batch Process Yields and Detection of Process Upsets Using in Situ Spectrscopic Measurements and Nonisothermal Kinetic Models: 4-(Dimethylamino)pyridine-Catalyzed Esterification of Butanol," *Anal. Chem.*, Vol. 76, Issue 9, 2004, pp. 2575–2582.

Hilderbrand, Scott A., Mi Hee Lim, and Stephen J. Lippard, "Dirhodium Tetracarboxylate Scaffolds as Reversible Fluorescence-Based Nitric Oxide Sensors," *J. Am. Chem. Soc.*, Vol. 126, Issue 15, 2004, pp. 4972-4978.

Warneke, C., J. De Gouw, W. Duster, P. Goldan, and R. Fall, "Validation of Atmospheric VOC Measurements by Proton-Transfer-Reaction Mass Spectrometry Using a Gas-Chromatographic Preseparation Method," *Environ. Sci. Technol.*, Vol. 37, Issue 11, 2003, pp. 5390–5397.

Status of Investigation

Studies have been conducted to demonstrate the feasibility of using reaction time as a method for calibrating a wide range of sensors. The tests performed have used color-indicating chemistry to track the reaction progress. Additional systems that do not rely on color have also been developed. These systems will use computer control to ensure the results are consistent. The systems are being tested and show promise for further refinement of the technique.

Funding Authorized for FY 2005: CDDF – $60K

Actual or Expected Expenditures of FY 2005 Funding:

In-house contract with ASRC Aerospace – $60K

Completion Date: September 2005

Application of Glow Discharge Plasma To Alter the Surface Properties of Materials

Leader: Carlos Calle, Ph.D., NASA

Other In-House Members of the Team:

Steve Trigwell, Ph.D., and Charles Buhler, Ph.D., ASRC Aerospace Corp.

Ellen Arens, M.S.E.E., NASA

External Partners/Collaborators:

J.S. Clements, Ph.D., and Jason Willis, Appalachian State University

Initiation Year: FY 2004

Purpose

Several materials that are considered important for spaceport operations are rendered noncompliant when subjected to the Kennedy Space Center (KSC) standard electrostatic testing (Standard Test method for Evaluating Triboelectric Charge Generation and Decay MMA-1985-79, Rev. 4). Treating materials that fail electrostatic testing and altering their surface properties so they become compliant would result in considerable cost savings and improve safety for the Space Shuttle, International Space Station, and Launch Services programs, as well as the Constellation program. These materials have excellent bulk and physical properties, are easy to process, and are relatively inexpensive. The bulk material often lacks certain required surface properties, such as hydrophilicity, roughness, and conductivity. Therefore, the surface of a polymer must be modified, without affecting the bulk property. However, changing the surface characteristics of these materials allows microbes to survive the cleaning and sterilization procedures required for NASA's planetary protection program. The goals of this project are to use atmospheric plasma glow discharge (APGD) to alter the surface properties of polymers for improved electrostatic dissipation characteristics and to determine if this surface modification enhanced or diminished microbial survival.

Background

Current surface treatments exposing materials to plasma, corona, photons, electrons, flame, ion beams, and x-rays can

- produce special functional groups at the surface,
- increase the surface energy,
- increase or decrease hydrophilicity,
- improve chemical inertness,
- introduce cross-linking,
- remove weak boundary layers and contamination, and
- increase the surface morphology.

All of these methods require that the materials be enclosed in vacuum chambers where they can be exposed to different atmospheres. The APGD method used in this work can be applied in atmosphere, eliminating the difficulty of treating materials in a vacuum chamber. The method allows operation at low temperatures, minimizing heat damage to the polymer surface. Oxygen and oxygen-containing plasmas are the most commonly used. An APGD using O_2 or air creates free radicals (N, O, OH, etc.) and excited species (N*, N_2*, O*, O_2, etc.) that form active products (O_3, H_2O_2, HNO_2, and HNO_3) that chemically react with the surface, improving the wettability. The depth of surface modification depends upon the power level and duration of treatment. For polymer samples, it is typically several hundred angstroms. However, if ultraviolet (UV) light is generated in the plasma, the depth of UV-induced cross-linking can be greater than a micrometer.

After plasma treatment, the effects of aging, caused primarily by the environment and temperature can be detrimental to the modification are. Polymer chains are more mobile on the surface than in the bulk, allowing reorientation. This may be due to diffusion of low-molecular-weight oxidized material into the bulk and migration of polar functional groups. These polar groups are in a high-energy state and attempt to reduce the interfacial energy by migration into the bulk. High temperatures can accelerate these processes, whereas low temperatures have been shown to reduce the aging effect. Once a surface has been modified, the effect of the modification on the surface topography and chemistry needs to be monitored.

For this project, several candidate films that failed the electrostatic tribocharging testing for use during processing were identified as vital by Space Shuttle Ground Operations. These materials are Rastex (a polytetrafluoroethylene [PTFE] woven cloth used in the Orbiter radiator protective covers), Frommelt Saf-T-Vu M1083 (Solid Rocket Booster joint enclosures for segment mating operations), Herculite 20 white, Herculite 20 blue, Herculite 10W yellow (used in launch service processing), and Saf-T-Vu (a polyvinyl chloride [PVC]) material used in Solid Rocket Booster joint enclosures for segment mating operations). Allowing the use of a wider range of materials would considerably reduce product and handling costs and provide less stringent working conditions, such as being able to operate at high relative humidities.

Approach

The Electrostatics and Surface Physics Laboratory (ESPL) at KSC developed techniques and methodologies to alter the surface properties of materials to prevent, mitigate, and detect electrostatic charge generation on flight hardware and support equipment for spaceport structures.

This project applied APGD to the surfaces of materials to improve their electrostatic dissipation (ESD) and corrosion resistance properties. It is well documented that applying glow discharge plasmas improves the wettability of certain polymers, which leads to improved charge dissipation properties. However, only a limited range of materials has been tested. It is also well known that this application also leads to oxidation of metal surfaces, which in turn helps prevent further corrosion of the metal.

To determine the ESD characteristics of the materials, corona charging and tribocharging against PTFE felt material were performed on as-received materials in ambient conditions at a constant 45±3 percent relative humidity (RH) and at 72 °F. The charge decay performance was monitored and the surface and bulk resistivity measured. Once the type of gas or gas mixture and the energy dose (plasma power and time exposure) that provide maximum surface modification (oxidation) for each individual material were determined, APGD was applied to the materials.

Once the material surfaces were treated, the surface and bulk resistivity were retested for improved ESD properties. The testing was performed to the ESD association standard test method ESD S11.11-2001, "Surface Resistance Measurement of Static Dissipative Planer Materials," and ESD S11.12-2000, "Volume Resistance Measurements of Static Dissipative Planar Materials." To determine the period of effectiveness, it was necessary to monitor the hydrophobic recovery (aging) and effects on the wettability of the treated materials over several months using x-ray photoelectron spectroscopy (XPS) and surface energy measurements as determined by contact angle measurements. Flammability and/or hypergolic compatibility effects were also tested. The effects of glow discharge plasma exposure in modifying the oxidation/reduction characteristics were investigated and corrosive properties tested using electrochemical impedance spectroscopy.

Six materials were used in this study: aluminum 6061, PTFE, polycarbonate, Saf-T-Vu, Rastex, and Herculite 20. Coupons of each material were ultrasonically cleaned for 10 minutes successively in acetone, methanol, and isopropanol, and finally rinsed in deionized (DI) water. The coupons were allowed to air-dry in a positive-pressure sterile hood until used.

Accomplishments

A schematic of the experimental setup is shown in Figure 1, and the actual setup is shown in Figure 2. Figure 3 shows a closeup of the plasma head and the rotating platform that ensures even exposure to the plasma. In the setup, a humidifier was included so the relative humidity of the oxygen could be varied to determine if it would enhance the surface reactions.

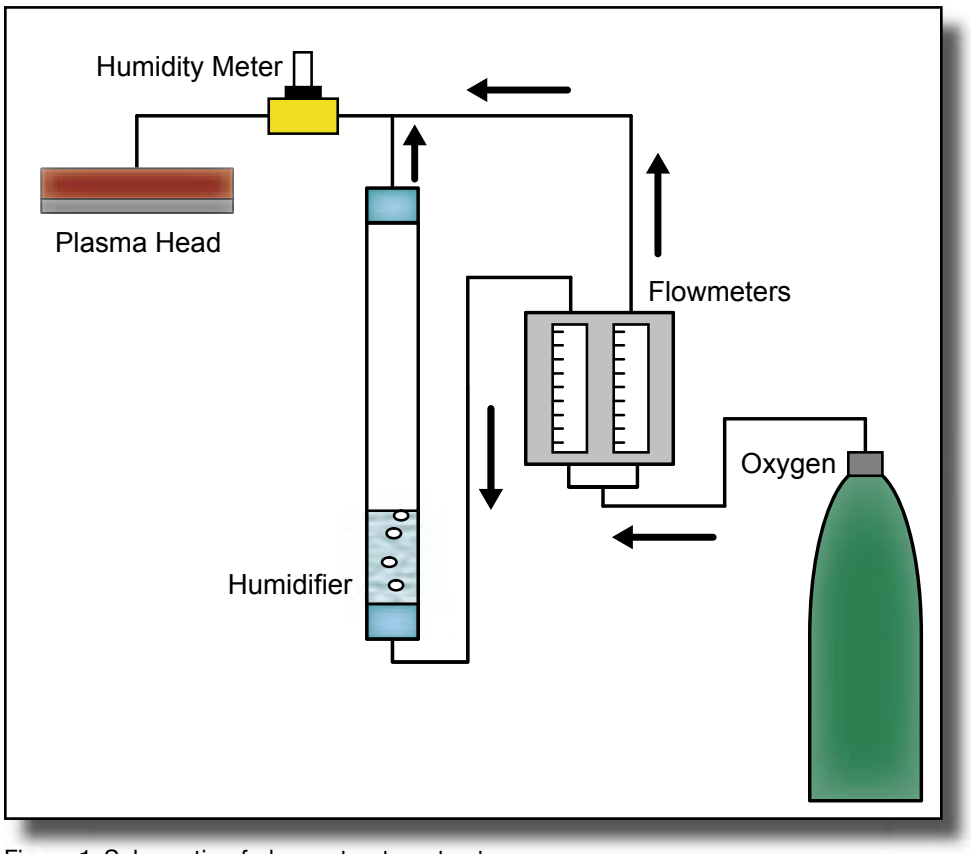

Figure 1. Schematic of plasma treatment setup.

Figure 2. Plasma treatment setup.

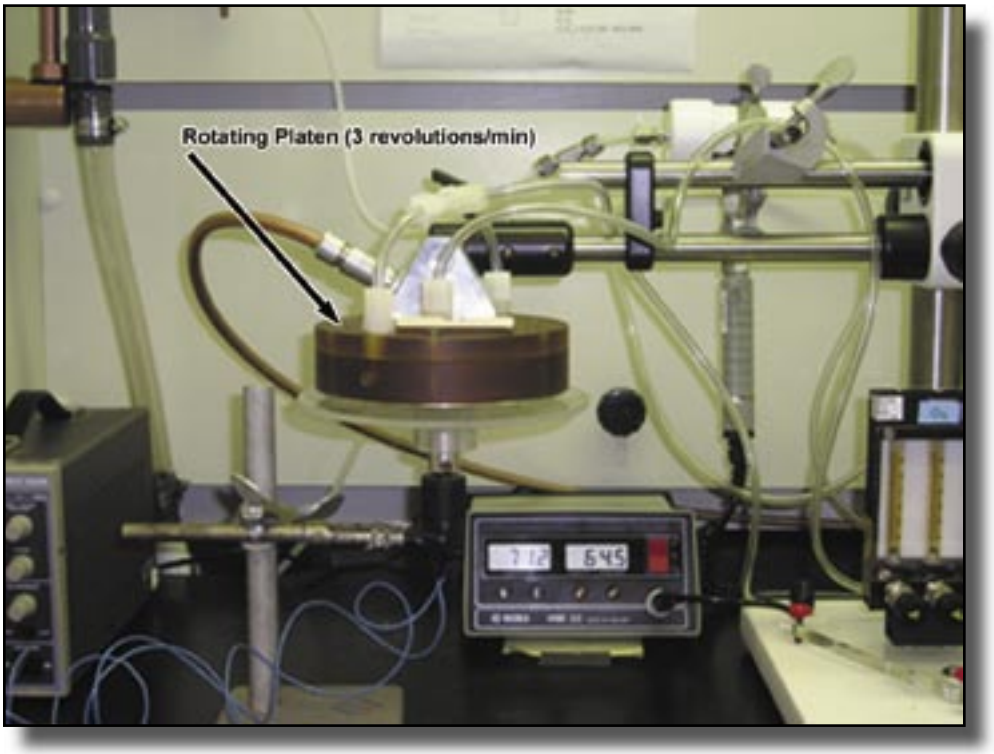

Figure 3. Close-up of plasma head.

The plasma treatment procedure was optimized on Saf-T-Vu, Herculite 20 white, and Rastex, with different gases (O_2, air, O_2+H_2O, and He+O_2) at 47±3 percent RH and at 72 °F. He + O produced the most significant effect, determined by monitoring the increase in the O:C ratio on the surface by XPS and by contact angle measurements. Contact angle measurements were performed on a VCA Optima XE contact angle instrument purchased for this project (Figure 4). The measurements were performed using DI water (18 MΩ). Once again, the measurements were taken at 45±3 percent RH and at 72 °F. Surface contact angle measurements for Saf-T-Vu decreased from 108° to 35° after APGD treatment, showing increased hydrophilicity. Monitoring the aging showed no recovery with a measured contact angle of 30° after 3 weeks (Figure 4). An increase in hydrophilicity typically increases the conductivity of a surface and hence enhances charge dissipation.

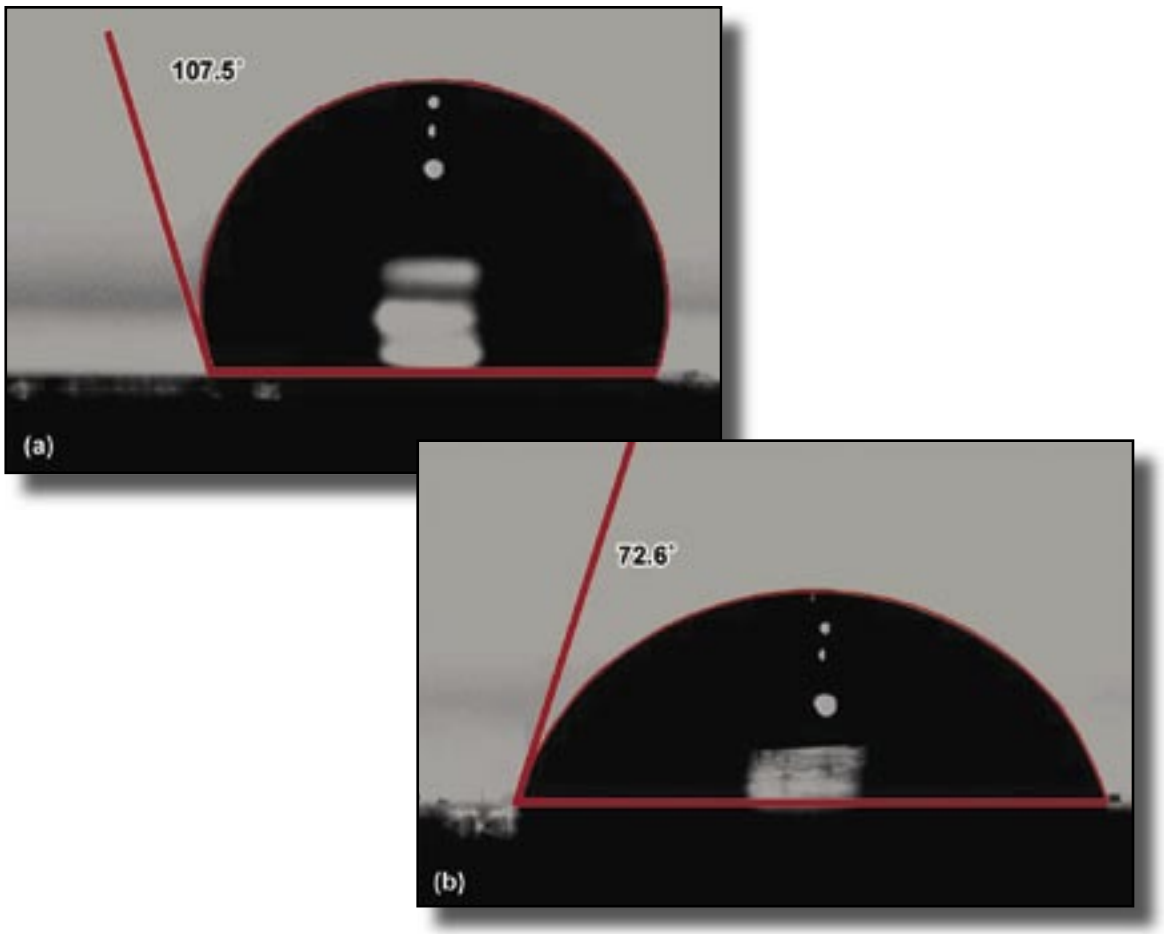

Figure 4. (a) Contact angle of DI water on Saf-T-Vu as received. (b) Contact angle after 6 minutes, showing increased hydrophilicity. Longer exposures decreased the contact angle to 35°.

Figure 5 shows the effect of He + O_2 on Saf-T-Vu. Subsequent tribocharging data for the two materials are shown in Figure 6. The remarkable data in this figure shows that a hydrophobic material such as Rastex (basically a woven PTFE cloth) can be made electrostatically dissipative compared to untreated materials that charged up and retained a high voltage (approximately –6 kV to –7 kV).

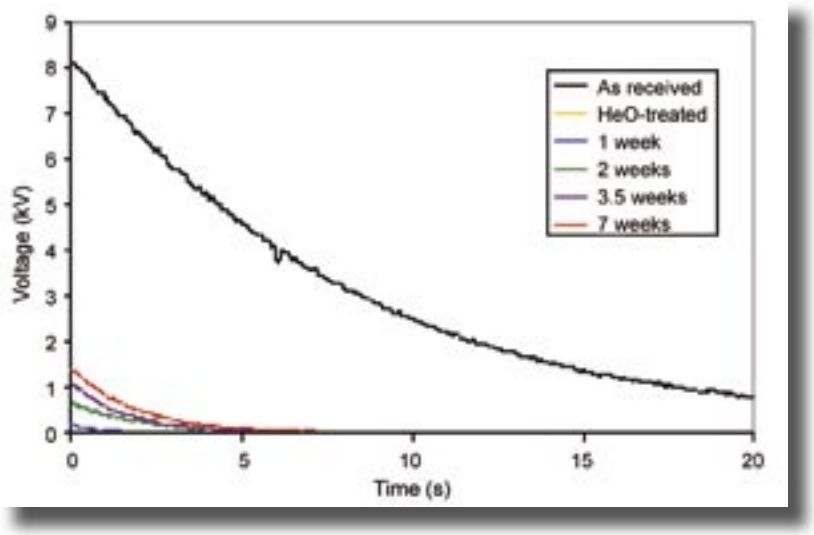

Figure 5. Effect of He + O_2 APGD on Saf-T-Vu. The curve clearly shows that, for the as-received material, the surface voltage after tribocharging failed to reach <350 V after 5 seconds, required by the standard. After APGD treatment, and after 7 weeks, the material passes the standard test.

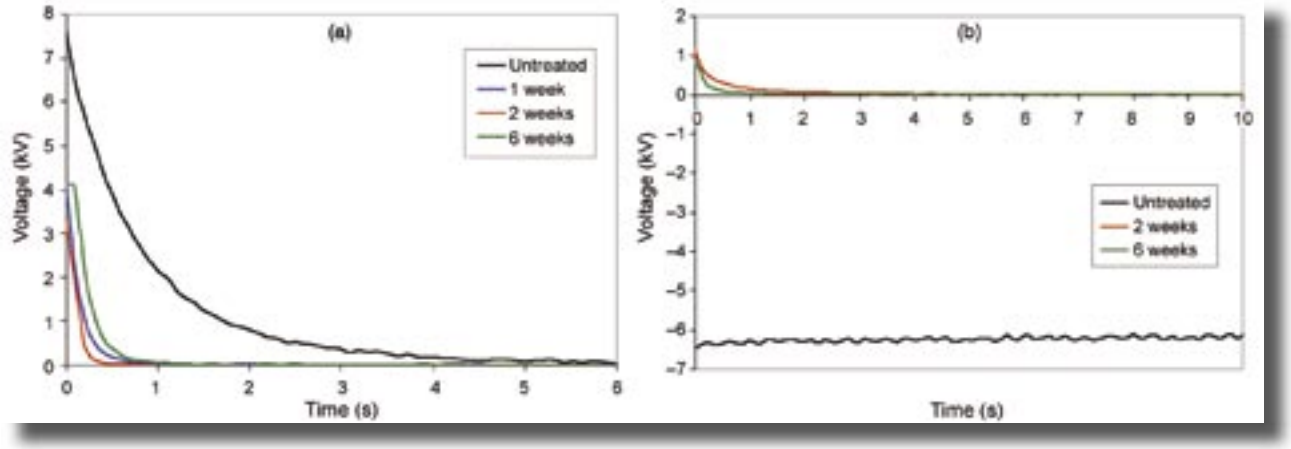

Figure 6. (a) Herculite 20 white showing material easily passes the test and (b) Rastex also passes the test 6 weeks after APGD and Hydrolast treatment.

Exposure to He+O_2 APGD plasma and subsequent chemical treatment significantly improved the electrostatic dissipation of polymeric materials and rendered them compliant with the KSC standard electrostatic test. The results were still valid up to 7 weeks after treatment.

For the final part of the project, aluminum 6061, PTFE, and polycarbonate were treated by the optimized protocol for the inclusion of bacteria testing. All six materials were treated as above and then transferred to a microbiological lab to evaluate how spores of the bacterium *Bacillus subtilis* HA101 would adhere to the treated materials. Spores of *B. subtilis* were applied to the treated upper surfaces of each coupon at the rate of ≈1.5 × 106 viable spores per coupon. Two tests were conducted. First, to estimate how "sticky" the materials were after plasma treatment, spores were applied to coupons, allowed to air-dry at 25 °C for 24 hours, and then processed with an enhanced Most Probable Number (MPN) assay with a minimum detection limit of 10 spores per coupon. Second, to determine if the plasma-treated materials inhibited the survival of spores over time, a new set of plasma-treated coupons was doped with spores of *B. subtilis* and then placed within incubation chambers maintained at 30 °C and 100 percent RH for 7 days. After incubation, the MPN assays were used to estimate the numbers of viable spores still adhering to the coupons after treatment.

Results of the microbiological assays indicated that aluminum 6061 was the stickiest of the six materials tested, but that all six materials were unaffected after plasma treatment for the level of inherent stickiness to spores of *B. subtilis* compared to non-plasma-treated controls. However, in the second assay, incubation in a 100-percent RH environment resulted in a clear decrease in recovered spores for aluminum 6061, polycarbonate, and Saf-T-Vu, when compared to the non-plasma-treated controls. In addition, there was a slight (but statistically significant) increase in the spores recovered from the plasma-treated coupons—PTFE, Herculite, and Rastex—compared to non-plasma-treated controls.

The results of the spore testing indicate that plasma treatment can both inhibit and enhance the recovery of adhered spores after exposure to saturated ambient environments of up to 100 percent RH. Thus, the plasma treatment does alter the surface properties of several spacecraft materials, making them either slightly more, or slightly less, sticky to spores of *Bacillus subtilis* when compared to non-plasma-treated coupons.

Publications

"Application of glow discharge plasma to alter the surface properties of materials," *Proc. ESA Annual Meeting*, Alberta, Canada, 46–54 (2005).

A subsequent paper has been submitted for publication in the *Journal of Electrostatics*.

Trigwell, S., C.R. Buhler, and C.I. Calle, "Application of Atmospheric Plasma to Alter Electrostatic Properties of Spaceport Materials," *Proc. of the IOP Conference on Novel Applications of Surface Modification*, University of Chester, Chester, England, September 18–21, 2005.

Trigwell, S., D. Boucher, and C.I. Calle, "Electrostatic Properties of PE and PTFE Subjected to Atmospheric Pressure Plasma Treatment," *Proc. of the 2006 ESA/IEJ/IEEE-IAS/SFE Joint Conference on Electrostatics* (2006).

Planned Future Work

A $378K, 3-year proposal titled "Glow Discharge on Mars: Potential Factors in the Degradation of Organics in the Martian Regolith" was selected for funding by the NASA Science Mission Directorate (SMD) in December 2004. This NASA Research Announcement (NRA) seeks to understand the consequences of electrical discharges on the chemistry and biology of Mars. In particular, it seeks to investigate the possibility that glow discharges explain the absence of organic material and carbonaceous matter on Mars.

Aggregate Amount of Funding Authorized: $117K

CDDF, CTRG&A Cost Center 76APPGLOW, UPN 274, outside contract with National Research Council (Postdoctoral Fellow Dr. Steve Trigwell) – $20K

Expected Completion Date:

The CDDF project concluded in September 2005. Work funded by SMD NRA to evaluate glow discharge on Mars will continue through April 2008.

Extraction of Lead Compounds for Remediation of Lead-Based Paints

Leader: Jacqueline Quinn, Ph.D., NASA

Other In-House Members of the Team: James Captain, University of Central Florida

Purpose

The research described herein sought to develop a wipe-on, wipe-off chemical process to remove lead oxides found in paint.

Background

Lead is a toxic substance that can cause a variety of health problems, including such diverse conditions as brain damage in children and digestive and nervous disorders in adults. Lead poisoning can also affect wildlife in areas where the metal has contaminated natural media. Lead can be found in paint, soil, household dust, and even in drinking water from lead plumbing or lead solder. Considerable amounts of lead contamination exist today as a direct result of the use of lead in paint prior to its ban in 1978. Formerly, lead paint was chosen as a coating for steel structures because of its superior durability, adhesion capabilities, and rust prevention characteristics, but it was also used prolifically in houses built before 1978. Old chipping paint can contaminate areas surrounding the structure and create concerns for human health and the environment. Removing lead, especially from lead paint, is of great importance to prevent this dangerous potential, which still exists today. The removal or elimination of lead-containing paint remains a costly and hazardous process. Unsafe removal of lead by dry abrasive blasting, the leading technology attacking the problem today, can initiate release large amounts of contaminated particulate matter that also pose health risks.

In general, there are four basic types of materials that compose paint: the solvent, the chemical binder, pigments, and additives (used typically to suspend pigment and shorten drying time). The solvent is the liquid that carries the solid components of paint and evaporates after application to leave behind the remaining solid components. The binder is the most important component because it forms the solid film that binds the pigment particles together. Binders used in paints can vary from alkyd-based paints to more specialized agents, including polyurethane resins, epoxy resins, and silicone-based resins. Drying oils are also used in paint to combat the brittleness that results from using resin alone.

The lead in lead-based paint is found in the pigment, the most common forms being white lead and red lead. White lead is in the form of lead carbonate ($2\ Pb(CO_3)_2 \cdot Pb(OH)_2$), and red lead is in the form of lead oxide (Pb_3O_4). The small particles of lead compounds are dispersed and suspended in the paint by the binder. The majority of lead compounds, particularly those used in paint, are chosen in part because they are insoluble and extremely durable. Lead compounds are very stable and not easily removed from the binder, yielding high durability and long-term performance. However, it may be possible to chemically swell the binder and leech the pigment out of the paint matrix without having to physically remove all the paint on a structure. If successful, this approach could greatly reduce the labor involved with paint stripping, the quantity of hazardous waste produced, and consequently, the cost.

Enhancing the mobility of lead oxide is a challenge because of its nonreactive nature and extreme stability. In the medical field, chelation therapy is a well-known and commonly used method of removing lead and other heavy metals from the body. Chelating agents are chemical compounds with the ability to form multiple bonds to a single metal atom. Not only is it possible to chelate metal ions already in solution, but chelating agents can also dissolve compounds containing metal atoms that are otherwise considered insoluble. Using a chelating agent to make the lead compounds soluble could increase pigment mobility and enhance the ability of the lead to leech out of the paint.

Approach

Several common chelating agents were evaluated in an attempt to find a functional chelating agent for lead oxide. Examples include ethylene diamine tetraacetic acid (EDTA), citric acid, and succinic acid. Experiments showed mercaptosuccinic acid (MSA) (Figure 1) was able to dissolve lead oxide very quickly with minor agitation and therefore became the best candidate. Unlike some of the other chelating agents tested, MSA contains sulfur. Sulfur is known to bind well with lead, more so than the oxygen or nitrogen in the other chelating compounds mentioned because of its larger, "softer" electron shell.

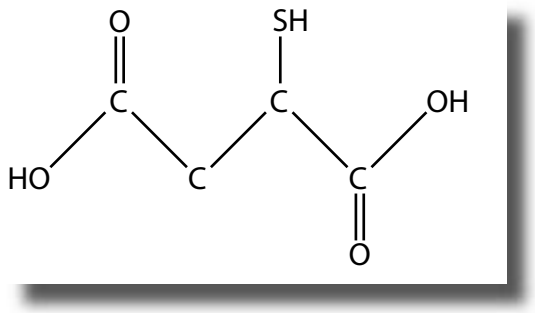

Figure 1. Mercaptosuccinic acid (MSA).

Samples were analyzed by two methods: flame atomic absorption spectroscopy (Flame AA) and inductively coupled plasma atomic emission spectroscopy (ICP AES). In Flame AA, a sample is introduced to a flame at high temperatures (~2,500 ºC) and lead compounds are reduced to atoms. These lead atoms are then passed through a beam of light at a wavelength characteristic of lead. By calculating the amount of light absorbed, the concentration of lead in the sample can be determined. Conversely, ICP-AES works by measuring the emission of light, instead of the absorption. This means that after the sample is passed through a plasma flame, the lead becomes ionized and enters an excited state. When electrons relax from this excited state, they emit a characteristic wavelength of light. This ionization and excitation occurs because the temperature of the plasma flame is many times that of the Flame AA.

For the first set of experiments performed, paint chips and scrapings of Type I and Type II paint were placed in solution to test for lead removal. The solution of 5 percent MSA in water at pH = 7 was able to dissolve as much as 75 percent of the lead oxide in both of these paints in under 48 hours. Follow-up experiments were performed by applying lead-based paint to glass slides for uniformity. These samples were soaked in the same 5 percent MSA solution for 24 or 144 hours and some were pretreated for 24 hours in d limonene in an attempt to swell the paint to give better permeability to the chelator. While 14 percent of the lead was removed from the slides that were treated for 24 hours, as much as 39 percent of the lead was removed from the slides that were treated for 144 hours. For both treatment times, just over 40 percent of the lead was removed from the slides that were pretreated with d limonene. These results, shown in Table 1, indicate that paint swelled by d-limonene and then extracted reaches saturation after 1 day in MSA as opposed to 6 days without swelling. The maximum amount of lead dissolved was less than that in the study using paint chips. This was expected because of the reduced surface area of paint in contact with the chelator. Also noted in the sampling procedure is when Type II paint is exposed to MSA, the solution turns purple. This color change, illustrated in Figure 2, is caused by the chelation of the iron oxide, which is found in the pigment of Type II lead paint.

Table 1. Results of applying MSA solution to Type II paint.

Type II Paint on Glass Slides	Lead Concentration in AA Aliquot (ppm)	Paint Mass (g)	Calculated Concentration of Removed Lead (ppm)	Lead Removed (%)
Nitric acid digest (control)	382	0.2502	152,478	100
24-hour MSA treatment	74	0.4986	21,513	14
144-hour MSA treatmennt	74	0.4991	59,286	39
Pretreatment w/ d-limonene + 24-hour MSA treatment	353	0.4233	64,740	42
Pretreatment w/ d-limonene + 144-hour MSA treatment	251	0.5571	62,266	41

Figure 2. MSA color change in response to the presence of iron oxide found in Type II paint versus Type I paint.

Multiple extraction experiments have shown continued lead pigment dissolution in smaller quantities, leading to the conclusion that the chelating solution is simply saturated and cannot dissolve any more lead until being replenished. However after two to three MSA extractions, the paint loses adhesion to the glass slide and completely strips from the surface. Results from experiments on old painted steel panels from launch umbilical towers at Kennedy Space Center were inconclusive because of nonuniform lead concentrations caused by weathering.

Aside from the complex matrix of components in lead paints, a simple remediation technique may exist. Strides were made in identifying a chelator that can dissolve and bind lead pigment; however, the real-world application of this technology still proves challenging. Previous work to remove polychlorinated biphenyl (PCB) from paint has shown some organic solvents can swell paint to allow for enhanced mobility of the target species. Swelling the binder to allow the chelator access to the pigment still requires a more in-depth look. Solving this problem may be the key to unlocking this technology's field applicability.

Funding Authorized for FY 2005: $123K

Completion Date: September 2005

Development of Focused Metabolite Profiling Capability for Dissecting Cellular and Molecular Processes of Living Organisms in Space Environments

Leader: Raymond Wheeler, Ph.D., NASA

Other In-House Members of the Team: Lanfang Levine, Ph.D., Dynamac Corp.

External Partners/Collaborators: Charles Guy, Ph.D., University of Florida

Purpose

The purposes of this project are to establish a high-throughput and robust metabolite profiling (MP) platform and prove the concept of integrating MP and transcript (gene expression) profiling approaches for better understanding the "law" of biological regulation.

Background

Regulatory control in biological systems is exerted at all levels within the central dogma of biology: DNA→messenger RNA (mRNA)→Enzymeinactive→Enzymeactive→Metabolites. Metabolites are the end products of all cellular regulatory processes and reflect the ultimate outcome of potential changes suggested by genomics and proteomics caused by an environmental stimulus or genetic modification. Following on the heels of genomics, transcriptomics, and proteomics, metabolomics has become an inevitable part of complete systems biology because none of the lower "-omics" alone provides direct information about how changes in mRNA or protein are coupled to changes in biological function. Analogous to the precedent "-omics," metabolomics is the systematic study of collections of small molecules (i.e., metabolites) in a biological system (a cell, organ, or organism). In contrast to the traditional biochemistry approach in which target metabolites and enzymes are studied, metabolomics takes a holistic view of the entire suite of metabolites (the metabolome) in an organism to capture the coordinated regulation of biological systems. Thus, metabolomics, coupled with other "-omics" such as transcriptomics and proteomics, holds great promises for deciphering the functions of genes, predicting novel metabolic pathways, and providing insights to the regulation of a biological event, as well as in directing metabolic engineering of plants for human benefit. However, the challenge is much greater than that met in genomics because of the greater number of metabolites and greater structural diversity, and thus properties. Developmental work is needed in such areas as (1) methodologies for unbiased extraction of metabolites and subsequent quantification, (2) algorithms for systematic identification of metabolites, (3) expertise and competency in handling a large amount information (data set), and (4) integration of metabolomics with other "-omics" and data mining (implication of the information).

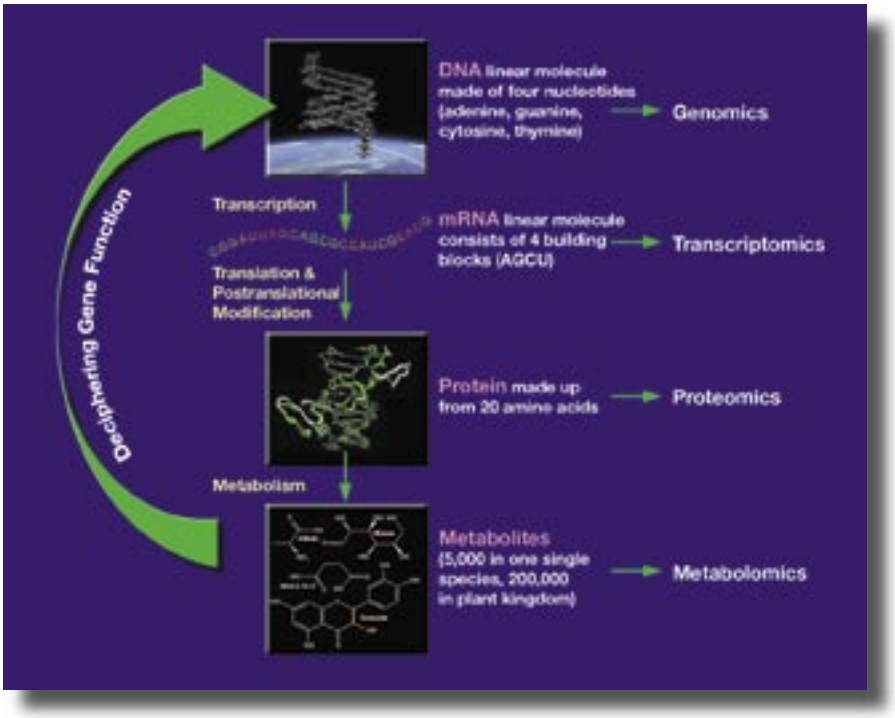

Central dogma of biology and the "-omics" revolution.

Approach

Develop a robust MP platform to assess vast numbers of metabolites in a biological system

This encompasses (1) developing procedures for unbiased metabolite extraction and derivatization, followed by high-throughput gas chromatography (GC)/mass spectrometry (MS) or liquid chromatography (LC)/MS analysis, (2) establishing an automated deconvolution program for chromatographically unresolved peaks caused by the presence of a great number of metabolites, and (3) developing technical competency in structure elucidation or identification of unknown metabolites.

Apply the developed MP platform in parallel with analysis of mRNA to provide deeper insight into complex regulatory processes of plants

A primary objective of MP is to associate relative qualitative (appearance of new metabolites in experimental treatment) and quantitative (upregulated or downregulated) changes in metabolite levels with gene expression responses directly linked with physiological and developmental functions. *Arabidopsis* (a model plant) will be cultivated under elevated CO_2 and will be examined by coupling MP with transcriptome profiling techniques.

Develop data mining strategies

A sound statistical approach is needed to link cheminformatics and bioinformatics to reveal underlying cellular and molecular regulation processes.

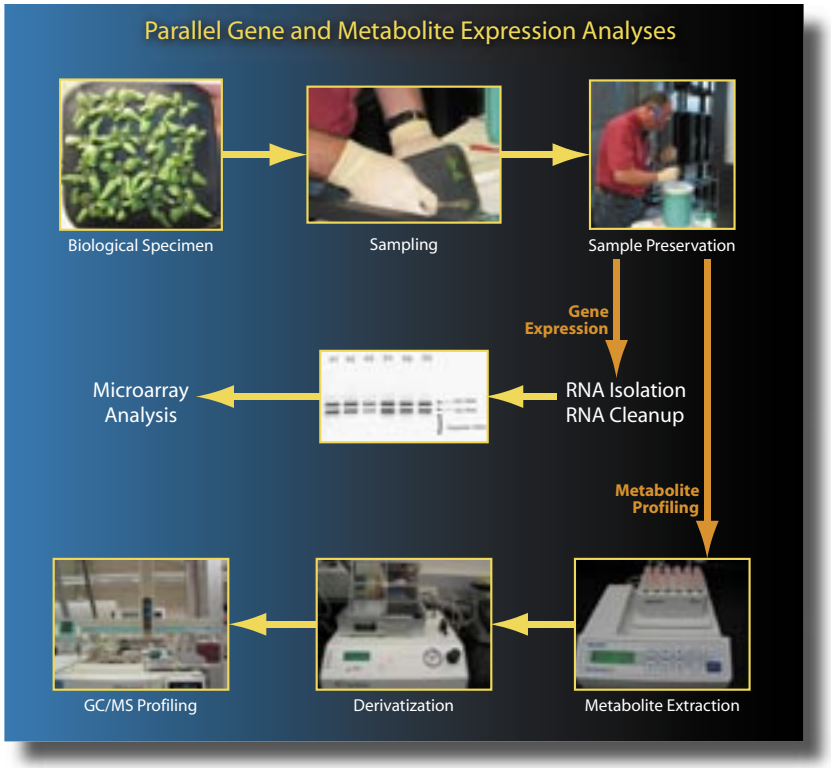

Overview of experimental strategy.

Accomplishments

- Acquired and/or developed tools required for a minimum MP capability.
- Established and evaluated procedures for unbiased and reproducible metabolite extraction and derivatization prior to MP by GC/MS.
- Developed a data acquisition method for polar small-molecule metabolites.
- Acquired and tested a custom-built mass-spectrum library for the GC/MS, resulting in an expanded mass-spectrum database to allow identification of derivatized compounds that are not in the commercial mass-spectrum library, such as the National Institute of Standards and Technology MS library.
- Implemented an Automated Mass Spectral Deconvolution and Identification System (AMDIS) and currently working on employing this system to extract qualitative and quantitative information from the raw GC/MS data files collected by an instrument-specific software (Xcalibur).
- Developed a short computer program (Excel Macro) to sort and summarize the output from AMDIS.
- Completed a series of three experiments using a model plant, *Arabidopsis*, grown in a controlled environment and varied CO_2 levels. Samples were collected for gene expression and MP. Meanwhile, stomatal density and starch concentration were also determined for the same set of samples.

Talks/Presentations

The team presented its findings to a group from the University of Florida Citrus Research Center.

Manuscripts

- Submitted a Technical Memorandum to NASA annual report for 2005.
- Submitted a manuscript titled "Phenotypic Expression of Metabolites in Wheat Grown Under Moderately and Super-Elevated CO_2" to *Physiologia Plantarum*.

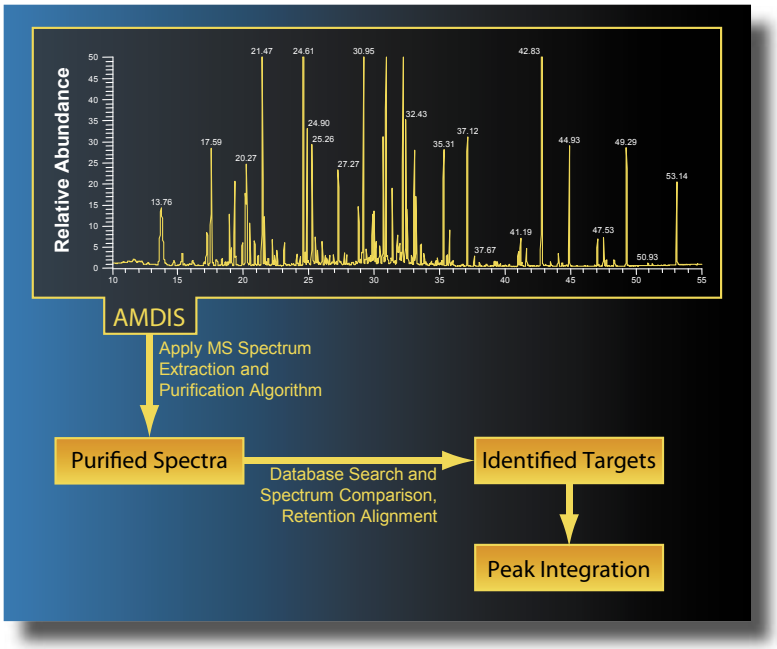

Example of GC/MS chromatogram of *Arabidopsis* metabolites and steps involved in processing of raw GC/MS data.

Status of Investigation

The project has generated interest from the fields of plant and microbe interaction and microbiology and was renewed for FY 2006. A research proposal titled "Light, CO_2, and Temperature Inputs of *Arabidopsis* Growth and Development As Assessed by Parallel Gene Expression and Metabolite Profiling" submitted to the National Science Foundation received a high-priority rating, although it is not funded.

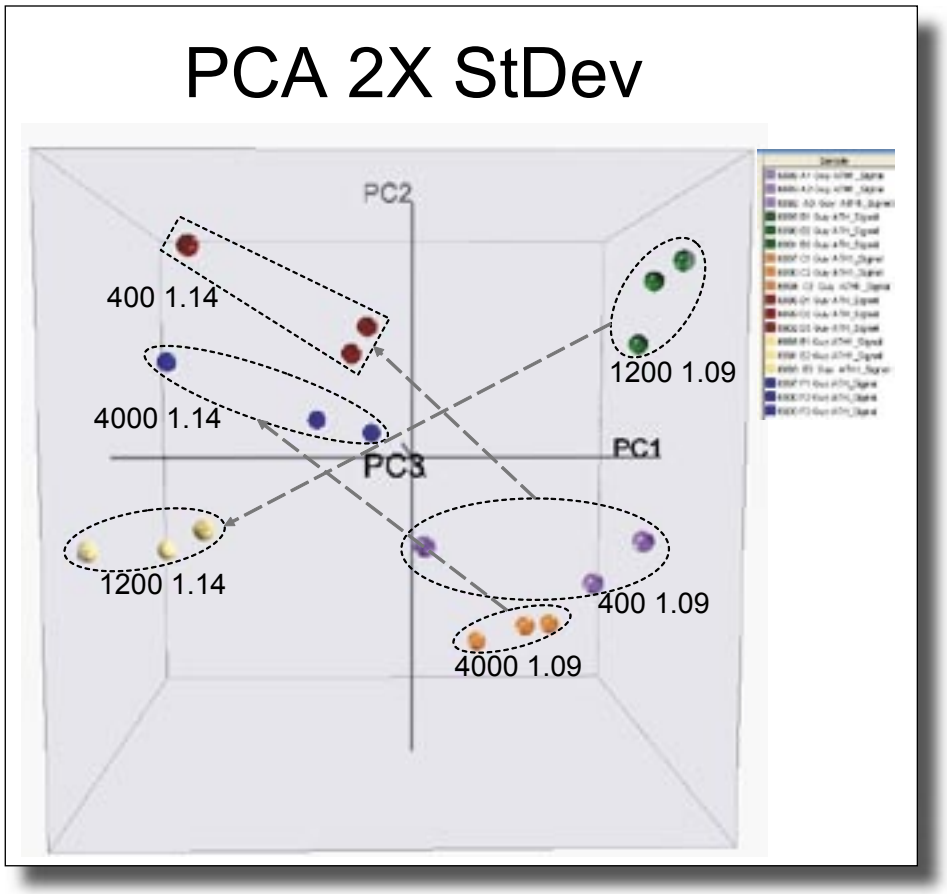

Principle component analysis (PCA) of gene expression demonstrates that both CO_2 concentration and developmental stage affect transcripts.

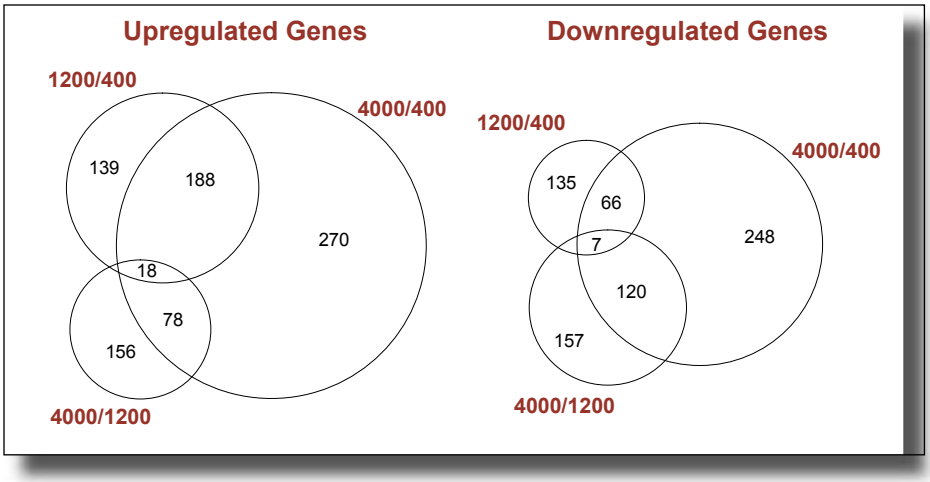

Extent of elevated CO_2 effect on gene expression. Numbers outside the circle indicate the CO_2 concentrations under which plants were grown (1200/400: 1,200 ppm CO_2 compared with 400 ppm CO_2 grown plants). Numbers inside the circles indicate the number of genes upregulated or downregulated at p = 0.05.

Planned Future Work

- Complete the profiling of metabolites in plant materials grown under three CO_2 levels (400 ppm as control, 1,200 ppm, and 4,000 ppm), using the GC/MS platform established in FY 2005.
- Complete the implementation of MS deconvolution algorithms, work out the kinks, and develop techniques to rapidly extract qualitative and quantitative information from raw GC/MS profiling data.
- Repeat biological experiments (*Arabidopsis* under various CO_2 levels) to collect plant growth, histology, and physiology data to complement the gene and metabolite profile.
- Develop data mining strategies (statistics): quantify connectivity between metabolites and gene expression for responsive synthetic pathways related to production in elevated CO_2.

Funding Authorized for FY 2005: $140K

Actual or Expected Expenditures of FY 2005 Funding:

In-house contract – Dynamac Corp. – $140K

Completion Date: December 2005 – Phase I

Physics of Rocket Exhaust Cratering

Leader: Philip Metzger, Ph.D., NASA

Other In-House Members of the Team: Bruce Vu, Ph.D., NASA

Christopher Immer, Ph.D., Robert Cox, Brian Larson, and Alex Taylor, ASRC Aerospace Corp.

Carly Donahue, USRP Student, Berry College

Purpose

This project sought to unravel and explain the excavation processes that occur when a jet of gas impinges on a bed of sand. This is important for rockets launching or landing on the dusty, sandy surfaces of the Moon and Mars.

Background

During the Apollo and Viking programs, there was considerable research into the blast effects of launching and landing on planetary regoliths. That work ensured the success of those missions but also demonstrated that cratering (or soil erosion) would be a significant challenge for other mission scenarios. For example, high-velocity spray of eroded soil will pose a challenge when we attempt to land multiple spacecraft within short distances of one another on the Moon (Figure 1). The first spacecraft to land may be scoured and contaminated by the spray from the second. We have the relevant experience of the Apollo 12 Lunar Module (LM) landing 155 meters away from the deactivated Surveyor 3 spacecraft (Figure 2). Portions of Surveyor were returned to Earth by the Apollo astronauts for analysis. It was found that the surfaces had been sandblasted and pitted and that every opening and joint was injected with grit from the high-speed spray.

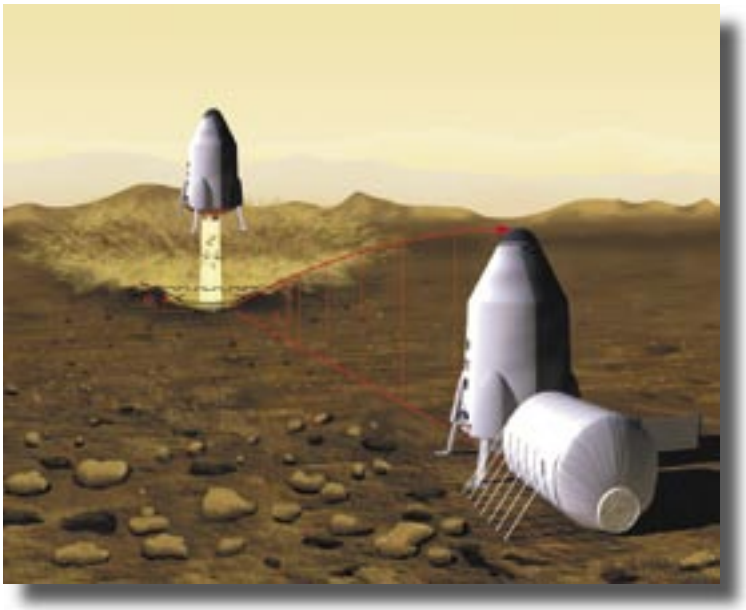

Figure 1. Colanded hardware must not damage or contaminate one another.

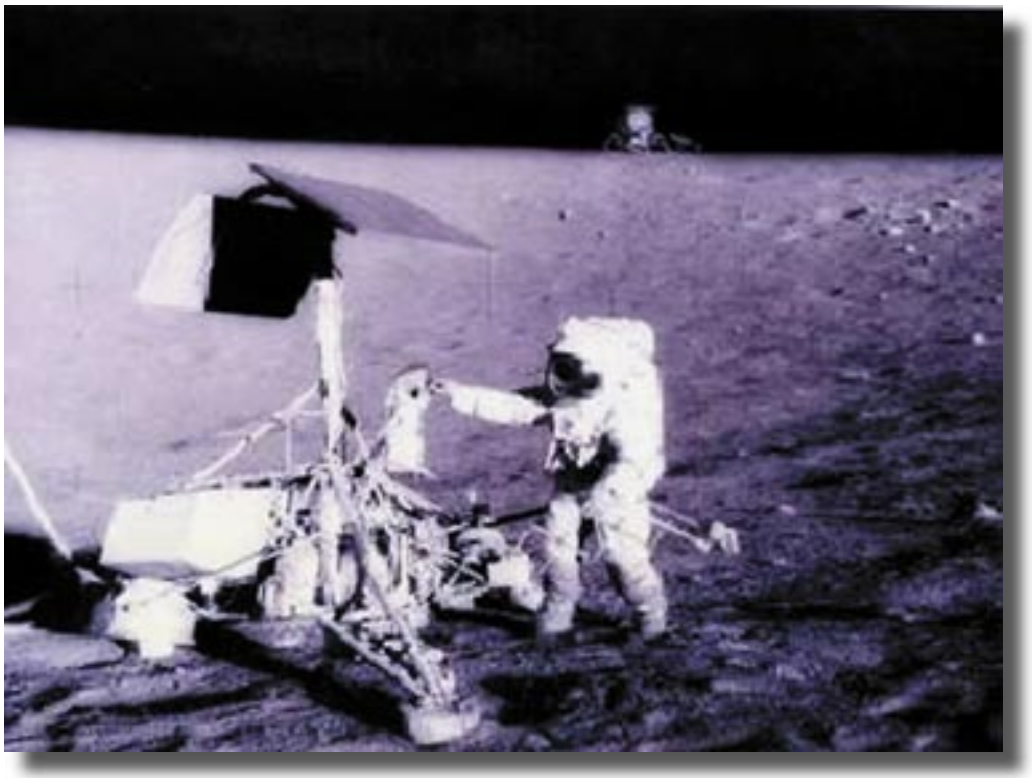

Figure 2. Apollo 12 Lunar Module landed 155 meters from the Surveyor 3 spacecraft, scouring and pitting its surface and contaminating open crevices.

Simply building a berm to block the spray around the landing site will not be a complete solution. First, while the majority of soil particles are ejected into low-elevation angles and hence stopped by the berm, some fraction may be ejected over the berm as a result of local surface roughness.

Second, if the lander uses multiple engines, then the ground-effect recirculation of gas along the reflection planes between the engines will eject sand particles with high velocity at very high-elevation angles over the berm. These particles will also strike and possibly contaminate any exposed hardware on the bottom of the spacecraft.

Third, after engine cutoff there is a central core eruption of soil in the vertical direction as gases beneath the plume's stagnation region are suddenly released from the soil. This may contaminate the engine bell or combustion chamber, creating a potentially dangerous condition inside the engine during its next firing. Furthermore, repeated landings on the same site will repeat this process many times, driving gases in and out of the soil beneath the stagnation, eventually loosening the compacted surface and producing the chance of localized soil fluidization or pressure cratering beneath the plume on subsequent launches or landings.

Despite their shortcomings, berms are the primary strategy to mitigate lunar soil erosion. Berm effectiveness must therefore be quantified to provide the environmental design requirements for hardware outside the berm. Prior studies of soil erosion and cratering were performed before modern instrumentation was available. Hence, there has never been an adequate description of the physical processes or scaling that occur inside a jet-induced erosion event. Also, the prior theory, based on the erosion of desert dunes, cannot be extrapolated over so many orders of magnitude for the flow conditions, where different aspects of the physics predominate. Therefore, the space program needs to understand the basic physics of the cratering and erosion processes before it can confidently develop the technology to control them.

Approach

Ultimately, the realistic lunar-erosion effects must be solved by a program that includes computer simulation. It is very difficult and expensive to attack the problem by experiments alone because of the difficult and unique environments of the Moon or Mars. Firing hypersonic jets of gas in vacuum chambers is difficult because once the jet starts, the chamber is no longer a vacuum, and the ambient pressure affects the form of the plume. Some chambers can evacuate the gas of a hypersonic jet to maintain vacuum, but the tests in such chambers would have to be very large to cover the anticipated distance of the particulate flow. Such a configuration is dangerous to the facility because the suspended particulate matter could ruin the chamber's high-speed pumps. Even if the costs and facility risks for such tests were justifiable, it would still be impossible to control gravity in the experiment and extremely difficult to prepare a soil surface that matches the compaction, interlocking, and frictional behavior of lunar soil particles. Hence, computer modeling is ultimately required as part of the overall investigation, and the sooner the computer modeling is included, the less expensive and the more effective the overall effort becomes. Therefore, we have adopted a strategy to enable the early development of realistic computer models. Before the fully integrated models can be written, we must develop an understanding of the physics of plume-soil interactions to ensure that the correct physics are incorporated. This project therefore undertook an experimental investigation supported by simple computer modeling to identify and explain the basic physics.

The experiments used subsonic jets of compressed gas, aimed vertically at the surface of dry, cohesionless sand. The conditions were carefully controlled so that scaling laws could be extracted. Tests were performed with jets of different gases (nitrogen, carbon dioxide, argon, and helium) to provide variations in gas density, at different exit velocities, with different nozzle heights above the soil, and with different-sized sand grains.

The test results were observed two different ways. In the first method, the sand was laid down in horizontal layers inside a box, with each layer of sand being a different color. Next, the sand was cratered by the jet, and afterward the shallow crater was filled in with black sand (to provide a level surface yet offer a contrast of color to identify the location of the crater's surface). It was then impregnated by optically clear epoxy, and it was cured in an oven. The block of epoxy-stabilized sand was cut in half to reveal how the flat, colored layers of sand had been deformed beneath the surface during the cratering process. We expected that the layers would be bent downward beneath the crater as a result of the pressure of the jet causing bearing capacity failure in the gas-weakened soil. This was predicted by researchers during the Apollo era, but this is not what we discovered. When we split open the cratered sand, we discovered that the deepest layers of sand were actually brought upward to the surface in the center of the crater, rather than being pressed downward. This effect is shown in Figure 3.

To understand how this counterintuitive flow pattern developed, a second experimental

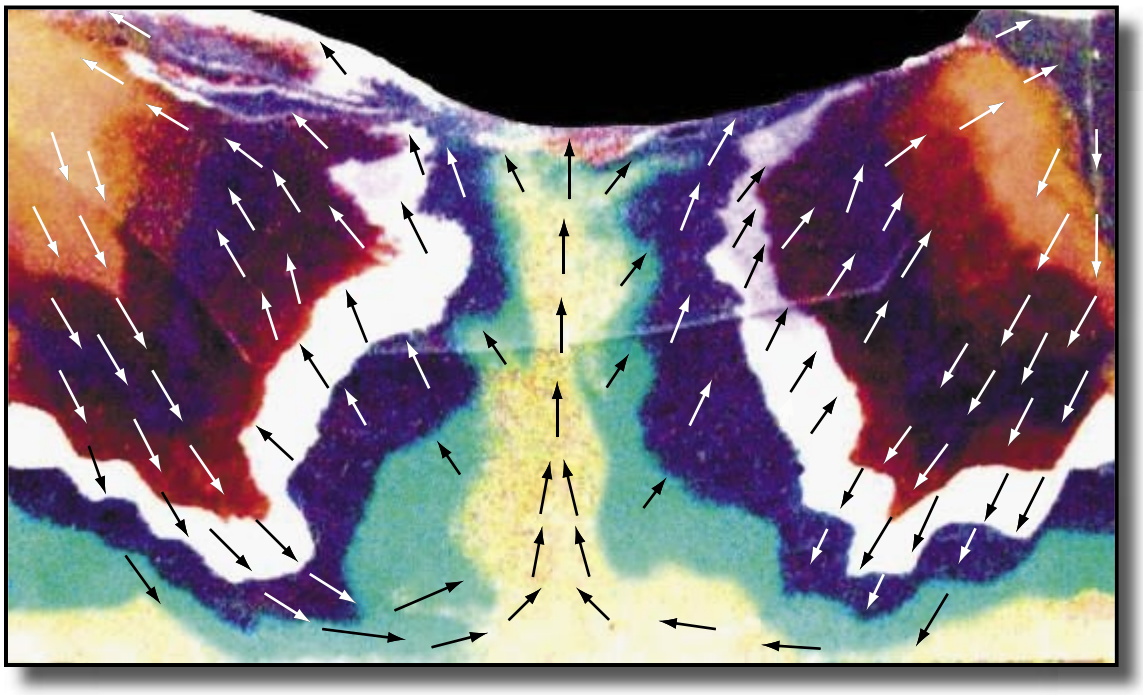

Figure 3. Cross section of epoxy-stabilized sand after cratering event. Arrows were added to show the direction of sand flow during the cratering event. Layers of colored sand were horizontal before the cratering occurred.

method was needed to observe cratering processes beneath the surface while they are occurring. The method was to use a sharp-edged acrylic sheet as the front wall of a sand box, aiming the jet so it straddled this sheet as shown in Figure 4. This split the jet in half so the cratering effects beneath the surface of the sand (under the back half of the jet) could be observed and recorded. The jets of gas were applied sometimes at high velocity and sometimes at low or moderate velocity. This produced two different regimes of cratering, (see Accomplishments). For the high-velocity regime, we used high-speed videography to capture the cratering event. For the low- to moderate-velocity regime, we used high-resolution videography.

The videography produced a very large set of raw data, so an automatic method of analy-

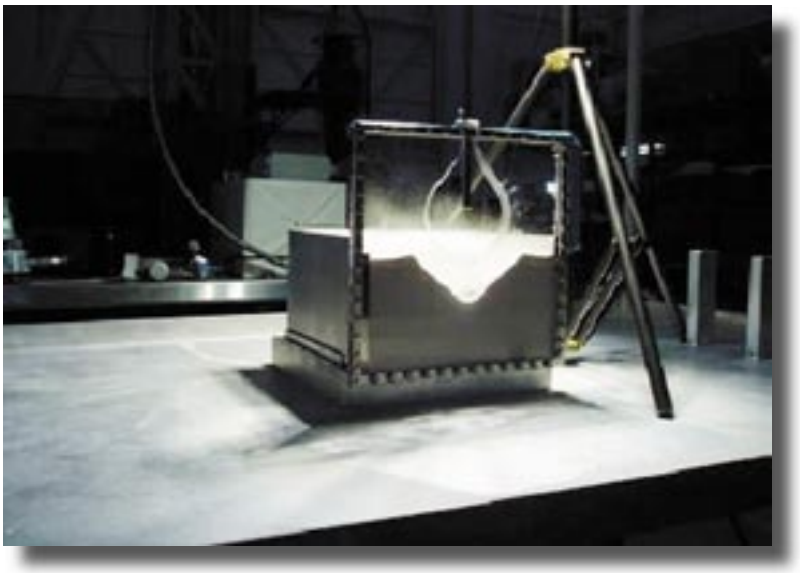

Figure 4. Cratering apparatus, showing crater formation along the transparent front wall of the box. The cutout in the clear sheet allows the gas to flow freely while keeping most of the sand inside the box.

sis was required. One of the team members developed a software algorithm to automatically analyze the video frame by frame throughout the duration of the test to extract crater shape and related parameters and to perform surface and volume integrals to calculate quantities of ejected sand. The user interface of this software is shown in Figure 5. This was applied only to the lower-velocity tests, which could be controlled more carefully than the chaotic high-velocity tests. This automatic video interpretation produced a very large set of semireduced numerical cratering data. We are continuing to analyze this large data set in Phase 2 of this project, but enough analysis has been completed to make several important discoveries about the cratering physics.

For the higher-velocity jets, the cratering process was more energetic and created

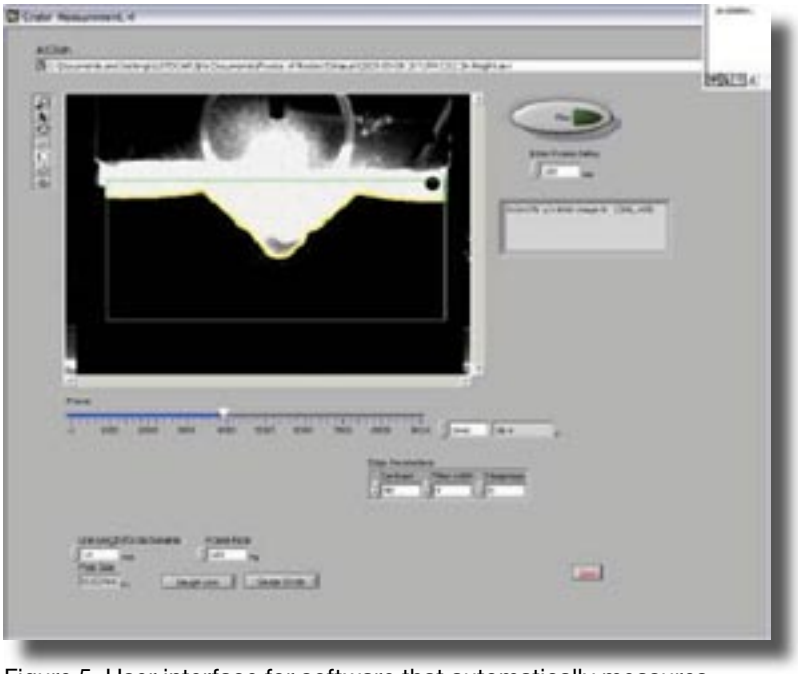

Figure 5. User interface for software that automatically measures crater shape, volume, etc., for every frame of video.

a deeper and narrower hole in the soil, with turbulent aggregative fluidization of the sand in the upper part of the hole. This produced a vastly different set of soil interactions than were observed with the low-velocity jets. The high-speed video from these tests was analyzed qualitatively and then by tracking individual sand particles and/or tracer particles that had been mixed with the sand. This allowed features of the sand's velocity field to be discerned.

There are reasons to believe that there are actually a number of different cratering regimes, not just the two (faster and slower regimes) described here. It was beyond the scope of this project to identify more regimes than these two simplest, subsonic regimes. It was also beyond the scope of this project to map the parameter space and draw the boundaries around the regions where these different cratering regimes occur.

To interpret the experimental results, computational fluid dynamics (CFD) simulations were performed using the software package C++, for both the lower- and higher-velocity cases. Crater geometries were scaled from the videos and used as the stationary boundary conditions for the CFD under the assumption that sand motion is slow relative to the gas attaining a steady-state flow condition. The boundaries were also treated crudely as impermeable with a no-slip condition, although we know that gases diffuse through the soil and that the gas velocity across a permeable medium does not strictly obey the no-slip condition at the surface. However, these approximations are quite adequate considering the high flow of the gas above the sand compared to the very restricted flow through the sand (in the bulk and near the surface), and so they provide a good first-order approximation to the physics.

The solution of the CFD provides pressures and shear stresses along the surface of the crater. Using these, it is possible to solve the flow of gas through the pore spaces of the sand. A FORTRAN program was written to do this, solving Darcy's equation. This produces the pressure and the velocity field for the gas in the sand, and the material derivative of the gas velocity produces its acceleration field. Dividing this by gas density produces the force on the gas, and by Newton's Third Law the negative of that force field is the drag force experienced by the sand. These drag forces provide a qualitative understanding of why the sand flows as it does around the bottom and sides of the crater (Figure 6). In ongoing work, we are using these drag forces, along with boundary forces on the surface of the crater, to solve the stress tensor field everywhere inside the sand. Using constitutive laws, we can then quantitatively predict the flow of sand under and around the crater.

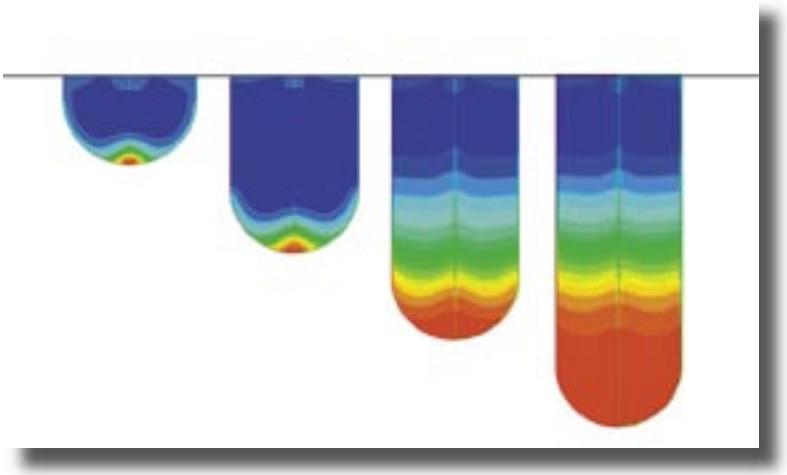

Figure 6. A sequence of CFD simulations during crater formation, showing the gas pressures developed in the crater. Red is higher pressure, and blue is lower. Note that the high-pressure gradients are in the tip of the crater when the crater is small, but along the sides of the crater when it gets deeper. In the deepest crater, there is a large region of stagnant gas in the crater's tip.

Accomplishments

In the tests for the fast regime, we discovered that the predominant cratering mechanism had been misinterpreted during the Apollo and Viking programs. It was believed at that time that the stagnation pressure of the jet impinging on the surface could exceed the bearing capacity of the soil and mechanically push the soil downward. The driving force was assumed to be at the surface of the sand and transmitted into the bulk via stresses in the granular backbone of the packing. The sand's velocity field under the surface was thought to be very similar to the field that results in a cone penetration test; that is, the sand was thought to flow perpendicularly away from the surface of the crater, going down, out, and then up again at some distance from the crater. This process was expected to be enhanced by the diffusion of the gas into the pores of the sand, which by Terzaghi's effective stress hypothesis would reduce the shear stress of the soil and allow it to fail in the typical cone penetration geometry more easily.

While some aspects of that description are correct, it contains one major flaw that has great implications for understanding the plume-soil interactions—confusing the effect of the diffused gases with Terzaghi's effective stress hypothesis. In that hypothesis, the fluid in the pore spaces is essentially static and is hydrostatically supporting part of the stress in the material, stress which developed from forces applied at the surface. In granular cratering, on the other hand, the fluid in the pore spaces is highly dynamic, and it is the drag of that fluid in the bulk of the sand that applies the stresses to the sand. Rather than supporting the load, the fluid imposes the load. In fact, if the diffusion of the gas is fast relative to the motion of the sand, then it has time to reach steady-state diffusion conditions and there is essentially no net pressure exerted on the top surface of the crater. The pressure just below the surface (in the pore spaces) will be almost equal to the pressure just above the surface. Hence, all the load is applied in the bulk by the fluid's drag, not at the surface by the fluid's pressure. The cone penetration model in that extreme would be completely wrong, and the geometry of sand flow different than expected. Figure 7 shows particle tracking of the sand around the crater's tip. We found that the sand flowed tangentially around the crater, not perpendicularly away from its surface as the cone penetration model had predicted.

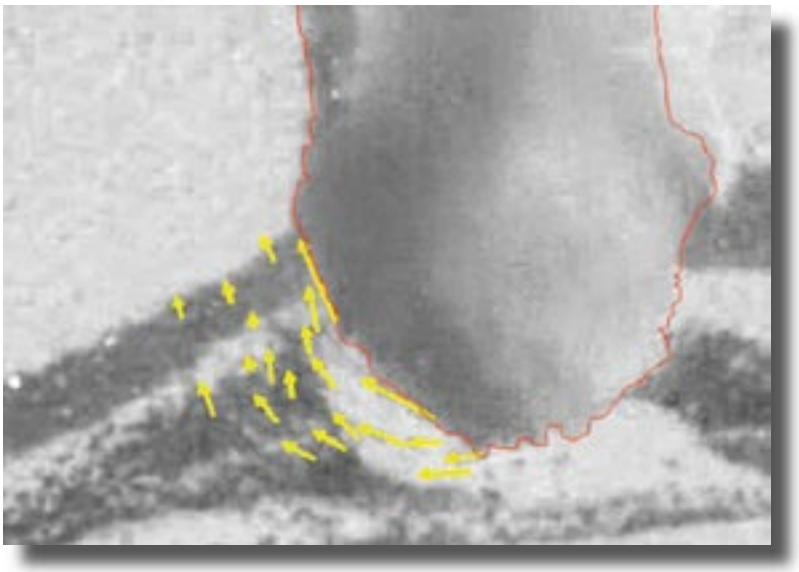

Figure 7. Crater (outlined in red) in white sand with black sand layers. Yellow vectors are the velocities of individual sand particles measured over a small increment of time. Particles travel in the tangential direction around the crater, not in the perpendicular direction as predicted by the theory during the Apollo era.

This discovery explains two things. First, we observed during crater growth in this fast regime that no sand was being scoured away from the bottom of the crater, yet the crater continued to grow. At first, we did not know how this could occur; but then we noted that the sand shears in bulk around the tip of the crater (as shown in Figure 8) to a location that is higher up the sides of the crater, and only when it gets to this higher location does it exit into the crater, where it gets carried away by the gas. Second, in the test shown in Figure 3 and in other tests, we noted that layers of colored sand were deformed upward instead of downward as the crater penetrated through them. This is because the crater grows not by downward mechanical penetration but by the upward fluid-driven shearing. In the test represented in Figure 3, after the jet was shut down, the crater collapsed, leaving no evidence of the deep hole that had been excavated through this shearing process. The layers of sand that had been dragged upward by the gas collapsed into the central core, leaving the form shown in the figure, with just a shallow crater visible at the top. Likewise, in tests during the Apollo era, there was no knowledge that such deep excavation was occurring beneath the soil. All that was known was the shallow crater left over at the end of the test. We now realize that most of the physics occurs deep beneath the soil by diffusive shearing, not in a shallow surface crater by bearing capacity failure.

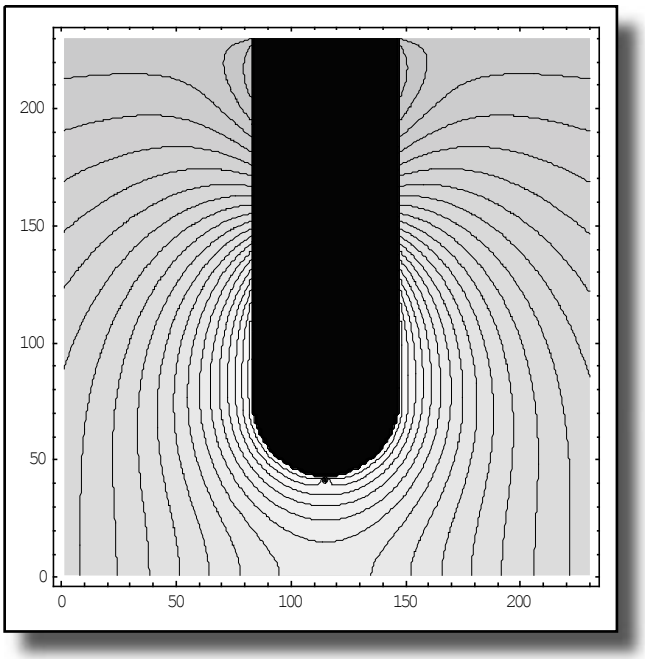

Figure 8. Lines of constant pressure within the sand around the crater due to diffusing gases. The crater itself is shown in black.

To be more precise, in most tests, we see a combination of bearing capacity failure and diffusive shearing. The combination depends on how fast the gases diffuse into the soil compared to how quickly the undiffused pressure drives the soil mechanically from above. For impermeable soil with a very high-velocity jet, bearing capacity would predominate (assuming the pressure is actually sufficient to overcome the soil's bearing capacity). For very permeable soil or a lower-velocity jet, the diffusive shearing would predominate. Most cases will exist on a continuum between the two extremes, with particle motion around the tip of the crater being neither perfectly perpendicular nor perfectly tangential to the crater's surface, and this is what we observe.

This diffusion-driven shearing will have an effect on lunar cratering, even though lunar cratering will not excavate a deep hole, as we have seen in these tests. (The lunar soil has extremely high shear strength and has low gas permeability because of extremely high compaction at those depths.) The relevant effect will occur in the shallow layer of loose particles at the surface. As the surface jet spreads out from the stagnation region, scouring particles into a high-velocity spray, the recoil of the gas molecules from the particles will inject pressure into the pore spaces. This static pressure will be rather high because of the extremely high dynamic pressure of the plume. It will have a gradient in the radial direction because the ground jet becomes less dense as it spreads out radially. These gradients will drive gas diffusion tangential to the surface, and the drag of this diffusion will contribute to the fluidization and erosion of the top layer of soil. Thus, an accurate prediction of lunar-soil erosion must account for this newly recognized part of the physics.

In the tests for the slow regime, the main discovery is that the rate of crater formation is controlled by the balance of two competing effects: the rate of soil ejection from the crater and the rate of soil recirculation back into the crater. To our surprise, we found that although the rate of crater growth continually slows during the crater formation process, the rate of soil ejection is essentially constant. It is not the rate of ejection, but the increasing rate of recirculation that governs the crater's growth. This is because recirculation is a function of crater shape and size. As the crater grows, increasing amounts of sand cannot ultimately escape, so the net rate of growth continually slows and eventually stops.

We observed that the forming crater evolves into a complex structure consisting of (1) an inner crater that provides the excavation surface, (2) an outer crater at the angle of repose that sports a rolling layer of grains flowing back to the inner crater, (3) a mass of airborne grains recirculating inside the hollow, and (4) transient dunes of locally deposited material around the outer lip. The complex sequence of forms is shown in Figure 9.

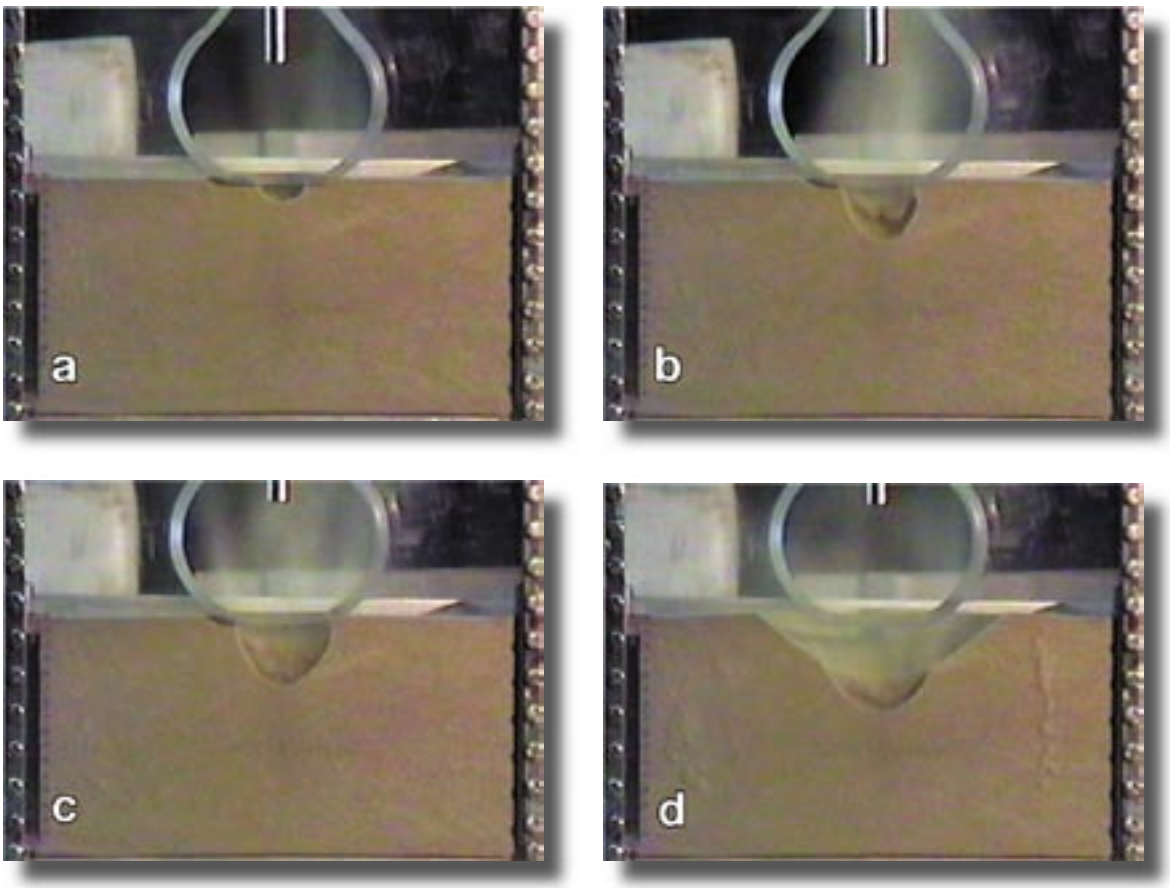

Figure 9. Sequence of crater growth. (a) Erosion/fluidization forms a cup. (b) Recirulation cell consisting of airborne grains forms inside the cup. (c) Crater widens until traction along inner surfaces is insufficient to maintain steep sides. (d) Sides collapse to the angle of repose, producing a recirculating surface layer of rolling grains that return to the inner crater.

Grains are ejected from the crater through the following mechanism. First, diffusion-driven shearing sometimes occurs just beneath the tip of the crater where the gases are stagnant (Figure 9a), but viscous surface erosion occurs over the rest of the inner cup, rolling the grains uphill until they reach the top of the inner cup. This was observed in the tests and confirmed by the CFD simulation shown in Figure 10, where maximum pressure gradients are beneath the tip but high velocities are everywhere else. Second, the actual erosion of sand, where the sand becomes airborne, occurs at the lip at the top of the inner cup. This too was observed in the tests and confirmed by the CFD simulation shown in Figure 10, where the maximum gas velocity occurs at the lip. Third, as the inner cup grows, as shown in the sequence of Figure 9, it becomes deeper with steeper sides. The gas traction at the lip provides the force balance to maintain the steep slopes, much steeper than the sand's natural angle of repose. Eventually, as the cup widens, the gas traction at the lip becomes insufficient to maintain the steep slope and it begins to avalanche, forming the outer crater. This outer crater is completely shielded from the gas flow, as shown by the CFD in Figure 10, so gravity dominates the slope. We confirmed through measurements that this slope is the usual angle of repose for the soil. Once these outer crater processes begin, two mechanisms will deliver sand to the erosion spot at the lip of the inner crater. The first is shearing and rolling grains in the inner cup to bring them up to the erosion spot. The second is the avalanching in the outer crater to bring them down to the erosion spot.

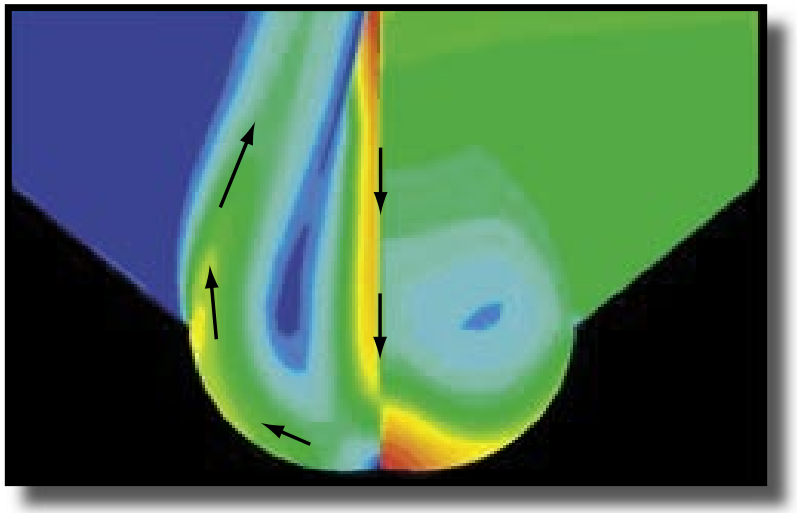

Figure 10. (Left) Velocity of jet in slow-regime crater. Velocity from fast to slow is shown by red to yellow to green to blue. Arrows indicate direction. Maximum erosion is at the lip of the inner crater (yellow region). (Right) Pressure due to jet from high to low is red to blue as before.

After being ejected at this lip, the grains recirculate through the following mechanisms. First, an ejected grain may be placed into a trajectory that drops it directly back toward the inner crater. Such grains appear to be turned by the gas flow and recirculated before they ever touch the surface again. This is aerial recirculation. Second, some grains fall onto the angle of repose of the outer crater and join the avalanching grains of that region to roll toward the erosion spot, where they are ejected again. This is funnel recirculation. Third, some grains fall just outside the outer crater, where they form small dunes. However, these grains obtain only a temporary respite from the recirculation because the outer crater widens and eventually reingests these dunes. This is deposit recirculation. Finally, some grains fall so far away that they are never reingested. These grains are the ones that escape the crater.

The volumetric growth of the crater is the difference between the volume of sand ejected and the volume of sand recirculated (of course, taking into account the packing fraction of sand when it is in a dense state). Because the crater width is growing, an increasing fraction of ejected grains are recirculated, slowing the net crater growth. When the two rates become equal, crater growth stops at the steady-state size. Grain ejection and recirculation continue in the steady state.

It was found that over the time scales of the experiments, the crater depth grew as the logarithm of time, scaled by just two constants (scaling time and scaling depth). This is shown in Figure 11. In the experiments where the gas densities and velocities were varied, the depth scale was unchanging, but the time scale varied proportionately to density multiplied by the square of the velocity (i.e., proportionately to the dynamic pressure of the jet).

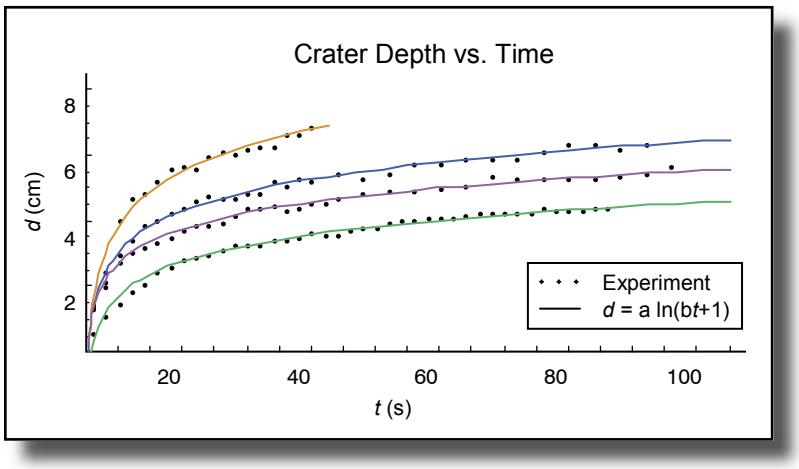

Figure 11. All cratering events are governed by a simple differential equation that universally produces a logarithmic growth in crater depth. This logarithm is scaled by two constants: a and b. After a long time, the crater will depart from this trend as it reaches its maximum size.

On closer examination, the crater depth oscillated around this logarithmic trend. The oscillations were found to be the result of bistability in the slope of the outer crater. The angle of repose (the angle after the avalanche) is slightly less than the angle of failure (the angle just before the avalanche). The outer crater slope oscillated between these two angles, and when avalanching occurred, the influx of material toward the inner crater slowed crater growth temporarily. This is shown in Figure 12.

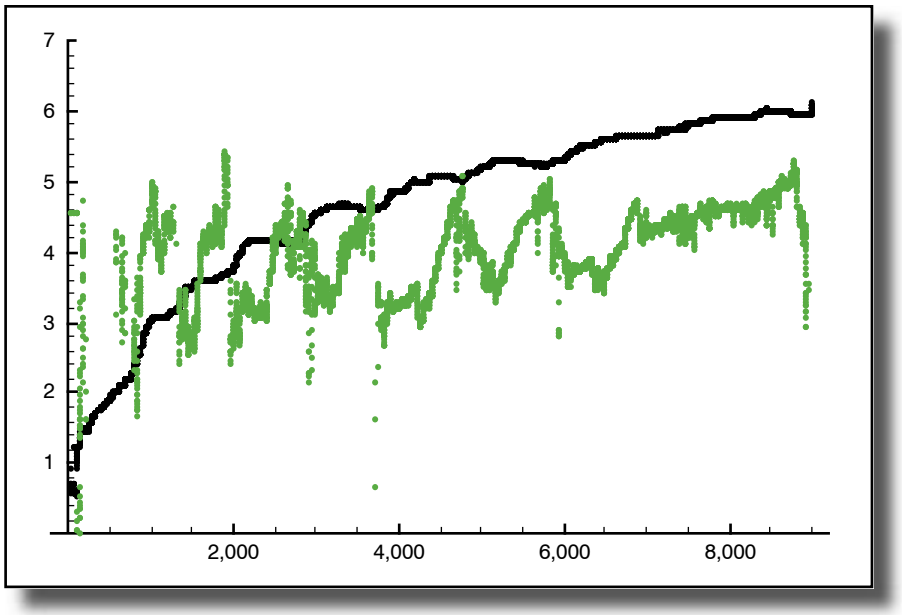

Figure 12. Black: Crater depth versus time, showing oscillations around a predominantly logarithmic trend. Green: slope of the outer crater, showing bistability and avalanching that correlate to the oscillations in crater depth.

Other crater parameters were studied, and relationships between them were worked out. This produced the picture that crater formation is largely controlled by the feedback of its own emergent geometry. Dynamically, its rate is determined simply by the dynamic pressure of the jet.

This project also organized and hosted the inaugural "Workshop on Granular Materials in Lunar and Martian Exploration" at Kennedy Space Center, which sought to identify the important differences between granular-material behaviors on the Earth and on the Moon or Mars and to identify the granular-material technology needs for space exploration.

Abstracts

Metzger, Philip, Carly Donahue, Christopher Immer, and Bruce Vu, "Crater Formation From a Jet of Gas Impinging on Sand" (manuscript in preparation for a fluid dynamics journal).

Metzger, Philip, Carly Donahue, Christopher Immer, and Bruce Vu, "The Interaction of Rocket Engine Exhaust with the Lunar or Martian Soil: Implications from Recent Experiments" (manuscript in preparation for a space exploration journal).

Talks/Presentations

Donahue, Carly, Philip Metzger, Christopher Immer, Brian Larson, and Alex Taylor, "Functional Scaling for the Cratering of a Granular Surface by an Impinging Jet," *ASCE Earth & Space 2006*, League City, Texas, March 5–8, 2006.

Metzger, Philip T., "Rocket Exhaust Cratering: a Serious Challenge for Space Exploration," *Proc. 1st Workshop on Granular Materials in Lunar and Martian Exploration*, Kennedy Space Center, Florida, February 2–3, 2005.

Metzger, Philip T., "Challenges in predicting planetary granular mechanics," invited talk, *Planetary and Terrestrial Mining Sciences Symposium*, Sudbury, Ontario, Canada, June 5–8, 2005).

Metzger, Philip, Christopher Immer, and Carly Donahue, "Dynamical Scaling of Jet-Induced Crater Formation in a Granular Bed," *5th World Congress of Particle Technology*, Orlando, Florida, April 24–27, 2006.

Metzger, Philip, Christopher Immer, Carly Donahue, and Robert Haehnel, "Rocket Exhaust Cratering: Transient Effects from Abrupt Application of Jet," *ASCE Earth & Space 2006*, League City, Texas, March 5–8, 2006.

Status of Investigation

Phase II of the project has commenced.

Planned Future Work

Future testing includes the use of supersonic jets (from solid rocket motors) and the development of a flow code that combines computational fluid dynamics with an Euler-Eulerian solver for the particulates.

Funding Authorized for FY 2005: CDDF – $100K

Completion Date: September 2005

Smart Coatings for Corrosion Sensing and Protection

Leader: Luz Marina Calle, Ph.D., NASA
Wenyan Li, Ph.D., NASA Postdoctoral Fellow

Initiation Year: FY 2005

Purpose

This research is aimed at developing "smart coatings" to detect and control corrosion at an early stage to prevent further corrosion.

Background

NASA began corrosion studies at Kennedy Space Center (KSC) in 1966 during the Gemini and Apollo programs with the evaluation of coatings for long-term atmospheric protection of carbon steel. The environment near the KSC launch pads has been documented by the American Society of Materials (ASM) as one of the most corrosive naturally occurring environments in the world [1]. With the introduction of the Space Shuttle in 1981, the already highly corrosive conditions at the launch pads were rendered even more severe by the acidic exhaust from the Solid Rocket Boosters. In the years that followed, numerous studies have identified materials, coatings, and maintenance procedures for launch hardware and equipment exposed to the highly corrosive environment at the launch pads.

An extensive study by the U.S. Federal Highway Administration shows that the total annual estimated direct cost of corrosion in the United States is $276 billion, approximately 3.1 percent of the nation's gross domestic product [2]. About one-third of corrosion failures are due to localized corrosion, pitting corrosion, and crevice corrosion caused by pitting [3]. Numerous studies have been carried out to minimize losses and failures caused by corrosion, and significant progress has been made in prolonging the service life of materials. When localized corrosion occurs without being detected, the result can be a disastrous failure.

NASA uses different types of coatings to protect flight hardware, launch pad structures, and ground support equipment. Barrier coatings, such as epoxies and urethanes, are used to isolate the surface of a metal structure from the corrosive environment. Conversion coatings, such as the Super Koropon primer used to protect areas throughout the Space Shuttle Orbiter, convert the surface into a hard, durable, corrosion-resistant layer. Sacrificial coatings, such as the zinc-rich primers used at the launch pads, offer corrosion protection by corroding in preference to the carbon steel. Smart coatings represent the state of the art of coating technology. These coatings sense the environment and provide an appropriate response.

Smart Coatings

The intelligence of the so-called smart coatings relies on their capability to respond to physical, chemical, or mechanical stimuli by developing readable signals, which may often actuate, in addition to such simple sensing, corrective actions as self-mending or self-healing [4].

The following are some of the smart coatings under intensive study for various applications: instant chameleonic coating for combat vehicles [5], tribological coatings with adjustable "skin" chemistry for adaptation to different environments [6], bioplastic film with embedded antibodies capable of detecting and capturing bacteria [7], sensing film containing planar sensors for *in situ* monitoring of engine components for surface cracks and plastic deformation [8], and a functionally gradient overlay coating system designed to provide high-temperature corrosion protection over a wide range of operating temperatures [9].

Smart Coatings for Corrosion Sensing

Smart coatings for corrosion-sensing purposes rely on a material undergoing a transformation through its interaction with the corrosive environment. Such transformations can be used to indicate and detect corrosion damage. Ideally, the sensing function could be integrated with additional actuation and control functions designed to control corrosion damage [10]. Since the corrosion of metal is an electrochemical process, most of the relevant corrosion sensors include the following features:

- paint systems with color-changing compounds that respond to the pH changes that result from corrosion processes [11];
- changes of coating compounds from nonfluorescent to fluorescent states upon oxidation or complexing with metal cations [12–15]; or
- release of color dyes on coating damage from incorporated dye-filled microcapsules [16].

Self-Healing Coatings for Corrosion Protection

The best coatings for corrosion protection provide not only barriers to the environment, but also a controlled release of a corrosion inhibitor, as demanded by coating damage and the presence of a corrosive environment. Past examples include coatings containing metallic zinc (such as the zinc-rich paint systems used at the KSC launch pad structures) and chromate [17].

Chromate-containing coatings (CCCs) release the inhibiting hexavalent chromium when exposed to a corrosive environment [18–22]. Release of this species passivates metal exposed at defects in the coating. The overwhelming success of chromate-containing paints and conversion coatings used over the last century and into the 21st century, despite the environmental hazard, can be attributed to their performance as damage-responsive materials. Xia et al. have reported evidence that the coatings release the corrosion-inhibiting hexavalent chromium, Cr(VI), not simply by mass-action dissolution from the coating, but as a result of electrochemical corrosion reactions that concentrate alkali at cathodic sites, thereby stimulating the chromate release [21]. Unfortunately, hexavalent chromium has limited use for corrosion protection because of its toxic and carcinogenic properties. Replacements must be found, yet duplicating the efficacy of CCCs is a considerable challenge [23].

Besides chromate, another damage-responsive coating technology that remains viable for certain applications is metallic zinc. Metallic zinc not only acts as a sacrificial material to electrochemically protect the substrate, but it also generates zinc ion, Zn(II), a product that inhibits corrosion. Galvanized coatings are thus ideally damage-responsive in that they will polarize a defect in the coating, and in so doing, release a corrosion inhibitor. The cost and weight of these coatings and their general ineffectiveness for the lighter alloys, along with some concern for their environmental effects, make them less than ideal for many aerospace applications.

Different approaches (such as semiconducting coatings that would provide an electronic barrier at the metal coating interface [24, 25], and sol-gel coatings that include corrosion inhibitors in their controllable micro- or nanostructure [26] have been used to develop a damage-responsive protective coating. J. Osborne notes the similarity of the physical chemistry of sol-gel film formation and that of a chromate conversion coating [27].

Yang and van Ooij have encapsulated soluble corrosion inhibitors, using plasma polymerization [28]. Such inhibitors can be incorporated into paints similar to the way in which conventional solid inhibitors are used. The inhibitor is slowly released as it diffuses through the thin polymer film. While this provides a mass-action-governed release mechanism, it is a less selective process for damage-induced activation. Some coatings may inhibit corrosion by stimulating the formation of protective biofilms. For example, a recent note suggests that biogenetically engineered bacteria may be able to release corrosion-inhibiting species such as certain polypeptides and polyphosphates [29].

Ion exchange corrosion-inhibiting pigments have been considered for a number of years. The most recent work was that performed by Williams and McMurray, who demonstrated that hydrotalcite, rehydrated in the presence of inhibitor anions such as phosphate and chromate, provides excellent inhibition for filiform corrosion [30]. The ion exchange pigments, when formulated in paint, work to limit filiform corrosion in at least two ways: by lowering the chloride activity through ion exchange and by buffering the anodic head of the filiform. The most studied materials for this application are probably conducting polymers, and different inhibition mechanisms are being considered [31–34]. DeBerry et al. demonstrated that in the conducting, oxidized form, such materials could anodically protect stainless steel in sulfuric acid by maintaining its potential in the passive region [35].

Two smart-system prototypes with self-healing properties have been reported by Kumar and Stephenson [16]. Both prototype coatings contain self-healing microcapsules whose core constituents can be released when they are ruptured. The microcapsules in the first prototype contain film-forming compounds (healants) and corrosion inhibitors, whereas those in the second prototype contain calcium hydroxide ($Ca(OH)_2$), which can react with carbon dioxide (CO_2) in the air and form a thin film of calcium carbonate ($CaCO_3$). This film acts as a healant to restore the coating integrity.

The smart coating being developed in this project will combine the advantages of corrosion sensing and corrosion protection by using pH-triggered release microcapsules for early detection of corrosion and for corrosion protection [36].

Approach

Localized Corrosion

Corrosion is largely an electrochemical phenomenon because, in most cases, it involves the transfer of electrons between a metal surface and an aqueous electrolyte solution. For instance, when iron corrodes in nearly neutral environments, the typical electrochemical reactions are

Cathodic reaction: $O_2 + 2H_2O + 4e^- \rightarrow 4OH^-$

Anodic reaction: $Fe \rightarrow Fe^{2+} + 2e^-$

In cases of localized corrosion, such as pitting corrosion, the anodic reaction happens in a small, confined area and the metal ions produced are precipitated as solid corrosion products, such as $Fe(OH)_2$ (often further oxidizes to $Fe(OH)_3$), which covers the mouth of the pit (Figure 1):

$$2Fe^{2+} + 2H_2O + O_2 + 4e^- \rightarrow 2Fe(OH)_2$$

$$4Fe(OH)_2 + 2H_2O + O_2 \rightarrow 3Fe(OH)_3$$

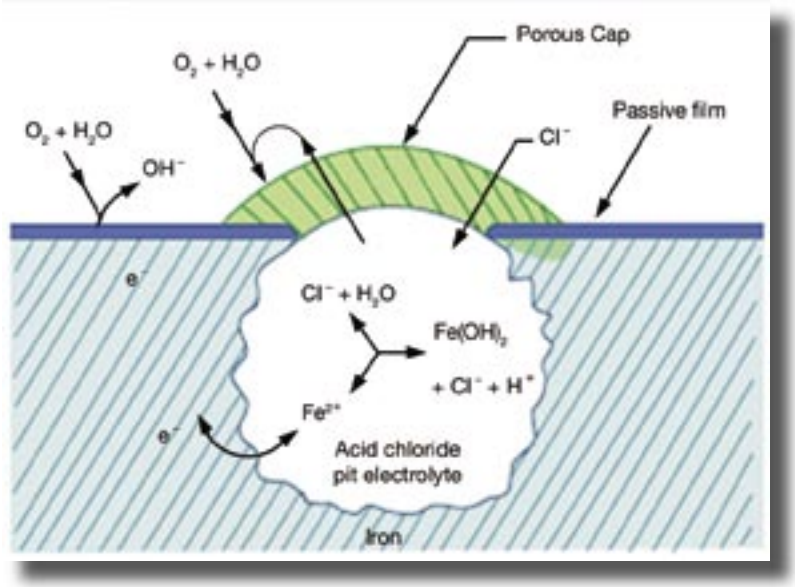

Figure 1. The electrochemical cell setup between anodic and cathodic sites on an iron surface undergoing pitting corrosion.

This covering traps the solution in the pit and allows the buildup of hydronium ions, H+, through a hydrolysis reaction:

$$Fe^{2+} + 2H_2O \rightarrow 2Fe(OH)_2 + 2H^+$$

Then, chloride or other damaging negative ions diffuse into the pit to maintain charge neutrality. Consequently, the solution in the pit becomes highly acidic, lowering the pH. The overall effect is that while localized corrosion happens, the anode area often has an acidic pH and the cathode area has an alkaline (higher) pH [37].

Figure 2a shows the alkaline region around pits (blue band). Figure 2b is a schematic representation of the anodic and cathodic areas present in localized corrosion with their respective pH values.

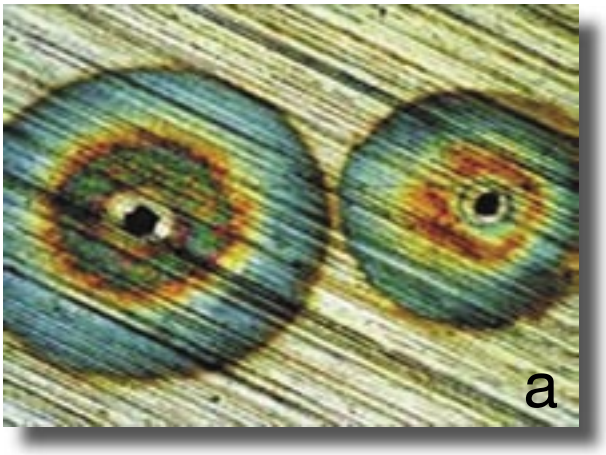

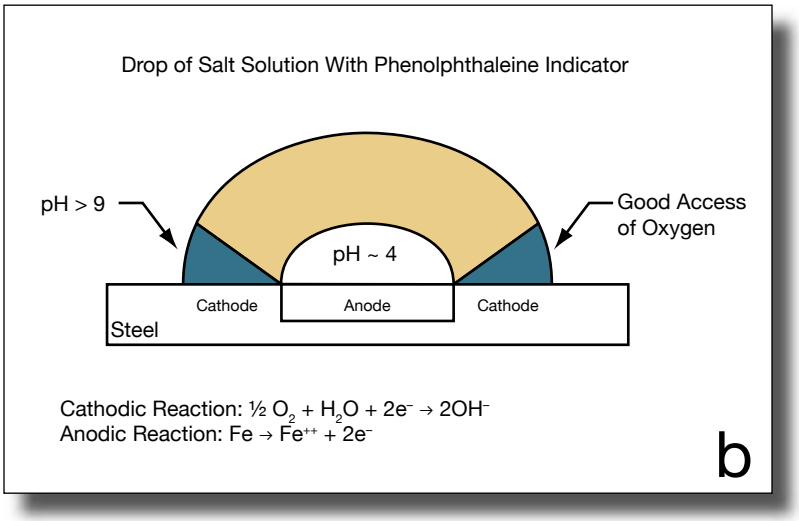

Figure 2. (a) Typical pitting corrosion <http://www.ibwk.baum.ethz.ch/>; (b) Schematic illustration of an Evans drop test [37].

ph-Triggered Release Microcapsules

The critical component of this new smart coating system is the pH-triggered release microcapsules. Similar microcapsules have been developed for pesticide applications because the targeted insects have an alkaline environment in their gut. These microcapsules can be formed to 1 μm or bigger, and their content can be completely released in a relatively short time (e.g., 4 hours) when the environmental pH is around 8 to 10, or 1 to 4. These pH ranges match those present in localized corrosion conditions in nearly neutral environments.

pH-triggered release microcapsules can be used to deliver healing agents to localized corrosion sites to terminate the process at its early stage. They can also be used as corrosion indicators themselves by releasing dyes at the localized corrosion sites. The dyes can be color or fluorescent, with or without pH sensitivity. A current study on corrosion sensing is based on incorporating pH-sensitive fluorescent dyes directly into paints. This approach has encountered many challenges, such as the low solubility of the dyes, the low pH sensitivity of the dyes, and the loss of fluorescence in the cured coatings [14]. The use of pH-triggered release microcapsules can overcome these problems because the microcapsules are pH-sensitive and are able to act as corrosion indicators themselves.

The type of smart coating being developed in this project uses pH-triggered release microcapsules. The microcapsules contain selected film-forming compounds (acrylic varnish or other suitable clear varnish) and corrosion-inhibiting compounds (such as camphor or polyamine fatty acid salts in a solvent), as well as a regular pH indicator, such as phenolphthalein, which changes color over the alkaline pH region, 8.2 to 10. The microcapsules can be mixed with clear or light-colored paint so that the color changes can be easily observed.

Experimental Results

Three steps are involved in the formation of the smart coating. The first step is the formation of the microemulsion. Normally, a surfactant is needed to reduce the interfacial energy so the microemulsion can form. Various surfactant mechanisms can be used for this propose, including surfactant stabilizers, emulsifiers, polymeric stabilizers, and thickening agents. By adjusting the amount of various surfactants and the stirring speed, it is possible to form stable microcapsules with a desired size distribution. The second step is the formation of the solid polymer capsule shell through interfacial polymerization. In our process, the prepolymer and cross-linker are both dissolved in the oil phase, and the catalyst of the polymerization reaction, an inorganic acid, is added to the water phase. Upon heating, the polymerization reaction between the prepolymer and cross-linker takes place at the interface between the oil and the water phase, where the catalyst is available. The reaction stops when the polymer shell grows to a certain thickness and density. The last step is to incorporate these microcapsules into a coating system so they can be applied to a metal surface.

Preparation of Microcapsules

The microcapsules are synthesized using the Zenaca microencapsulation process, wherein the polymer wall is formed by the interfacial polymerization and condensation of a mixture of a butylated urea-formaldehyde prepolymer and a crossing agent containing –SH and/or –OH groups. The structure of a typical butylated urea-formaldehyde prepolymer with an average molecular weight of ~1,000 is shown in Figure 3. A commercial product is usually a mixture of prepolymer with certain molecular weight distribution.

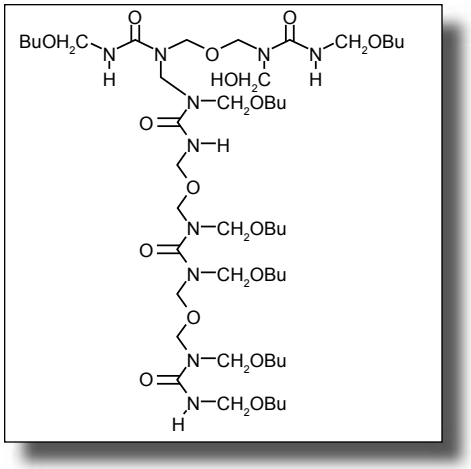

Figure 3. Structure of a typical butylated urea-formaldehyde prepolymer with an average molecular weight of ~1,000.

The reaction between the crossing-linking agent, such as therathioglycolate (PTT), and the prepolymer is presented in Figure 4. The pH sensitivity of the resulting structure lies in the ester or thioester group from the crossing-linking agent. They can be cleaved through the nonreversible hydrolysis reaction under basic conditions.

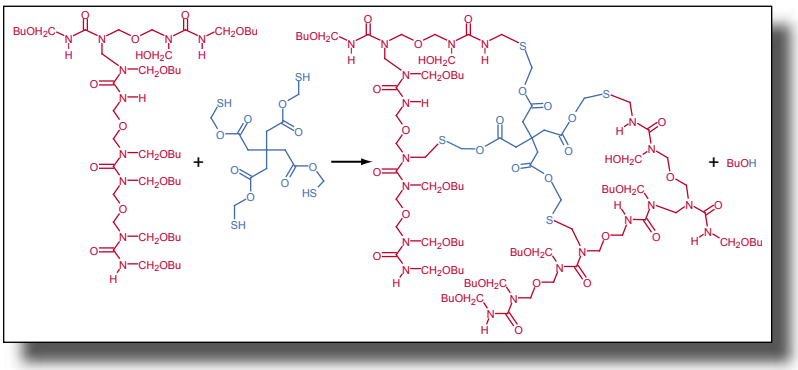

Figure 4. Reaction between the crossing-linking agent and the prepolymer.

The detailed experimental procedure is as follows:

a. An emulsion is formed by mixing an organic phase with an aqueous phase followed by stirring. The organic phase includes the corrosion indicator or inhibitor (in some cases, dissolved in a solvent, such as toluene), CYMEL U-80 (a butylated urea-formaldehyde prepolymer), and a cross-linking agent, such as PTT. The aqueous phase includes a protective colloid, an emulsifier, and an acid dissolved in water. The emulsion is prepared by dispersing the oil phase in the aqueous phase, using any conventional high-shear stirrer, until the desired consistency is achieved.

b. The resulting oil-in-water emulsion is then heated to 50 °C for up to 3 hours.

c. The resulting capsule suspension is removed from the heat, washed, separated from the liquid phase, and collected for further applications.

Two typical formulas for microcapsules containing pH indicators are shown in Tables 1 and 2. Xanthan gum is a high-molecular-weight polysaccharide (an anionic polyelectrolyte with a cellulose backbone and different side chains) often used as a thickener. Petro BAF is mainly made of sodium alkyl naphthalene sulfonate, known as a dispersing aid and wetting agent. Attagel, hydrated magnesium aluminum silicate, is commonly known as attapulgite clay and is used as a particle stabilizer. Reax 83A is a sodium salt of sulfonated modified Kraft lignin, used as a surfactant.

Table 1. Formula A

Cymel U-80 Prepolymer	3.85 g
2-Mercaptoacetate	0.95 g
Phenolphtalein	0.5 g
Toluene	31.4 ml
Xanthan Gum	0.028 g
Petro BAF Powder	0.06 g
Attagel 40	0.6 g
Reax 83A	0.83 g
Water	26.1 ml

Table 2. Formula B

Cymel U-80 Prepolymer	1.9 g
2-Mercaptoacetate	0.48 g
Phenolphtalein	0.25 g
Toluene	15.7 ml
Isopropanol	8 ml
Xanthan Gum	0.028 g
Petro BAF Powder	0.06 g
Attagel 40	0.3 g
Reax 83A	0.83 g
Water	26.1 ml

Emulsion Studies

After the initial experiments, different formulations and conditions were varied to achieve the desired microcapsule size and size distribution. While a homogenous size distribution is normally preferred, different sizes might be required for different functions of the microcapsule system. For example, for corrosion indication, a size of about 20 to 40 µm is suitable, and for inhibitor releasing, a smaller size might be better. Another motivation for emulsion study is to increase the solubility of corrosion indicator or inhibitor in the oil phase. For example, the pH indicator, phenolphthalein, used for corrosion indication has a limited solubility in the oil phase. Its solubility in the oil phase was increased by adding ethanol to the system while keeping the emulsion system stable.

Through trial and error, an understanding of the microemulsion process was gained. Many factors, such as oil-to-water ratio, different surfactants, stirring speed, and stirring time, affect the stability and size of a microemulsion. However, the extent to which these factors influence the microencapsulation process varies. The oil-to-water ratio is important for the size distribution of the oil-in-water emulsion. There seems to be a top limit of oil-to-water ratio to get a stable and homogenous oil-in-water emulsion. There is a limit to the amount of oil that can be added to water to yield a stable oil-in-water emulsion. If too much oil is added, the system will be stabilized at a larger colloid size or will become unstable. Surfactants are critical for emulsification. Their amount in the system affects the size, size distribution, and stability of the emulsion system. In this system, it was determined that adjusting the amount of Attagel could change the size of the emulsion without affecting the size distribution. Other important factors for emulsification are the stirring speed and time. Stirring is important to initiate the emulsification process and bring it to stable stage in the presence of the surfactant. Normally, a higher stirring speed results in a smaller-size colloid. A certain time is needed for the emulsion to reach its stable stage and optimum size distribution.

Based on the understanding of the microemulsion process, different formulations can be chosen for different purposes. For instance, using a conventional high-shear stirrer at 800 to 1,000 rpm, microcapsules of Formula A are produced with an average diameter of 50 µm (Figure 5a). Using Formula B under the same conditions results in microcapsules with a smaller diameter: 25 to 30 µm (Figure 5b). Smaller microcapsules ranging from 5 to 10 µm can be obtained by increasing the amount of Attagel in Formula B.

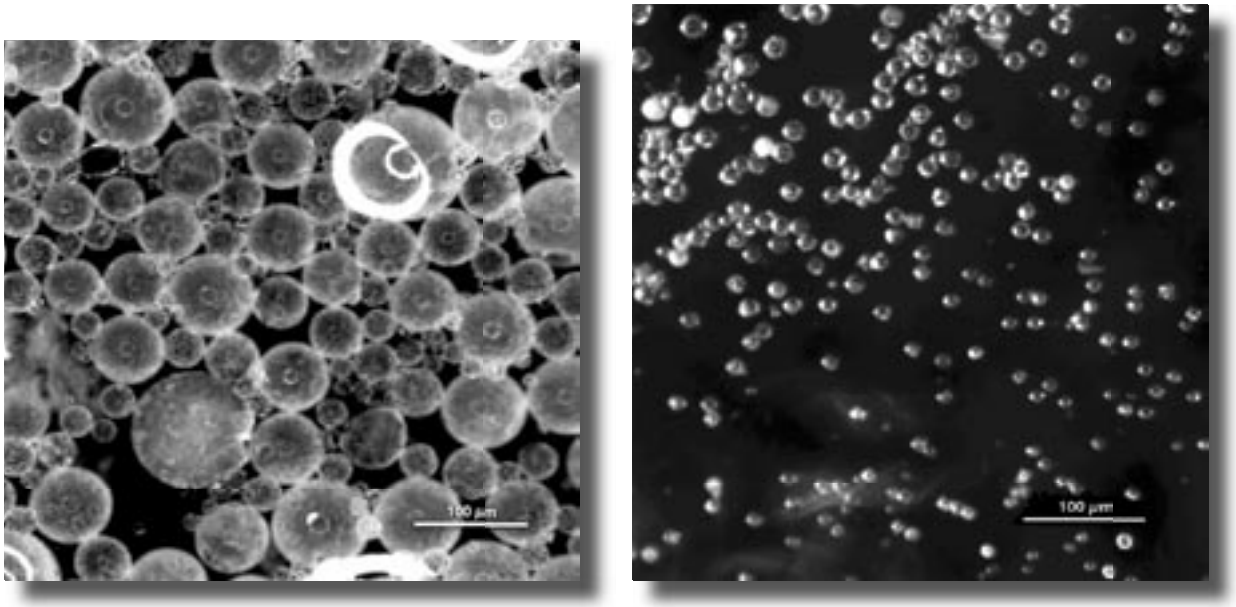

Figure 5. Microcapsules made using Formula A (left) and Formula B (right).

ph and Corrosion Sensitivity Studies

To increase the pH sensitivity of the microcapsules, that is, to make microcapsules that break down faster under basic pH conditions, two approaches are applied: increasing the cross-linking agent content and decreasing the thickness of the microcapsule wall. Increasing the cross-linking agent in the reactant will yield more ester groups in the wall structure. Decreasing the reaction time will result in a thinner microcapsule shell. These two factors will result in higher pH sensitivity. A thinner microcapsule shell also means low mechanical strength, a limitation that can affect certain applications. Figure 6 shows the color change of the indicator in the microcapsules upon exposure to basic pH conditions. The microcapsules in Figure 6a had thicker walls and fewer of the microcapsules released the indicator (as indicated by intense purple) compared to those in Figure 6b.

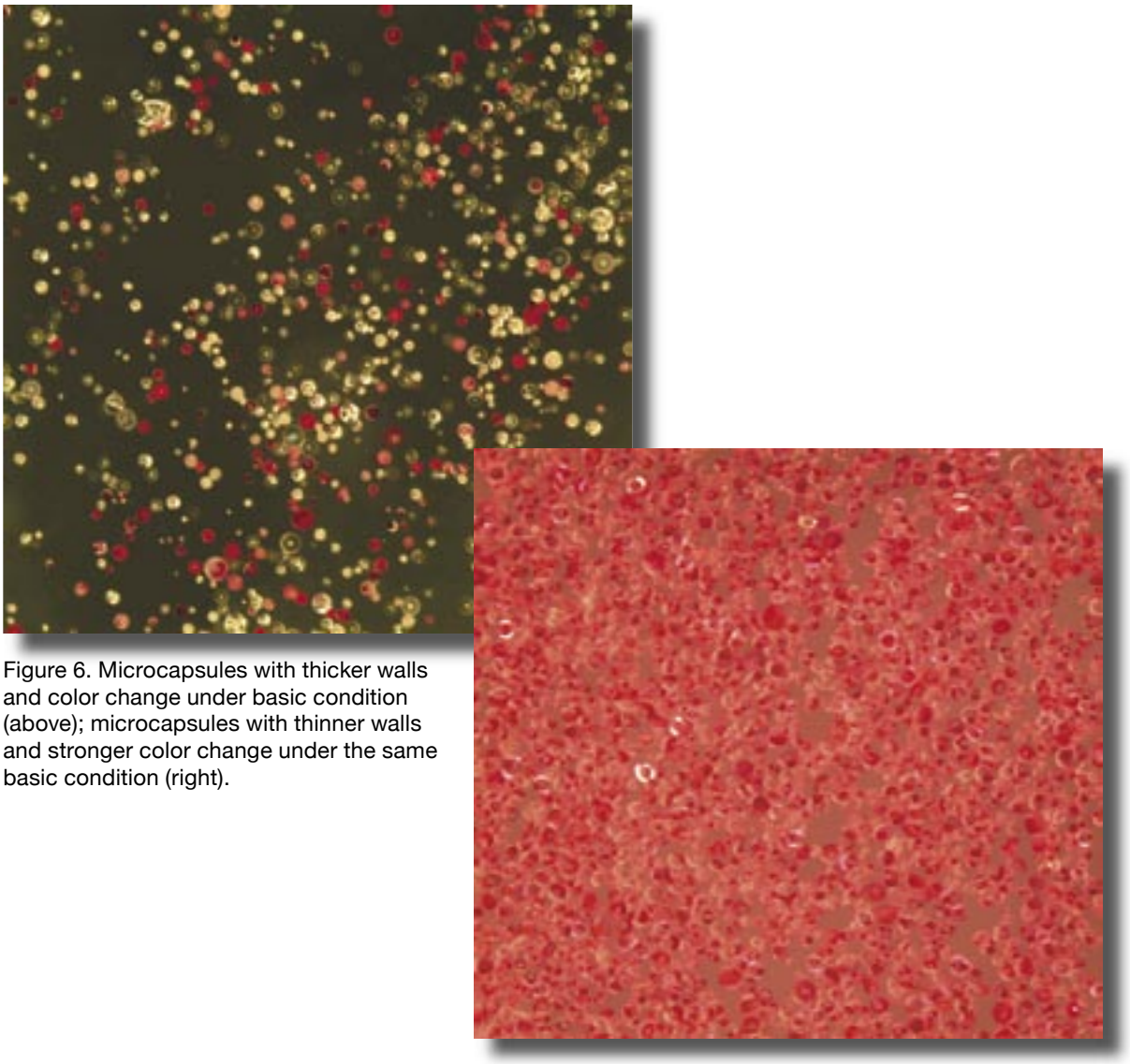

Figure 6. Microcapsules with thicker walls and color change under basic condition (above); microcapsules with thinner walls and stronger color change under the same basic condition (right).

After testing the pH sensitivity of the microcapsules, a simple test was performed on their corrosion indication ability. A drop of water containing microcapsules with pH indicators was placed on a carbon steel panel. Based on prior experience, a rust spot would form under the water drop. This is a simple way to observe corrosion on a metal surface. Figure 7 shows that the microcapsules changed color, thus indicating the presence of localized corrosion.

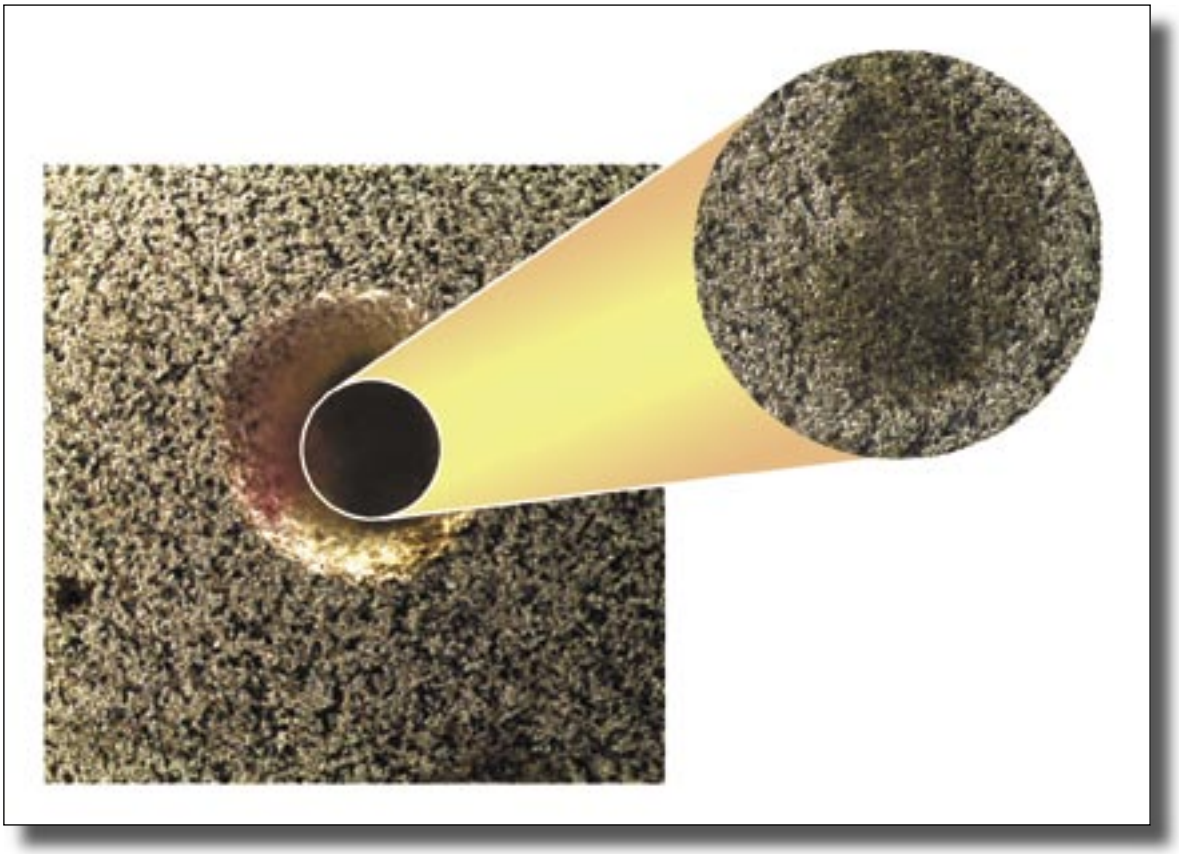

Figure 7. pH-indicator-containing microcapsules indicating corrosion site through color change at cathodic area.

Microcapsule Dispersion System

While these microcapsules perform the desired controlled-release and indication functions, the ultimate goal of this project is to incorporate these functions into a paint product. However, more work is needed to move from laboratory research to a commercially available product. We tested some commercial paint systems for their compatibility with the microcapsules, and one paint system, AquaSurTech D45-AMS system 9 (D45), showed very good results.

To be considered compatible with a paint system, the microcapsules must (1) not break during high-shear mixing, (2) not clog the spray gun or be sprayed improperly, and (3) keep the same functionality in dried paint that they exhibited in the colloid system or dried-powder form. The first two concerns are related to the size and mechanical strength of the microcapsule. Microcapsules that are about 20 μm or smaller can easily be mixed with commercial paint products by conventional high-shear stirring and then applied to metal panels with a spray gun. Figure 8 shows microscope photography of panel surfaces sprayed with paint containing microcapsules and with paint not containing microcapsules. The microcapsules are visible in the paint matrix, but not more so than the other solid paint particles.

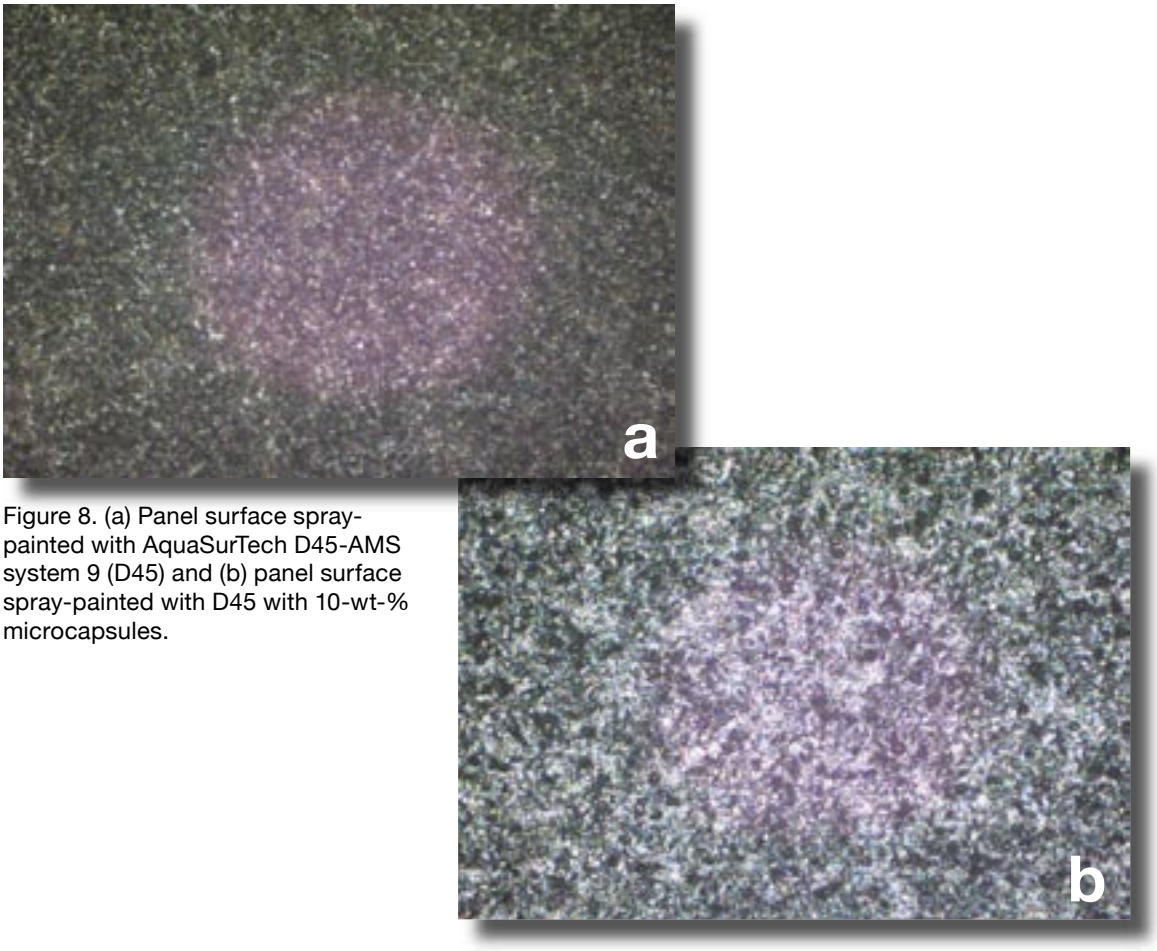

Figure 8. (a) Panel surface spray-painted with AquaSurTech D45-AMS system 9 (D45) and (b) panel surface spray-painted with D45 with 10-wt-% microcapsules.

The pH sensitivity of the microcapsules in dry paint (D45) was also tested. Figure 9 shows the vivid color changes observed when the microcapsules in the dry paint were exposed to basic pH conditions.

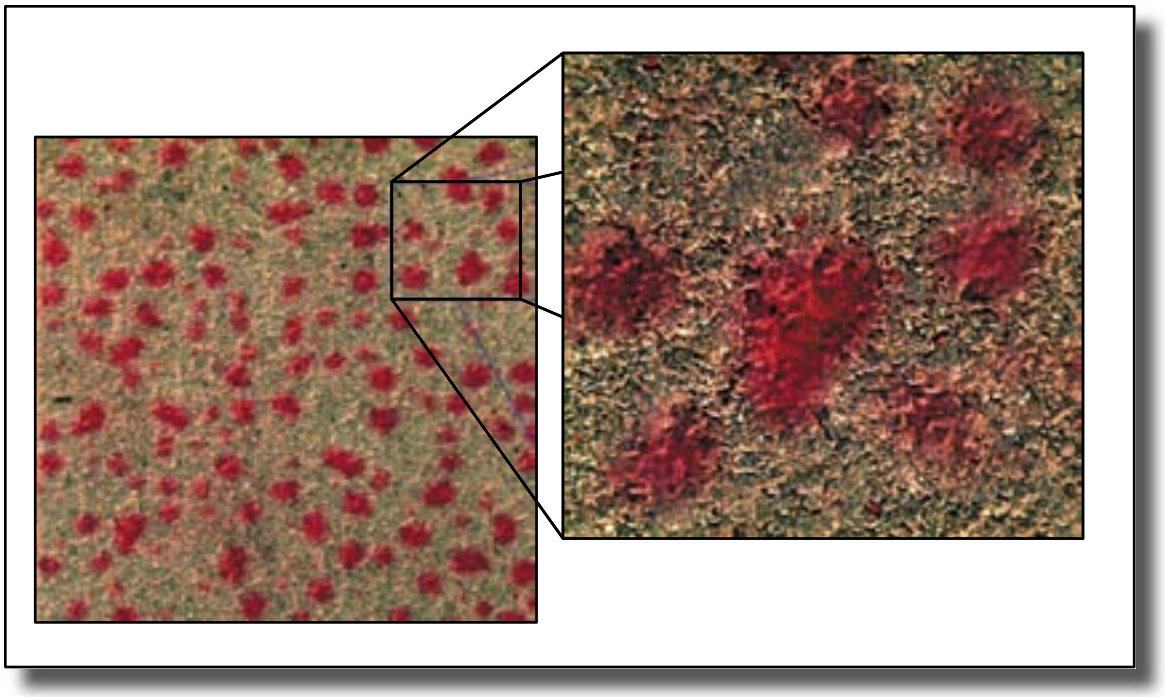

Figure 9. Color change observed when microcapsules in dry paint were exposed to basic pH conditions.

Sodium nitrite, $NaNO_2$, is a salt that can act as a corrosion inhibitor. The ability of the microcapsules to release a corrosion inhibitor was tested by encapsulating sodium nitrite and mixing the resulting microcapsules with the D45 paint. In preliminary electrochemical impedance spectroscopy (EIS) tests, on carbon steel panels coated with this paint showed greater corrosion resistance compared to a control sample (panels painted with D45 only). While this result was consistent with visual observations, further studies are still needed to confirm these results.

Conclusion

The results obtained to date indicate that this project has been successful in developing microcapsules that respond to the basic pH conditions present when localized corrosion occurs by delivering an indicator that changes color. The results also indicate that the microcapsules have the ability to deliver a corrosion inhibitor under the same conditions.

Future Work

Further work is needed to take this new technological development from the laboratory into practical applications. The ultimate goal of this project is to incorporate the corrosion-sensing and -inhibiting microcapsules into a paint system. This will require the complete characterization of different formulations. Techniques such as EIS and electrochemical noise method (ENM) can effectively examine the ability of the developed product to inhibit corrosion. Microscopy techniques such as atomic-force microscopy (AFM) and scanning electron microscopy (SEM), combined with an energy-dispersive spectrometer (EDS) can quantify the changes in surface morphology and local composition. Expanding on what EDS can provide, x-ray photoelectron spectroscopy (XPS) or Auger electron spectroscopy (AES) techniques can show the compositional and chemical changes on the coating surface, inside the coating, and at the interface of the coating and the metal substrate. These techniques can be employed to gain insight into the initiation and growth kinetics of localized corrosion and to design a better corrosion protection mechanism for the coating.

The microencapsulation of corrosion indicators in D-45 is a great start toward detecting localized corrosion and developing a way to suspend the microcapsules on top of the surface of the substrate. What can be added to this system are environmentally friendly corrosion inhibitors capable of stopping localized corrosion at an early stage. In this case, the indication of corrosion would not be necessary. However, when corrosion is not stopped or when it re-forms at the same spot, the indicator release would show the corrosion initiation and propagation. Because of the versatility of this microcapsule design, the possible applications of their smart-release capability are numerous and can be tailored depending on the need to be filled. Refining the technology will be an ongoing process, but the initial results prove that the microcapsule concept and its smart-release mechanism will provide a great opportunity for intelligent delivery in the fight against corrosion.

References

1. S. Coburn, "Atmospheric Corrosion," in *Metals Handbook*, 9th ed., Vol. 1, "Properties and Selection, Carbon Steels," American Society for Metals, Metals Park, Ohio, 1978, p. 720.

2. CC Technologies Laboratories, Inc. (Dublin, Ohio), "Corrosion Costs and Preventive Strategies in the United States: Supplement to Materials Performance," July 2002.

3. "Corrosion Testing," n.d., <http://www.corrosion-doctors.org/Localized/Introduction.htm> (August 22, 2006).

4. M. Xanthos, "Functional Additives as Sensors in Intelligent Polymer Coatings," *Smart Coating II, European Coatings Conference*, Berlin, Germany, June 2003.

5. Mike Agosta, "NJIT to Develop Smart Coatings for U.S. Army," Coatings World, March 2003, <http://www.coatingsworld.com/articles/2003/03/njit-to-develop-smart-coatings-for-us-army.php> (August 23, 2006).

6. A.A. Voevodin, T.A. Fitz, J.J. Hu, and J.S. Zabinski, "Nanocomposite tribological coatings with 'chameleon' surface adaptation," *J. Vac. Sci. Technol. A*, Vol. 20, Issue 4, July 2002, p. 1434.

7. R.R. Koepsel and A.J. Russell, "Directed Capture of Enzymes and Bacteria on Bioplastic Films," *Biomacromolecules*, Vol. 4, Issue 3, May 2003, pp. 850–855.

8. B. McKee, S. Dahl, and K. Shkarlet, "Smart coatings for in-situ monitoring of engine components," *Proc. SPIE 3674*, March 2, 1999, pp. 461–468.

9. J.R. Nicholls, N.J. Simms , W.Y. Chan, and H.E. Evans, "Smart overlay coatings — concept and practice," *Surface and Coatings Technology*, Vol. 149, Issues 2–3, January 15, 2002, pp. 236–244.

10. "Smart Coatings," *Corrosion-Club.com*, n.d. <http://www.corrosion-club.com/smart.htm>, (August 23, 2006).

11. J. Zhang and G.S. Frankel, "Corrosion-Sensing Behavior of an Acrylic-Based Coating System," *Corrosion*, Vol. 55, October 1999, pp. 957–967.

12. R.E. Johnson and V.S. Agarwala, "Fluorescence Based Chemical Sensors for Corrosion Detection," *Corrosion*, NACE International, New Orleans, Louisiana, 1997.

13. R.E. Johnson and V.S. Agarwala, "Using Fluorescent Compounds as Early Warning Detectors for Corrosion," *Materials Performance*, April 1994, pp. 25–29.

14. V.S. Agarwala, "Sensors for Hidden Corrosion Damage: Detection and Monitoring," Naval Air Warfare Center, Aircraft Division, Patuxent River, Maryland, November 1997, <http://smaplab.ri.uah.edu/lce/agarwara.pdf> (August 23, 2006).

15. G.S. Frankel et al., "Corrosion-Sensing Composition and Method of Use," U.S. Patent Application 20030068824, December 21, 1999.

16. A. Kumar and L.D. Stephenson, "Smart coatings," *23rd Army Science Conference*, Orlando, Florida, December 2002.

17. M. Kendig, "Past, Present, and Future 'Smart' Protective Coatings," *Conf. Advanced Research and Development of Coatings for Corrosion Protection: Offshore Oil and Gas Operation Facilities, Marine Pipeline and Ship Structures*, Biloxi, Mississippi, organized by Colorado School of Mines, April 14–16, 2004.

18. H.A. Katzman, G.M. Malouf, R. Bauer, and G. Stupian, *Appl. Surf. Sci.*, Vol. 2, 1979, p. 416.

19. M. Kendig, A.J. Davenport, and H.S. Isaacs, "The mechanism of corrosion inhibition by chromate conversion from x-ray absorption near edge spectroscopy (Xanes)," *Corros. Sci.*, Vol. 34, Issue 1, January 1993, pp. 41–49.

20. J. Zhao, G.S. Frankel, and R. McCreery, "Corrosion Protection of Untreated AA-2024-T3 in Chloride Solution by a Chromate Conversion Coating Monitored with Raman Spectroscopy," *J. Electrochem. Soc.*, Vol. 145, Issue 7, July 1998, pp. 2258–2264.

21. Lin Xia, Ejii Akiyama, Gerald Frankel, and Richard McCreery, "Storage and Release of Soluble Hexavalent Chromium from Chromate Conversion Coatings Equilibrium of CrVI Concentration," *J. Electrochem. Soc.*, Vol. 147, Issue 7, July 2000, pp. 2556–2562.

22. M.W. Kendig and R.G. Buchheit, "Past, Present and Future 'Smart' Protective Coatings," *Corrosion*, Vol. 59, No. 5, 2003, pp. 379–400.

23. G.S. Frankel, "Corrosion Science in the 21st Century," *J. Corros. Sci. and Engineering*, Vol. 6, paper C028, July 2003.

24. F.C. Jain, J.J. Rosato, K.S. Kalonia, and V.S. Agarwala, "Adhesives, Sealants, and Coatings for Space and Harsh Environments," *ACS Conference Proceedings*, Colorado, 1987.

25. F.C. Jain; J.J. Rosato; K.S. Kalonia; and V.S. Agarwala, *Corrosion*, Vol. 42, 1986, pp. 700.

26. N.N. Voevodin N.T. Grebasch, W.S. Soto, F.E. Arnold, and M.S. Donley, "Potentiodynamic evaluation of sol-gel coatings with inorganic inhibitors," *Surface and Coatings Technology*, Vol. 140, Issue 1, May 1, 2001, pp. 24–28.

27. Joseph H. Osborne, "Observations on chromate conversion coatings from a sol-gel perspective," *Progress in Organic Coatings*, Vol. 41, Issue 4, May 2001, pp. 280–286.

28. H. Yang and W. van Ooij, "Plasma Deposition of Polymeric Thin Films on Organic Corrosion-Inhibiting Paint Pigments: A Novel Method to Achieve Slow Release," *Plasmas and Polymers*, Vol. 8, No. 4, December 2003, pp. 297–323.

29. F. Mansfeld, C. Hsu, Z. Sun, D. Ornek, and T. Wood, "Ennoblement—A Common Phenomenon?" *Corrosion*, Vol. 58, No. 3, 2002, pp. 187–191.

30. Geraint Williams and H. Neil McMurray, "Annion-Exchange Inhibition of Filiform Corrosion on Organic Coated AA2024-T3 Aluminum Alloy by Hydrotalcite-Like Pigments," *Electrochemical and Solid State Letters*, Vol. 6, Issue 3, March 2003, pp. B9–B11.

31. B. Wessling, "Corrosion prevention with an organic metal (polyaniline): Surface ennobling, passivation, corrosion test results," *Materials and Corrosion*, Vol. 47, Issue 8, 1996, pp. 439–435.

32. Geoffrey M. Spinks, Anton J. Dominis, Gordon G. Wallace, and Dennis E. Tallman, "Electroactive conducting polymers for corrosion control," *J. Solid State Electrochemistry*, Vol. 6, No. 2, February 2002, pp. 85–100.

33. M. Kendig, M. Hon, and L. Warren, "'Smart' corrosion inhibiting coatings," *Progress in Organic Coatings*, Vol. 47, Issues 3–4, September 2003, pp. 183–189.

34. S. Cogan, M. Gilbert, G. Holleck, J. Ehrlich, and M. Jillson, "Galvanic Coupling of Doped Polyaniline and Aluminum Alloy 2024-T3," *J. Electrochem. Soc.*, Vol. 147, Issue 6, June 2000, pp. 2143–2147.

35. D.W. DeBerry, "Modification of the Electrochemical and Corrosion Behavior of Stainless Steels with an Electroactive Coating," *J. Electrochem. Soc.*, Vol. 132, Issue 5, May 1985, pp. 1022–1026.

36. E. Juanita Van Koppenhagen et al., "Base-triggered release microcapsules," U.S. Patent 6544,540. April 8, 2003.

37. F.J. Maile, T. Schauer, and C.D. Eisenbach, "Evaluation of corrosion and protection of coated metals with local ion concentration technique (LICT)," *Progress in Organic Coatings*, Vol. 38, Issue 2, May 2000, pp. 111–116.

Funding Authorized for FY 2005: $85K

Completion Date: September 2005

Model for Software Quality Diagnosis and Prognosis

Leader: Justin Beaver, NASA

External Partners/Collaborators: Guy Schiavone, Ph. D., and Joseph Berrios, Ph.D., University of Central Florida

Initiaion Year: FY 2005

Purpose

The purpose of this project is to develop a model that can produce a reliable diagnosis of the quality of a software product and an accurate prognosis of the quality of software that is under development. The model can be used to identify potential technical risks within a software development effort and will enable a project team to mitigate those risks earlier in the software life cycle, when they are least expensive to correct.

Background

The aim of any software project is to deliver the most useful and reliable product within the budget and schedule allotted, but the very nature of software development puts the project at risk of missing these parameters. Through statistical and machine learning methods, software quality models illuminate facets of the product and process that might otherwise escape notice and thereby increase the chances of project success.

Modeling software quality is inherently difficult given the complexities of any software development effort. The software life cycle covers a wide range of factors that can influence the quality of the delivered system. To accurately portray the quality of a software product, the model must represent all of those factors. Prior software quality models do not address all the influencing factors, are not universally applicable, and have data quality problems during validation. Much of the body of software quality research focuses on establishing empirical relationships to forecast software quality and ignores any logical or causal relationships that may exist. However, recent progress in software quality modeling, using complex adaptive systems such as Bayesian Belief Networks, has shown promise in accurately representing cause-effect relationships in software product development and providing models that are adaptable to a given development team and environment.

Approach

The software quality diagnosis/prognosis model to be developed assumes three underlying causal factors of quality in software: software problem complexity, software personnel skill, and software process maturity. These three factors will be modeled in all development life cycle phases and will provide a diagnosis/prognosis of software product quality. Figure 1 depicts the high-level structure of the proposed software quality model. The model takes as inputs measurements of development team skill, software process maturity, and software problem complexity over the entire software life cycle, and produces assessments and forecasts of software product quality.

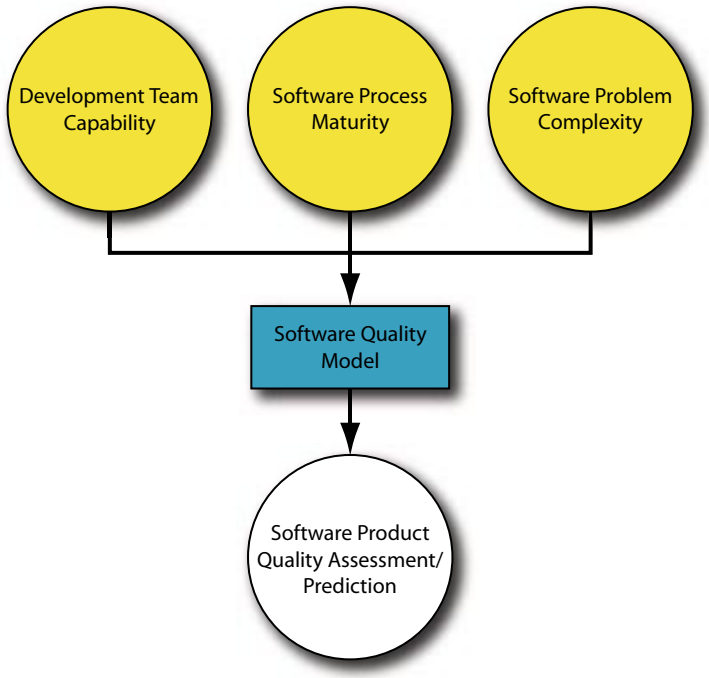

Figure 1. Software quality model inputs and outputs.

Modeling software quality requires a consistent way to quantify the three model inputs and the single model output shown in Figure 1. A measurement framework has been selected for each input and output, based on existing standards and/or widely accepted approaches to software engineering measurement. The assessment of development team skill is a consolidation of individual skill ratings derived from NASA's Competency Management System. Software process maturity is quantified using ISO/IEC 15504, "Software process assessment," as a basis for compliance with industry practices. Software problem complexity is represented differently for each life cycle phase, ranging from the volume of quality expectations of the software to the traditional software engineering design complexity measures. Finally, software product quality is expressed in the model in terms of the metrics defined in ISO/IEC 9126, "Software engineering — Product quality."

The Bayesian Belief Network (BBN) is the mathematical technique selected to model software quality in this research effort. A BBN is an adaptive system, meaning that its underlying algorithm allows for the adjustment of model output values based on prior data sets. A BBN is graphically represented as a collection of nodes that are connected by directed arcs. The nodes represent random variables within the model, with each node providing probabilities of outcomes based on a set of input values. The directed arcs represent causal relationships or dependencies between nodes. A BBN is capable of representing cause-and-effect relationships using both discrete and continuous variables, can adapt to prior data, and can infer unknown data elements based on a set of known data elements.

Figure 2 is a cause-effect diagram that represents the structure of the software quality model and details the internal relationships between measurements. Quality is affected by the correctness and completeness of the activities and artifacts at each phase of the development life cycle. Measures of correctness and completeness are driven by the development team's skill/experience level, the process maturity or infrastructure, and the problem complexity for each phase.

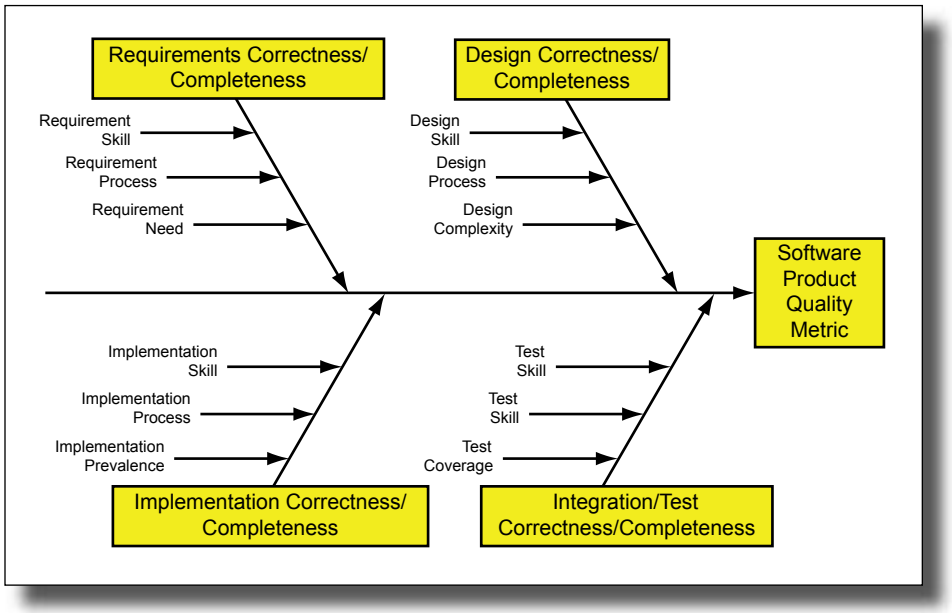

Figure 2. Software quality model structure.

Accomplishments

The software quality model was completed and implemented as a software application that acquired data from a file; implemented the BBN programmatically; forecasted software quality, using conditional probabilities calculated from prior data sets; and automated any validation of the forecasts. The sets of data used to train and validate this software quality model are from 28 small-scale software development projects. Each project was tracked for various software engineering metrics through the development life cycle.

The software quality model was validated as an accurate forecaster of software quality in three steps: determining the sufficiency of the sample sizes; validating the model's ability to diagnose software quality, using the Equality of Means statistical test; and evaluating the accuracy of the model's prognosis, using the Average Relative Error (ARE) criterion. The developed software quality model was validated as an accurate predictor of 16 software product quality metrics from ISO/IEC 9126.

Table 1 contains the results of calculating the ARE for each of the software quality indicator metrics that were found to be of sufficient sample size and have equivalent means between their modeled and actual values. The AREs for all of the metrics analyzed fell below the maximum threshold of 0.25. In most cases, the ARE was below 0.05, indicating that the model was extremely accurate in predicting these aspects of software quality.

Table 2. Software quality model validation results

ISO/IEC 9126 Quality Indicator Metrics	Average Relative Error (ARE)
Functional Adequacy	0.050
Functional Completeness	0.066
Functional Correctness	0.048
Access Auditability	0.036
Access Controllability	0.050
Data Encryption	0.025
I/O Utilization	0.025
Efficiency Compliance	0.033
Failure Avoidance	0.106
Incorrect Operation Avoidance	0.230
Restorability	0.036
Reliability Compliance	0.050
User Operation Cancelability	0.033
Operational Status Monitoring	0.038
Usability Compliance	0.036
Activity Recording	0.042

Abstracts

Beaver, J.M., and G.A. Schiavone, "A Life Cycle Software Quality Model" (submitted to *ACM Transactions on Software Engineering and Methodology* on October 13, 2005).

Beaver, J.M, and G.A. Schiavone, "The Effects of Development Team Skill on Software Product Quality" (submitted to *ACM SIGSOFT Software Engineering Notes* in March 2006).

Status of Investigation

This investigation was completed in FY 2005. However, further funding may be pursued to package this model for a broader application across NASA.

Funding Authorized for FY 2005:

CDDF, CTRGA Cost Center 76QUALDIAG – $10K

Actual or Expected Expenditures of FY 2005 Funding:

In-house procurements – $2K
In-house Contract – $0K
Outside Contracts/Grants – $0K

Completion Date: September 2005

Formulation of Specialty Polymeric Materials for Electrostatic Dissipation and Flame Retardancy

Leaders: Martha Williams, Ph.D., Trent Smith, Luke Roberson, Ph.D., LaNetra Clayton, Ph.D., and Jacqueline Quinn, Ph.D., NASA

Other In-House Members of the Team: Charles Buhler, Ph.D., and Barry Meneghelli, Ph.D., ASRC Aerospace Corp.

External Partners/Collaborators: Gordon Nelson, Ph.D., Florida Institute of Technology,
Julie Harmon, Ph.D., University of South Florida

Initiation Year: FY 2004

Purpose

This project addresses the formulation and use of advanced materials to meet system safety needs to minimize electrostatic charges, flammability, and radiation exposure for future spaceport technologies such as spaceport personnel protective systems, human/robotic exploration missions, and homeland security applications. The research includes enhanced polymer feasibility studies on the addition of metallic nanoscale particles into polymers for enhanced electrostatic dissipative properties and for possible radiation shielding applications. Unique materials that have both electrostatic dissipation and flammability properties will be specifically formulated and engineered. Unique formulations will include the investigation of new flame-retardant additives, inorganic nanomaterials, conductive polymers, metallic nanoparticles, and other constituent materials.

Phase II of the project built on the success of Phase I, which included the NASA New Technology Report (NTR) filing/patent-pending filing of "New Approach for Achieving Fire Retardancy and Improving Physical Properties in a Compatible Polymer Matrix," where a novel material has been formulated for flame retardancy and increased thermal performance. Other prototype materials using nanoparticles indicate electrostatic dissipation properties. We continued to develop and improve formulations, raising the technology readiness levels (TRLs) of polymer blends and nanocomposites using a flame-retardant additive, inorganic nanomaterials, conductive polymers, metallic nanoparticles, and other constituent materials with defined performance properties such as low-temperature applications.

In Phase II, new matrix-nanocomposite materials will be manufactured, characterized, and examined to improve thermal conductivity and mechanical properties of the specialty polymeric materials. Additives will be incorporated at different concentrations into several polymer matrices to construct polymer-nanocomposite or "super" materials that will possess a combination of the aforementioned highly desired properties. Unique and multifunctional composite formulations will broaden the selection of materials available for future lunar and Mars space exploration activities.

Background

High-performance plastics do not by themselves dissipate electrostatic charge and can easily burn. Combining unique attributes, such as electrostatic dissipation, thermal conductivity, mechanical strength, and flame-retardancy, inherent in the chemistry of a polymer is a significant chemical challenge. These properties must be addressed to reduce current limitations of coatings on protective equipment (ground-based and on-orbit protective gear) where uncertain risks exist, such as loss of capabilities with nominal wear. Currently, protective gear is designed to be flame-retardant and is sprayed with an electrostatic-dissipation material. This material wears off with time, subjecting the user to unforeseen dangers. This project will investigate and develop formulations of polymer blends and nanocomposites, using inorganic nanomaterials, metallic nanoparticles, and other constituent materials, into novel uncoated specialty polymeric materials for use by ground-based and on-orbit crews and for future exploration.

The Phase I project performed proof-of-concept studies, using additives and polymeric formulations that provide a chemical environment suitable for flame retardancy and electrostatic dissipation. Formulations will also address other enhanced properties, such as increased mechanical strength, thermal conductivity, and potential inhibition of radiation. Baseline material characterization data for mechanical and thermal properties was collected for prototype polymeric formulations. Flammability properties were studied using limited-oxygen index (LOI) analyses. Formulation options were refined and optimized in Phase II. The following characteristics were targeted:

- LOI: flame retardancy,
- peak heat release rate: less than 500 kW/m^2,
- surface resistivity: 106 to 1,012 Ω per square or a short corona charge decay time (seconds),
- radiation shielding properties, and
- low-temperature properties, including impact brittleness testing and thermal conductivity testing.

In Phase I, feasibility studies were performed specifically on target inorganic nanomaterials formulations that showed promising potential during evaluation. Other formulations with inert nanoscale materials, such as nanoscale metals (Figure 1), were tested to evaluate electrostatic dissipation, radiation inhibition, reduced flammability, strength, and flexibility. Further details on technical approach are not being reported here because of intellectual-property considerations. TRLs are to be raised in all material formulations.

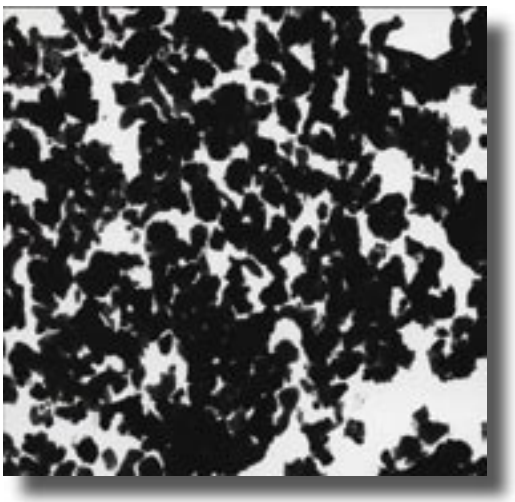

Figure 1. Micrograph of nanoiron used in formulations.

The following are the primary equipment and technologies used for characterization and evaluation:

- tensile-strength Instron tester,
- mechanical and thermal analysis instrumentation,
- LOI analyzer,
- x-ray diffraction and imaging,
- optical microscopy,
- Fourier Transform Infrared Spectroscopy (FTIR) analyses,
- cone calorimeter,
- Netzsch thermal diffusivity/conductivity analysis, and
- impact brittleness testing.

Approach

In Phase I, new specialty material formulations were fabricated using various loading levels of a flame-retardant additive and different polymer matrices. LOI results of low-loading formulation showed a dramatic change in combustion mechanics and burn time with respect to the unmodified matrix, with enhanced flame retardancy and thermal properties. Lifetime estimation was significantly increased in the new flame-retardant material over that of the unmodified material. At the same low loading levels, formulations showed increased charge dissipation. Higher loading levels result in enhanced fire properties over those observed in the lower loading levels. Preliminary analyses of peak heat release rates of one specialty material performed with a cone calorimeter (Figure 2) indicated significant decreases over those of the unmodified polymer. A patent was filed on new flame retardancy technology in 2004. In Phase II, other composites with industry-preferred matrices were formulated, with increased loading (over that employed in Phase I); flammability tests indicated increased fire performance in UL-94 evaluation. In cone calorimetry analyses, significant decreases (up to 60 percent, less than 260 kW/m^2, with defined loading) in peak heat release rates (PHRRs) were observed. Figures 3 through 5 depict cone flammability testing of unmodified material compared to 10 percent and 20 percent loading of flame-retardant additive, where significant decrease in size of fire with the flame-retardant additive are shown. A Space Act Agreement was signed with an industry partner. The technology has been scaled up, and the additive is being evaluated in industry for possible technology transfer and commercialization.

Figure 2. Refurbished cone calorimeter for studying flammability properties.

Figure 3. Cone calorimetry flammability test of unmodified matrix.

Figure 4. Cone calorimetry flammability test of 10 percent additive loading. Shown is an obvious visual decrease in size of fire compared to unmodified matrix.

Figure 5. Cone calorimetry flammability test of 20 percent additive loading. Shown is a visual decrease in size of fire compared to 10 percent, and a significant decrease compared to unmodified matrix.

In Phase I, feasibility studies were carried out on a nanoiron-organic formulation using two different polymeric matrices. The feasibility studies on an inorganic-organic nanoiron composite formulation demonstrated desirable and enhanced thermal-mechanical properties when compared to the unmodified material, with the inorganic component contributing to changes in electrostatic, thermal, and physical properties (Figure 1). These nanoiron composites should have shown interesting shielding properties with respect to high-energy photons (ionizing radiation—x-rays and gamma rays). This assumption is based on other systems reported in the literature. In addition, preliminary data did indicate that the materials possessed electrostatic dissipative properties and absorbed x-ray radiation. These materials are being developed with the goal of attenuating ionizing radiation for NASA use with a lunar spaceport and interplanetary missions.

In the middle of Phase II, collaboration with a university partner was initiated in the formulation of the inorganic nanoparticles-organic formulations to meet 2005 milestones (return to flight demanded high workforce commitment). The composites were made with nanomaterials barium titanate and bismuth oxide (high atomic numbers, high-Z nanomaterials). These nanomaterials have high dielectric constants and also have piezoelectric properties. The composites should also have exceptional dielectric properties, serve as radiation attenuators, and have optimum charge dissipation. These composites can also have applications for components in actuators and sensors. At higher loading, these composites can be used as gamma radiation shields. Optimization of the nanomaterial's dispersion is key to a composite's performance.

Prototype composites were formulated with loadings ranging from 0 weight-percent to 20 weight-percent (Figure 6) and exposed to a gamma radiation source. The extent of degradation was characterized via thermal analysis. Preliminary results show that a possible filler threshold is reached at 5 weight-percent; however, various dispersion techniques, as well as the incorporation of possible coupling agents and other additives, must still be explored to achieve favorable interaction between the nanoparticles and the polymer matrix. Proper shielding experiments that chronicle various polymer matrices, effective thicknesses, and filling loads should still be explored. Formulation with a nanomaterial additive for synergistic and enhanced properties is presently being carried out under contract. Characterization of the composites' properties is in progress and should provide a template design for tunable composites depending on filler load and polymer matrix. It is expected that after complete characterization of the new formulations, these composites will show certain enhanced properties, such as those discussed above, and will be able to serve as alternatives to metals in certain applications.

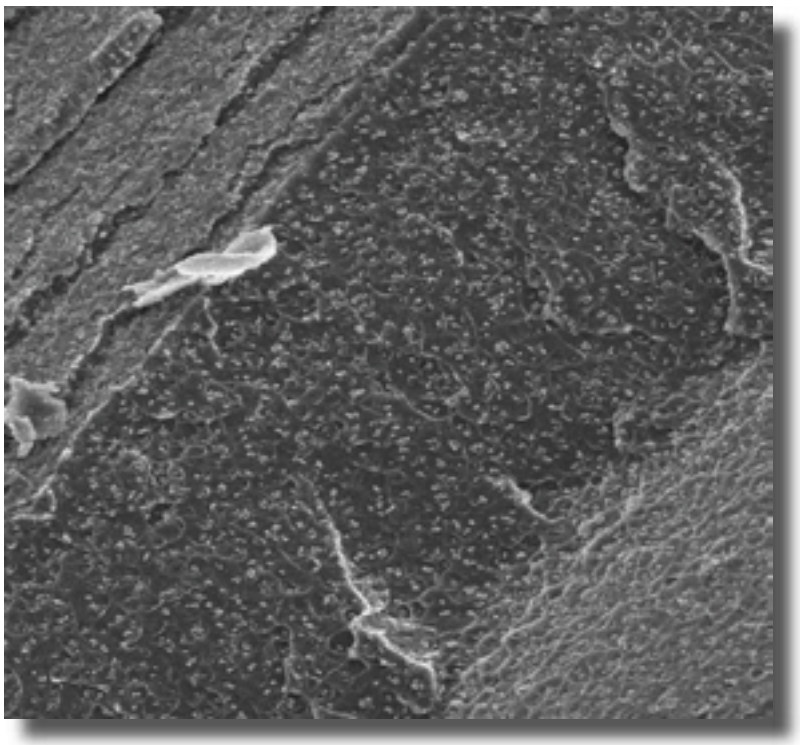

Figure 6. Polymer/nanoparticle composite at 20-weight-percent loading.

Novel inorganic/organic composite systems were formulated with different loading levels and different matrices and were characterized to examine the effect of additives on the system. In Phase I preliminary evaluations at lower temperatures, specific heat data indicated that the composite is a better insulator than the unmodified polymer matrix, with as little as 1 percent additive. In the latest 5-weight-percent loading composite formulations, a 40-percent increase in thermal performance is measured when compared to the natural matrix. Other high-engineered polymer matrices are being studied in the 2006 project.

Publications

Williams, M.K., and T.M. Smith, "A New Approach For Achieving Fire Retardancy While Retaining Physical Properties In A Compatible Polymer Matrix," NASA New Technology Report KSC-12697 (submitted April 15, 2004).

Williams, M.K., and T.M. Smith, "A New Organic/Inorganic Polymeric Materials," NASA New Technology Report KSC-5019137 (submitted August 18, 2005).

Smith, Jr., J.G, T. Smith, M. Williams, and W. Mendell, "Potential Polymeric Sphere Construction Materials for a Spacecraft Electrostatic Shield" (in press).

Patent Applications

Williams, M.K., and T.M. Smith, "A New Approach For Achieving Fire Retardancy While Retaining Physical Properties In A Compatible Polymer Matrix," Nonprovisional Patent Application Serial No. 10/962,827 (filed October 6, 2004).

Status of Investigation

A patent was filed on the New Approach to Fire Retardancy in 2004, and a Space Act Agreement was signed in 2005 with an industry partner to scale up the technology and to obtain an industry evaluation of viability of the technology application. The scale-up of the technology was successfully completed, and the additive is being evaluated in industry for possible technology transfer and commercialization.

FY 2004 Innovative Partnerships Program funding (UPN 251) of $19K was used to purchase a new carbon monoxide/carbon dioxide (CO/CO_2) analyzer for the cone calorimeter to study CO/CO_2 production upon complete combustion. CO/CO_2 ratios of small flammability tests are effective in modeling full-scale fire toxicity hazards. The analyzer was installed in 2005 and is presently in use with cone calorimetry flammability testing.

Impact brittleness testing has been initiated with the brittleness tester that was purchased in Phase I (testing was delayed because of return-to-flight commitments). Impact brittleness parameters for inorganic-organic polymer composites for low-temperature applications will be evaluated under a separate project in 2006.

Planned Future Work

Further development was required in FY 2006 to raise the TRL of the inorganic-organic composite systems for low-temperature applications with other enhanced properties.

In raising the TRLs of these novel inorganic-organic composites, the activity in FY 2006 with Center Director's Discretionary Funds will focus on developing the composite systems further and characterizing performance parameters. Low-temperature performance properties will be optimized. Impact brittleness testing has begun, which will examine mechanical properties of the composites at low temperatures. This is required for the optimization of this performance parameter. An increase in flexibility and fire resistance (depending on the matrix polymer) will be evaluated. Fire performance will be studied using LOI and cone calorimetry. Netzsch thermal conductivity testing will be used in evaluating thermal performance properties.

Unique additive combinations will be incorporated into these matrices (including various loading levels) to develop multifunctional or "super" materials. Characterization techniques such as elemental analysis (atomic-absorption spectroscopy and inductively coupled plasma-mass spectroscopy) are slated for confirming exact loading concentrations and interactions between individual additives and between the additive and the matrix. Extensive development, formulation, and characterization will be required to design and analyze these composites. The formulation of a multicomponent polymer system that can address low temperatures, flame retardancy, mechanical strength, flexibility, and charge dissipation will create "super" materials that can be employed in a wide range of applications.

A $1.197M Human and Robotics Technology (H&RT) Intramural proposal titled "Spacecraft Electrostatic Shielding" was awarded to KSC by the NASA Exploration Systems Mission Directorate (ESMD) in August 2004 ($200K over 2 years). The project will determine the feasibility of an electrostatic radiation shield for future interplanetary vehicles. The shielding design will incorporate positively and negatively charged spheres made from materials already available or from ones whose properties can be enhanced for this application. Although the present polymer development at KSC in radiation shielding is specific to x-ray and gamma radiation, polymer and materials development expertise is being used for this shielding application. The Phase I objectives are to

- study and evaluate material performance requirements;
- address several approaches in the selection of the sphere material, such as film versus a weave (conductivity, surface tensions, and leakage currents of the polymeric materials are primary concerns); and
- recommend sphere material(s) composite design.

The first internal critical review was completed in March 2005. Selection of materials, required performance parameters, and design are being reevaluated based on probable redesign of the shape of the spheres.

Phase II of this project was not proposed/awarded because of the restructuring of Exploration in lieu of Crew Exploration Vehicle (CEV) commitments. A report titled "Potential Polymeric Sphere Construction Materials for a Spacecraft Electrostatic Shield" by J.G. Smith, Jr., T. Smith, M. Williams, and W. Mendell is being published in 2006.

A $12M H&RT Extramural proposal titled "Next-Generation Wiring Materials" was awarded to ASRC Aerospace by NASA ESMD in November 2004. In support of this project, KSC will address use of polymeric conductors to meet the needs of future spaceport technologies, utilizing $1.7M over 4 years. For long-term exploration, the present wire insulation technology must be significantly enhanced or completely replaced with a more proactive wiring system. The next generations of conductor materials need to be lightweight, small in volume, tough, durable, and corrosion-resistant. These materials must also possess the thermal and radiation tolerance needed for safe and reliable space exploration systems and habitats. Conducting polymeric materials that are lightweight, easily processed, and flexible are an attractive alternative for metallic materials. In addition, the conductivity of these materials can be tuned or enhanced by several methods while including other required performance parameters.

The primary Phase I objectives for the conductive polymers research are to identify and evaluate state-of-the-art and emerging technologies and gaps in those technologies for next-generation wiring applications. To fill these gaps, KSC will develop, in parallel, synthetic and technological approaches to increase conductivity in high-performance polymeric and carbon nanotube materials, making them approach that of copper. KSC will comprehensively evaluate state-of-the-art and emerging conductive polymer technologies, with Crosslink Polymer Research Company consulting. Crosslink is a technology development company focused on inherently conductive polymer research with expertise in engineering smart materials for applications in diverse markets. A range of technologies for defined applications will be evaluated, and in Phases I and II, the most promising technologies will be recommended. Under Phase II, the best approaches will be identified, and samples will be evaluated to refine the technology and optimize such key properties as conductivity, strength, and thermal stability. In years 3 and 4, the research will focus on conductance degradation and reliability in space radiation.

Phase II of this project was not proposed/awarded because of the restructuring of Exploration in lieu of NASA's CEV commitments.

In 2006, new activities to develop lightweight and smart materials will address smart materials for wiring and detection systems, with earlier deliverables (some components of higher TRLs) that can meet CEV's technology requirements.

Aggregate Amount of Funding Authorized in FY 2003 and Earlier Years: $0K

Funding Authorized for FY 2004: $125.5K

CDDF, CTRG&A Cost Center 76FORMPOLY – $88.8K
CDDF, CTRG&A Cost Center 76CDDFSVE – $3.7K
CTC, CTRG&A Cost Center 76CTCDDF – $14K
Innovative Partnership Program, UPN 251 – $19K

Actual or Expected Expenditures of FY 2004 Funding:

In-house small-item credit card purchases – $6.6K
In-house procurements:
Low-temperature brittleness tester – $14K
Pycnometer closed-cell/open-cell content analyzer – $8.6K
Nova 2200E surface area analyzer – $17.2K
Refurbished cone calorimeter for flammability testing – $41.8K
CO/CO_2 gas analyzer – $19K
In-house contract with ASRC Aerospace Corp. – $8.6K
Consultant contract with Gordon Nelson – $6K
NASA Travel – $3.7K

Expected Completion Date: The CDDF portion of Phase I and Phase II projects were completed in September 2005. A university was under contract for collaborative nanocomposites development until May 2006. New CDDF activity in Composites for Low-Temperature Applications was initiated in 2006.

Electrostatic Method of Surface Charge Measurement

Leader: Ellen Arens, NASA

Other In-House Members of the Team: Carlos Calle, Ph.D., NASA
Andrew Nowicki and Mindy Ritz, ASRC Aerospace Corp.

Initiation Year: FY 2004

Purpose

The project objective is to design and develop a lab-based instrument that uses the electro-optic Pockels effect to make static electric fields visible. When completed, this system will be used to monitor charge accumulation and decay on the surfaces of materials. This instrument will help determine the suitability of materials used in environments where an electrostatic discharge created by accumulated charge could pose a threat to personnel or equipment.

Background

Current methods of charge measurement using a Faraday cup or electrometers either are impractical for field measurements or do not give a true value of charge distributed over a surface. With the Faraday cup, the net amount of charge developed on a surface can be measured, but the surface charge density on the material cannot be determined. Also, the material to be measured must fit within the cup, which makes it impractical for determining the charge on the surfaces of large objects. Furthermore, only a single average value is reported to describe the charge accumulation on the material. Using electrometers to determine the amount of charge accumulated on a surface gives only an average reading of the electric field over an area, which can be greatly affected by any surrounding grounded or metallic materials. This method also gives only a single value to describe the electric-field characteristics of the materials.

The development and distribution of electrostatic charge on materials is a serious safety concern. Electrostatic charge can develop on a material's surface in a variety of ways, the most common of which is rubbing against other surfaces. The potential of an electrostatic spark poses a significant risk not only to sensitive electronic instrumentation, but also to personnel working where a spark could ignite fuels or pyrotechnics. For these reasons, Kennedy Space Center has been actively involved in developing tests to determine the safety of a variety of materials under different environmental and charging conditions. The development of an electro-optic system that provides a two-dimensional visual indication of charge distribution will be a significant advantage in determining a material's characteristics and safety.

Approach

An electro-optic method to visually indicate electrostatic charge developed on insulator surfaces will be investigated. Certain birefringent crystals undergo an electro-optic effect known as the Pockels effect—birefringence produced in an optical medium by a slowly varying electric field, in which the birefringence is proportional to the electric field. In these crystals, the phase of light changes as a function of the electric field across the crystal. By grounding one side of the crystal surface and bringing a charged surface near or in contact with the other crystal surface, the electric field across the crystal is modified. This in turn changes the phase of the light traveling through the crystal. If the light is polarized in a known direction before it travels through the crystal, then the polarization of the light will have shifted after exiting the crystal. The intensity of light output from the system as it passes back through a linear polarizer will depend on the electric-field strength applied. Therefore, the magnitude of the electric field across the crystal can be determined by measuring the intensity of the light after it passes through the crossed linear polarizer. This system will determine how charge is distributed over a surface and will identify both positive and negative charge.

Accomplishments

The initial layout and configuration of the optical components and image acquisition system was completed. A three-axis stage was included in the system to move the test materials to areas where they would be charged (triboelectrically through rubbing) and then move them in front of the electro-optic sensor for measurement. A schematic of the final setup is shown in Figure 1. Since the crystals in the system were only 25 mm in diameter, the stages were used to incrementally move the material in front of the sensor in a grid fashion so a larger surface area could be mapped (typical area measured was 15 cm × 15 cm). This system, including image acquisition and motion control, was fully automated in a LabVIEW program.

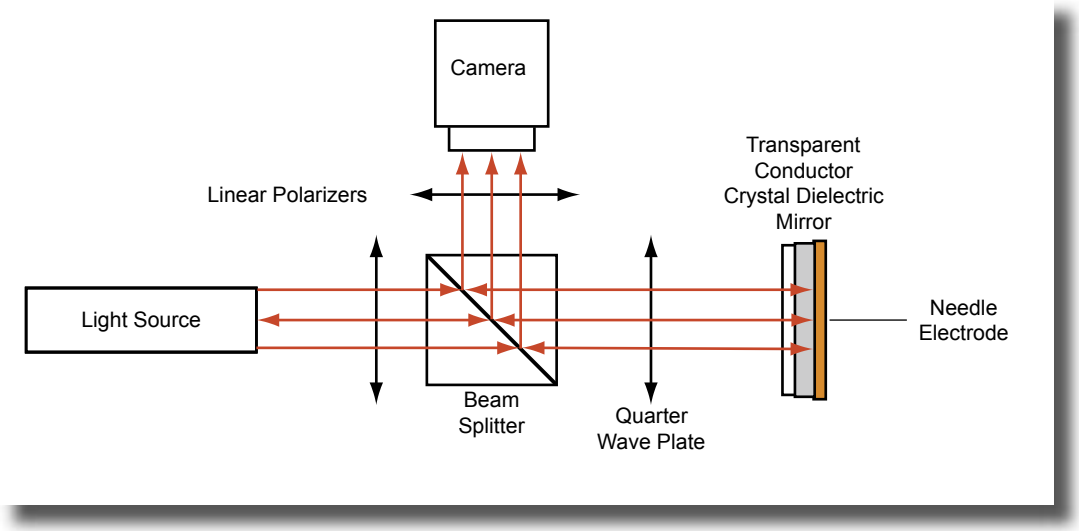

Figure 1. Electro-optic system design schematic.

Initial measurements made with BGO ($Bi_{12}GeO_{20}$) crystals demonstrated a significant transmittance change with increasing electric field across the crystal. A needle electrode was used to apply known voltages for system calibration. The intensity shifts of the images were correlated to the expected transmittance for the applied electric-field intensities.

We found that interference patterns in the images were caused by reflections of the image from the front and back surfaces of the crystals through the system. An image-processing algorithm was developed to reduce the interference patterns in the acquired images. To reduce the interference caused by surface reflections and the flexing of the crystal itself, we attempted to mount the crystal on a rigid glass substrate. Though the interference was reduced using this method, it was not eliminated. The manufacturing company is investigating the reduction of interference achieved by directly depositing the crystals on the substrate.

Status of Investigation

The system responded well when a voltage was applied to an electrode. An example of the intensity response of the system is shown in Figures 2 and 3. The response is sinusoidal, as expected, and the electric-field intensity created by to the applied voltage corresponds well with calculated electric-field intensities for the electrode configurations that were used.

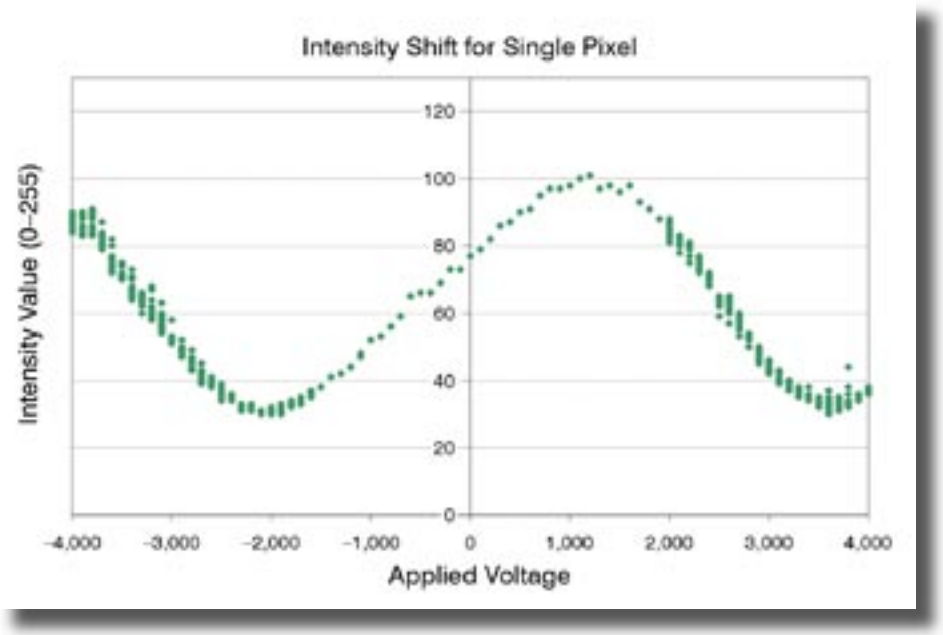

Figure 2. Intensity shift of the output light as the voltage applied to a needle electrode is incremented through a range from –4,000 V to +4,000 V.

Figure 3. The response of the crystal as the voltage applied to a needle electrode is increased from –1,000 V to +1,000 V. Each slice in the image shows the same section of the crystal, with the needle electrode located in the center of the image.

A problem with using this system at atmospheric pressure rather than in vacuum is that the breakdown voltage is easily met or exceeded at the small distances that we are using (1 mm or less). A smaller electric field would produce the same phase shift if the crystal thickness were increased so that the light had a longer travel time within the bifringent material; however, increasing the crystal thickness reduces the resolution of the system.

Planned Future Work

Though this system has visually indicated electric fields produced by various electrodes with applied voltages between –1,000 V and +1,000 V (corresponding to electric fields up to 1×10^6 V/m), the charge density developed on insulators has not been high enough to induce a measurable intensity shift. This concept shows promise for use in vacuum systems where the breakdown voltage is significantly higher. Applications in vacuum warrant more investigation. We are pursuing collaboration with the crystal manufacturer to develop applications to minimize the distortions when crystals are used in a modulating system operating as a light valve.

Funding Authorized for FY 2004: $111K

CDDF, CTRGA Cost Center 76ELECMEAS – $92K
CDDF, CTRGA Cost Center 76CDDFRSVE – $1K
Core Technical Capability, CTRGA Cost Center 76C4CTCDDF – $18K

Funding Authorized for FY 2005: $40K

Actual or Expected Expenditures of FY 2004 Funding:

In-house contract with ASRC Aerospace Corp. – $110K
NASA Travel – $1K

Completion Date: October 2005

VOC Filter Cartridge for Biological Experiments in Space

Leaders: John Sager, Ph.D., NASA
Oscar Monje, Ph.D., Dynamac Corp.

Other In-House Members of the Team:
Jeffrey Richards and Ignacio Eraso, Dynamac Corp.
Timothy Griffin, Ph.D., NASA

External Partners/Collaborators:
Peter Palmer, Ph.D., San Francisco State University
Gary Stutte, PhD., Dynamac Corp.
Gus Koerner, NASA/ALS Education Coordinator

Initiation Year: FY 2004

Purpose

Biological experiments in space are potential sources of volatile organic compounds (VOCs), which can add to the Trace Contaminant Control System of the International Space Station (ISS). Currently, only sporadic sampling of Space Transportation System (STS)/ISS cabin air is available; and gas sampling schemes occupy large volumes and are susceptible to leaks during stowage. The ability to filter, identify, and quantify VOCs flowing into or emanating from plant flight experiments will augment the science capabilities for research payloads and provide data for developing supplemental food production systems that use plants. The project objective is to develop a VOC filter cartridge that is passive (multiple passes over absorbent), is able to reversibly bind the VOCs after long-term storage, permits identification and quantification of VOCs, and meets flight safety guidelines.

Background

VOCs in Spacecraft

The accumulation of nonmethane VOCs in spacecraft cabin air can contribute to poor air quality and threaten the health of the crew during long space missions. Furthermore, removing these VOCs increases the load on the air purification/revitalization systems used to control CO_2 and water vapor in the crew cabin. To reduce health risks to the crew of the Crew Exploration Vehicle (CEV), the Environmental Control and Life Support Air Revitalization Element requires low-mass, low-power, and low-volume technologies that employ regenerable adsorption media and improved chemisorbents for use in vacuum swing and temperature swing regeneration systems.

Project Overview

The project was initially funded to develop a VOC filter for use in plant-based biological payloads to be deployed aboard spacecraft. In these systems, the main VOC of interest is ethylene, a plant hormone, because of its action on the development of plants. The approach was to (1) characterize the chemical specificity of five commercial off-the-shelf (COTS), thermally desorbing compounds to eight VOCs typically found in ISS cabin air, (2) determine the VOC loads (e.g., VOC production rates) expected in typical biological payloads, (3) size a regenerable filter to maintain the VOC concentrations in the payload below desirable levels (e.g., analogous to spacecraft maximum allowable concentration [SMAC] levels), and (4) demonstrate the efficacy of this reusable filter in a long-term test. Although this methodology was implemented using plant-produced VOCs as the source of trace contaminants (namely ethylene), the approach is valid for the development of regenerable trace contaminant control filters based on COTS materials for the CEV.

Plant-Based Payloads

Spacecraft air quality affects the quality of the science that can be carried out in plant-based payloads aboard spacecraft. For example, the SMAC for ethylene is 294 ppm, but plants respond to concentrations of ethylene as low as 25 ppb. These concerns are important to NASA's long-term goal of exploration whereby humans and biological systems share an air supply. Although plant-based systems will not be required until after 2018, the most probable plant chamber configuration for bioregenerative life support systems is a vegetable production unit (VPU) deployed in microgravity aboard the ISS [1], used in a lunar outpost or in transit to Mars. Such a food production system would supplement traditional packaged food with fresh salad crops [2]. The design requirements for such a unit have not been written yet and several candidate technologies exist for use in its design. The simplest design for such a chamber consists of a root tray, a light bank, and expandable Mylar walls (e.g., Vegetable Production System [VEGGIE] and Biomass Production System for Education [BPSe] chambers, designed by Orbitec in Madison, Wisconsin). These low-mass chambers save power because chamber air temperature and relative humidity are not controlled and they use cabin air as a source of CO_2. However, plants growing in these chambers are exposed to trace contaminants found in cabin air, among them ethylene, which can significantly reduce food production at levels above 50 ppb [3].

Ethylene and other VOCs are commonly found in spacecraft [4]. Ethylene in spacecraft is off-gassed from plastic materials, generated from decaying fruits in garbage bags, or produced by plants themselves during their development [5, 6]. Plants produce other VOCs (such as isoprene and carbon disulfide) that can also have biogenic activities [7]. The confined environment of spacecraft allows these VOCs to accumulate, and if unchecked, they can affect plant metabolism. Table 1 lists VOCs found in ISS cabin air [8].

Table 1. Concentrations of common VOCs in ISS cabin air.

VOCs in ISS Cabin Air[a]	Concentration (ppb)
Ethylene	50
Methanol	330
Ethanol	1,670
Dichloromethane	45
Acetaldehyde	120
Acetone	82
Xylene	11
Freon 12	26,000

[a]Methane not included.

High ethylene concentrations (0.6 to 1.0 ppm) aboard the Mir orbital space station caused the production of sterile (seedless) wheat heads during long-term experiments conducted in the Svet greenhouse [9]. This finding has prompted experiments to determine the sensitivity of staple crops (wheat and rice [10]) and salad crops (radish [11]) to ethylene exposures. Typical symptoms of ethylene exposure include stem thickening, reduced height, increased specific leaf area, reduced leaf area, and leaf epinasty [12, 13].

Space-flight-rated plant growth chambers have used either passive or active catalytic scrubbers to maintain acceptable levels of nonmethane VOCs. However, passive systems require large volumes of consumables, active systems consume large amounts of power, and the performance of both is degraded in high-humidity environments [14]. Furthermore, frequent monitoring of air quality in plant chambers aboard spacecraft with canisters or solid adsorbents is limited by volume and mass constraints.

Approach

The development of the VOC filter cartridge has involved three tasks spanning 2 years. The first task is filter media characterization. A mixed-bed, multifunction absorbent is selected, and the filter size and chemical specificity required to meet scrubbing limits for plant payloads is determined. The second task of filter cartridge design involves sizing the filter cartridge to control and monitor VOCs in plant experiments (low-mass plant growth chambers—BPSe and VEGGIE). The third task is efficacy testing to determine VOC filter performance in ground-based and flight plant experiments (e.g., BPSe and Radish Assimilation in Spaceflight Testbed Atmosphere [RASTA] flight experiment).

Adsorbent-Media Characterization Studies

In FY 2004, the project characterized several adsorbents for the purpose of designing a mixed-bed, adsorbent filter to meet the scrubbing requirements of biological payloads. Five thermally desorbing compounds were evaluated for their chemical specificity for filtering VOCs found in ISS cabin air (Table 1). The characterization tests used a benchtop system (Figure 1) to pass several liters of a 10× ISS cabin air mixture at 40 mL/min over 150 to 200 mg of adsorbent media. For each adsorbent, prefilter and postfilter concentrations were analyzed using a gas chromatograph (GC) (Figure 2). A thermal desorption injection system for an existing GC/mass spectrometer (MS) and a thermal desorption tube conditioning oven were purchased and installed (Figure 3). This methodology exposes each adsorbent to a complex mixture of VOCs, thereby simulating the performance of each adsorbent in ISS cabin air. The filtering capacity for each VOC measured in this fashion would probably be less than if the adsorbents were exposed to each VOC individually. For each VOC in the ISS gas mixture, a breakthrough curve plotting the postfilter concentration (Y) as a fraction of the prefilter concentration of the specific VOC (Y_O) versus elution time was prepared (i.e., CarboSieve SIII [Figure 4]).

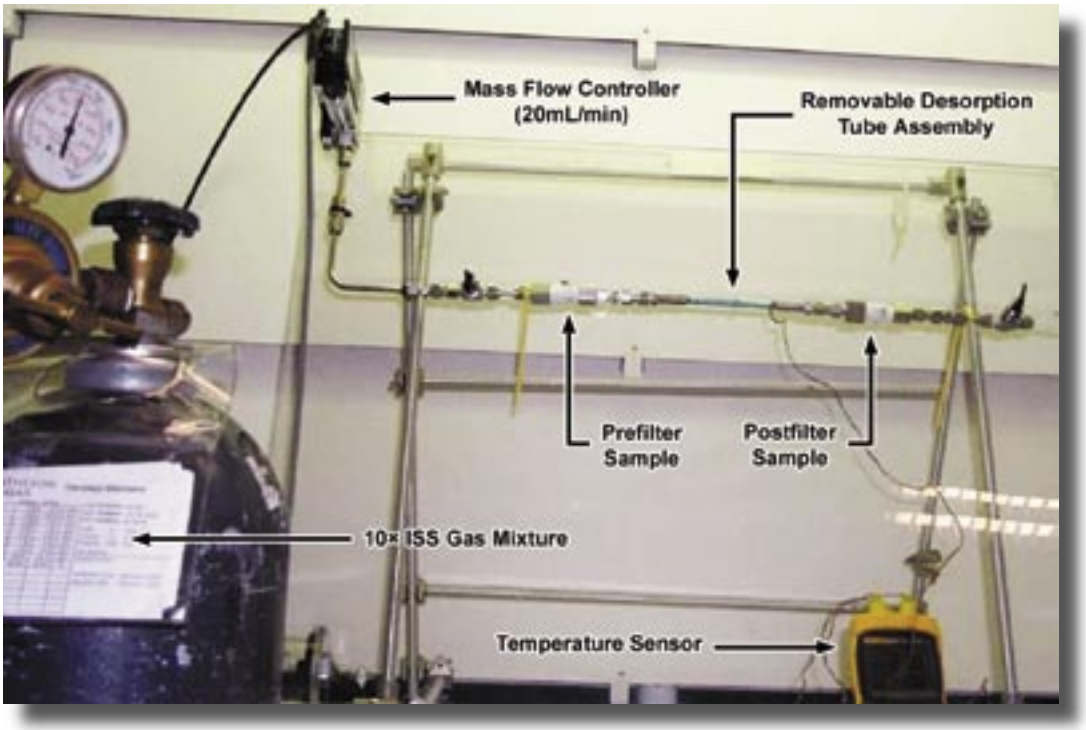

Figure 1. Benchhtop system developed for measuring the filtering characteristics of thermally desorbent media.

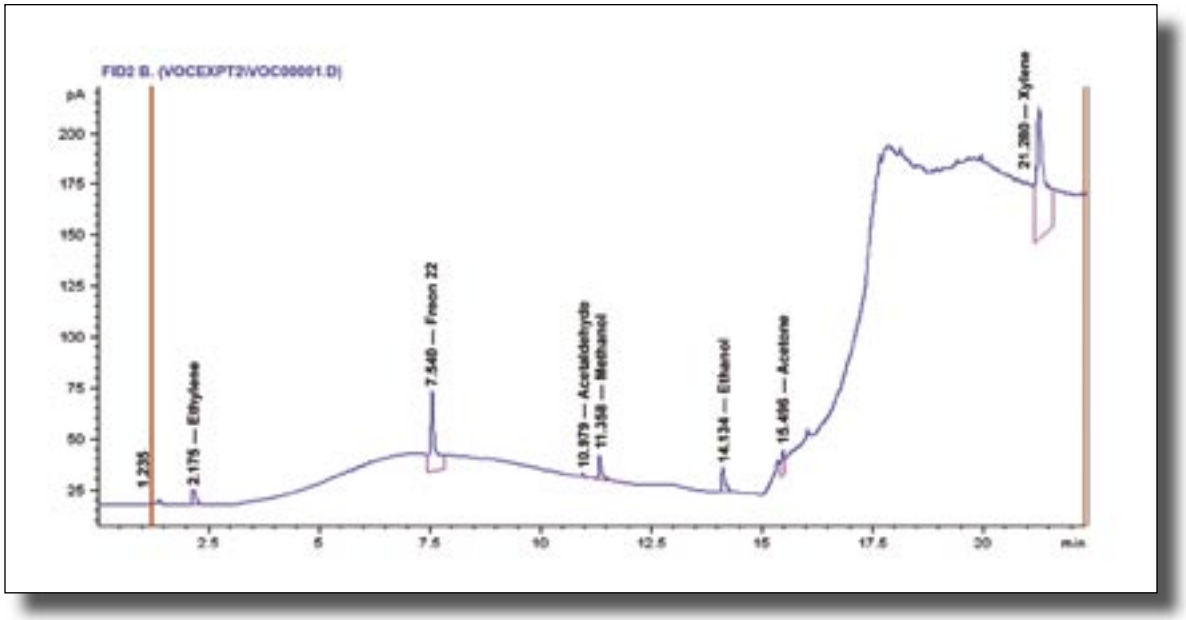

Figure 2. Gas chromatogram (relative intensity versus elution time) of the 10× ISS cabin air mixture used in the filter media characterization tests.

Figure 3. A thermal desorption system and a thermal tube conditioning oven were installed for quantifying amounts of VOCs filtered by vaious adsorbents.

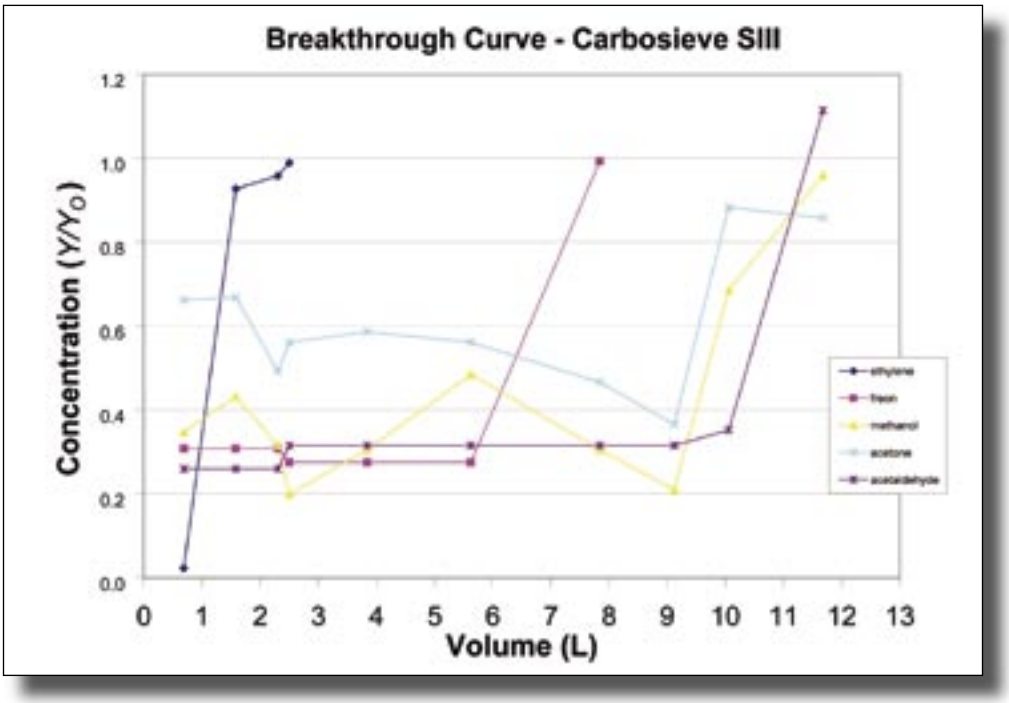

Figure 4. Breakthrough curve for CarboSieve SIII. Ethylene was filtered until 1.5 L of air had passed through the filter. Freon was still adsorbed up to 6 L. Methanol, acetone, and acetaldhyde were adsorbed until 9 L of air had passed through the filter.

Ethylene was found to have the smallest breakthrough volume of the five media tested (Figure 5). The media exhibited differences in how much they filtered; however, the test was conducted with 10 times the concentration to be observed in spacecraft. These results indicate that the capacity of the media to filter ethylene should be used in the filter design because ethylene has a large effect on plant growth. The data in Table 2 were obtained from breakthrough curves for ethylene (Figure 5) depicting Y/Y_O versus the eluted volume. The amount of ethylene removed by each compound at the breakthrough volume (Y_B) is found from $(1–Y_B/Y_O)$ [15]. The breakthrough volume represents the volume of gas required to elute the organic compound off 1.0 g of adsorbent at constant temperature. Table 2 shows that each adsorbent agent has a different chemical specificity for trapping ethylene. Breakthrough curves of individual VOCs in the ISS gas mixture for each adsorbent are shown in Figure 6.

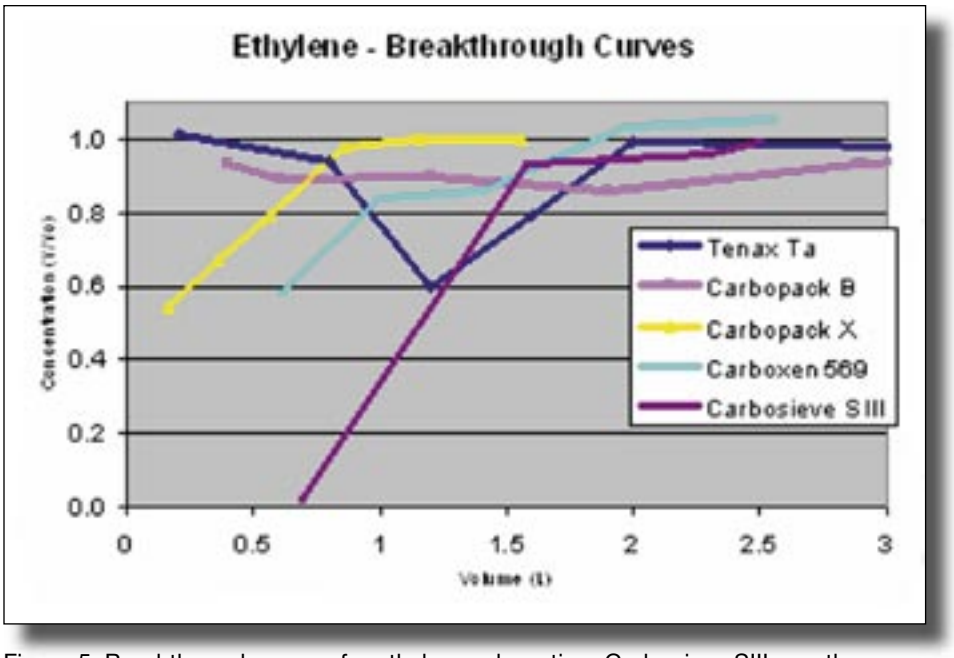

Figure 5. Breakthrough curves for ethylene adsorption. Carbosieve SIII was the most efficient filter media for ethylene; however, it has a small breakthrough volume.

Table 2. Characteristics of adsorbents selected for filtering ethylene.

Adsorbent Type	Adsorbent	Mesh	Density (g/cm^3)	Surface Area (m^2/g)	$1–Y_B/Y_O$	Breakthrough Volume (L/g)
Porous Polymer	Tenax TA	60/80	0.28	35	0.40	24.0
Graphitized Carbon	CarboPack B	60/80	0.43	100	0.20	16.0
	Carbopack X	60/80	0.58	240	0.50	1.4
Carbon Molecular Sieve	Carboxen 569	20/45	0.61	485	0.40	5.9
	Carbosieve SIII	60/80	0.76	820	0.98	5.4

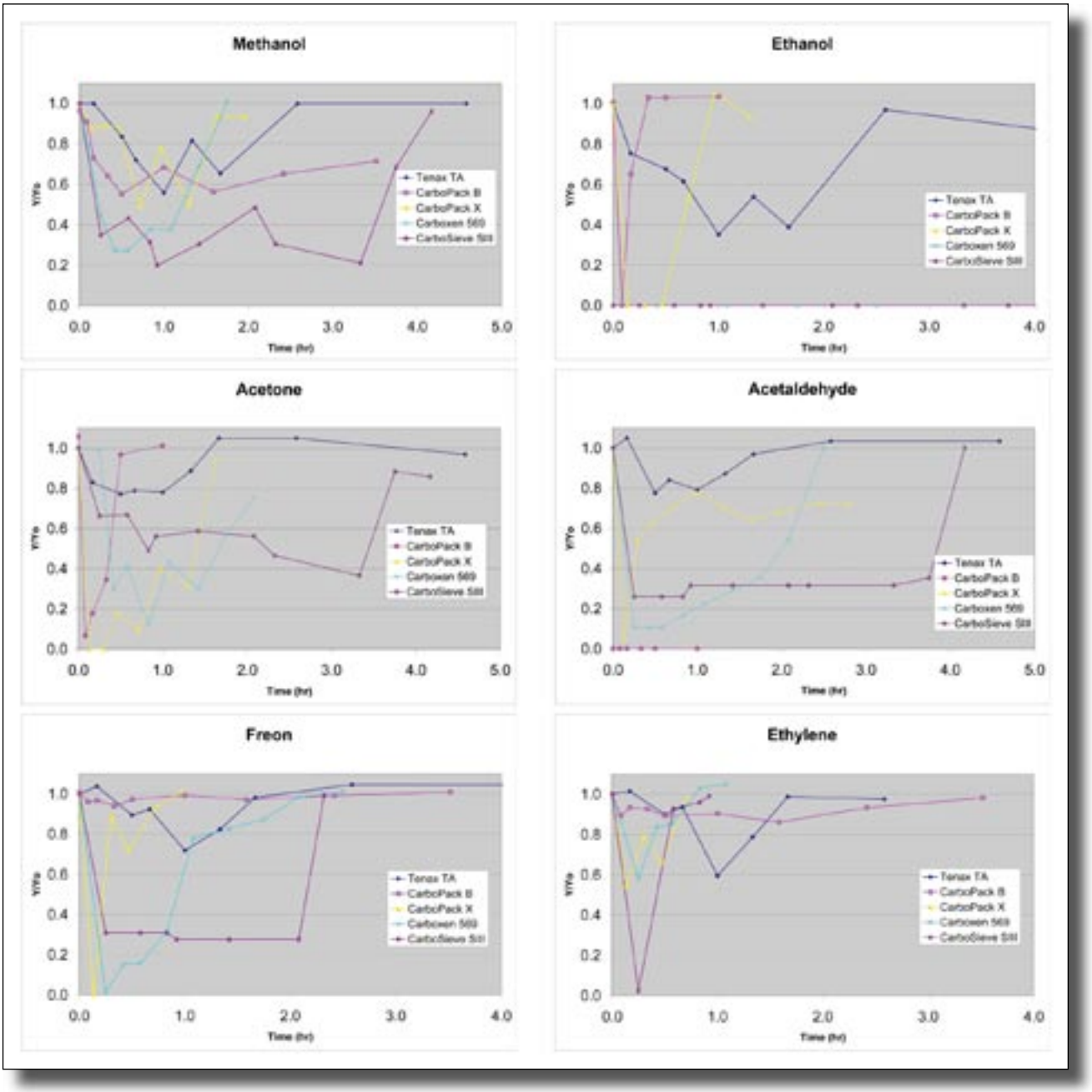

Figure 6. Breakthrough curves for methanol, ethanol, acetone, acetaldehyde, Freon 22, and ethylene were obtained for each of the thermally desorbing compounds. This figure shows that certain adsorbents are better filters than others for the same VOC.

Outreach

The VOC Filter Cartridge project participated in the 2004 Space Life Sciences Training Program (SLSTP) in collaboration with Dr. Gary Stutte (RASTA Flight Experiment) and Gus Koerner (ALS Outreach) (Figure 7). Two students, Charles M. Stinson III, from Jacksonville State University, and Justin Batson, from the State University of West Georgia, conducted an experiment to determine the rates of plant-produced VOCs, an important parameter used for sizing the VOC filter. The experiments were conducted in three BPSe chambers.

Figure 7. Space Life Sciences Training Program students harvest radishes exposed to ethylene in BPSe chambers.

BPSe Chambers

The BPSe chambers are prototypes of future VPUs designed to provide low-mass and low-power platforms for growth of salad crops aboard spacecraft. They consist of a fluorescent light cap, expandable Mylar bellows, and a large root tray (area: 0.25 m^2; depth: 10 cm). The light caps use 16 soft-white, 60-W fluorescent bulbs. The BPSe unit frame has a scissor design and can be lowered or raised depending on plant height or desired light level (Figure 8). Two nutrient delivery system (NDS) types, hydroponic and potted plants, were constructed and compared in terms of yield and rates of VOC production. Plant-produced VOCs were detected as soon as 8 days after planting (DAP). The rates of VOC production measured at 21 DAP are shown in Table 3.

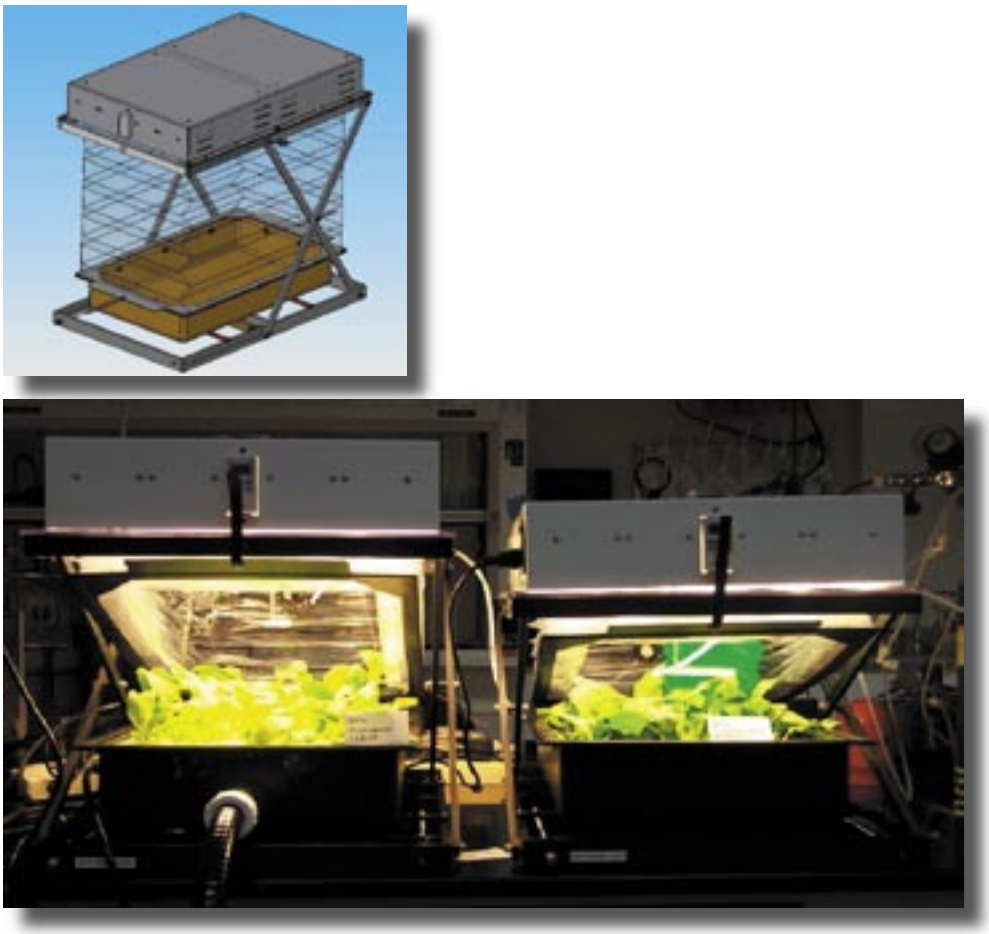

Figure 8. Radish experiment in BPES low-mass chambers.

Table 3. VOC production began after 8 days of growth in the BPSe chambers.

Day	Ethylene	Methanol	Acetaldehyde	Ethanol	Dichloromethane	Acetone
0						
8		×			×	×
12	×	×	×		×	×
21	×	×	×	×	×	×
Production Rate (pmol/g•s)	0.12	3.84	0.04	0.09	1.42	0.28

The production rates (expressed on a dry mass of radish) of selected VOCs were measured at 21 DAP.

VOC Production Rates

The emission rates of production of plant-produced VOCs were measured at 8, 12, and 21 DAP. The measurements were taken in three BPSe low-mass chambers during the 2004 NASA SLSTP. Plants in low-mass chambers introduce VOCs into the ISS Air Revitalization Element because these chambers are vented to cabin air. Thus, identifying the VOCs produced by plants and determining the rates at which these VOCs are produced are important for future designs of low-mass chambers and for reducing risks to spacecraft systems.

Efficacy Testing

For efficacy testing (Figure 9), a prototype reusable ethylene filter (Figure 10) containing 50 g of Carbosieve SIII was used to remove VOCs from a BPSe chamber during a growout of radish (Raphanus sativa) plants (21 DAP). The filter was thermally regenerated every 4 days using a bleed gas technique (N_2 tank supply).

Figure 9. Efficacy testing.

Figure 10. Prototype reusable ethylene filter.

Three BPSe chambers, each containing 37 Cherry Bomb II radish plants, were used to evaluate the filter in a plant growth system. One chamber contained a commercial passive filter (ExtraLife, green disc [Figure 10]), one contained no filter, and one contained the Carbosieve SIII filter (Figure 11). Initially, the leak rate was 63 percent per hour, but in an attempt to lower the relative humidity, the chamber leak rate was increased to 400 percent per hour on day 12. The desorption of the filter was accomplished by a filter regenerator (desorption setup), composed of a heater, a thermostat, a thermocouple, and a tank of N_2 gas (99.99 percent pure) (Figure 12).

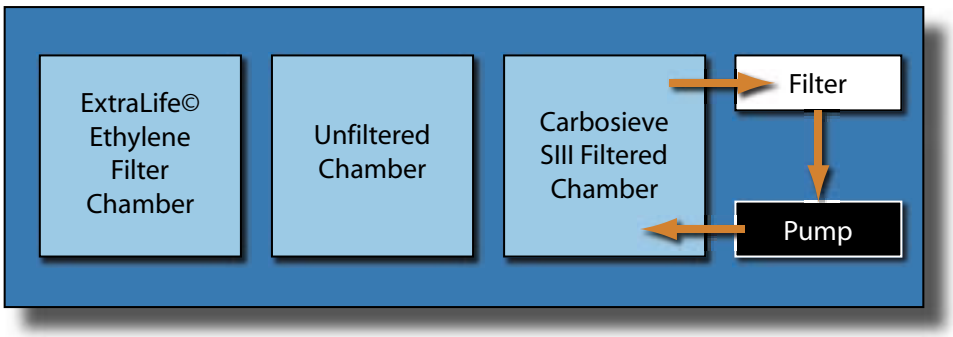

Figure 11. Three BPSe chambers were used in the efficacy testing experiment. In the filtered chamber, a pump pulls the air through the CSIII filter at a rate of 5 mL/min and then returns it to the chamber. The ExtraLife chamber contained four discs of ExtraLife to remove as many VOCs as possible.

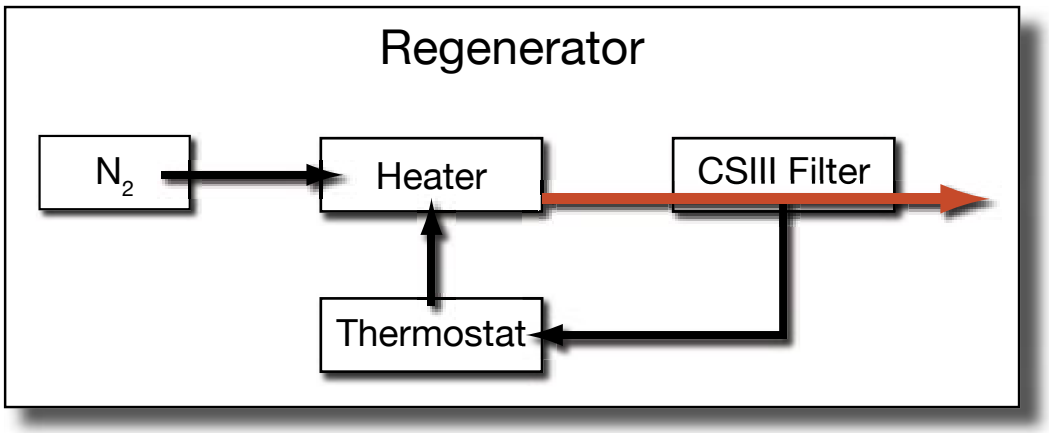

Figure 12. The N_2 gas flows through the heater and filter. The thermostat regulates the temperature of the heater and uses a thermocouple to measure the temperature.

Growth measurements of the radish plants in the three BPSe chambers included dry weight, dimensions, and harvest index. Radish growth in the prototype filter chamber was greater than in the unfiltered chamber and less than in the ExtraLife chamber. These results suggest that the reusable ethylene filter was efficient at reducing the ethylene in the chamber. This experiment should be repeated with a humidity control system added to the BPSe chambers because relative humidities greater than 90 percent were recorded from 12 to 21 DAP. The poor performance of the CarboSieve SIII filter at controlling ethylene-mediated growth reductions, compared to the Purafil-containing ExtraLife discs, may be related to the possibility of reduced filtering capacity of the reusable ethylene filter at such high humidity.

Accomplishments

- Characterized the absorptive properties of five thermally desorbing compounds with seven ISS VOCs.
- Measured the VOC emission rates of radish plants.
- Sized and designed a filter cartridge for controlling VOCs from 0.5-m2 BPSe chambers.
- Organized two laboratories in the Space Life Sciences Laboratory for meeting project requirements.
- Identified several end users of the technology (ALS Plant Element, BioServe, WCSAR, JPL, and Space Dynamics Lab).
- Designed, built, and tested a benchtop system for filter media characterization experiments.
- Developed and optimized procedures for loading desorption tubes and sampling pre- and postfilter gas.
- Optimized and calibrated GC-based methods for sampling and analyzing VOCs from the test system.
- Developed the techniques to measure emission rates of plant-produced VOCs in 0.25 m^2 plant growth chambers.
- Used the emission rates of plant-produced VOCs and the adsorptive properties to select and size a suitable filter to control VOC concentrations in plant growth chambers.
- Designed, constructed, and tested the performance (via thermal desorption) of a prototype reusable ethylene filter.
- Tested the reusable ethylene filter in a 21-day-long plant production experiment (0.25-m^2 radish crop).
- Published and disseminated the findings via presentations at national and international conferences.
- Supported the training of two students during the 2005 NASA SLSTP.
- Compared preflight samples of the Leonardo MPLM, taken before launch of STS-114, with postflight air samples. GC/MS analysis using the TO-15 EPA method (62 compounds) showed very low concentrations of VOCs in the pre- and postflight samples.
- Gathered air samples from four open-top chambers at the SERC CO_2 Site to determine if differences in VOC emissions exist under ambient- and elevated-CO_2 treatments.
- Characterized the performance of an ethylene sensor developed by Giner Inc. under a Small Business Innovative Research Phase III grant. The sensor was found to be temperature-sensitive and to respond to other VOCs: ethanol, methanol, and acetone.

Publications/Presentations

Batson, J., I. Eraso, O.A. Monje, and G.W. Stutte, "Measurement of VOC Production and Assessment of Biophysical Characteristics of Radish in a Biomass Production Chamber," NASA SLSTP student presentations, 2004.

Elmer, J., O. Monje, and J. Williams, "Evaluation of a CarboSieve SIII Filter for Plant Growth in a Closed Chamber," NASA SLSTP poster presentation, NASA Kennedy Space Center, Florida, 2005.

Monje, O., I. Eraso, J. Elmer, J. Williams, and J.C. Sager, "Design and Performance of a Reusable VOC Filter for Atmospheric Control of Biological Payloads aboard Spacecraft," *American Society for Gravitational and Space Biology 21st Annual Meeting*, 2005.

Monje, O., J.T. Richards, I. Eraso, T.P. Griffin, K.C. Anderson, and J.C. Sager, "Designing a Reusable Ethylene Filter Cartridge for Plant Flight Hardware: Characterization of Thermally Desorbing Compounds," SAE Paper 05ICES-256, 2005.

Monje, O., J.T. Richards, I. Eraso, T.P. Griffin, K.C. Anderson, and J.C. Sager, "Designing a Reusable Ethylene Filter Cartridge for Plant Flight Hardware: Characterization of Thermally Desorbing Compounds," *ICES International Conference*, Rome, Italy, 2005.

Monje, O, J.T. Richards, I. Eraso, T.P. Griffin and J.C. Sager, "Measurement of plant-produced volatile organic compounds in controlled environments," *Soil and Crop Science Society of Florida 65th Annual Meeting*, Boca Raton, Florida, 2005.

Stinson, C.M., O.A. Monje, and G.W. Stutte, "Evaluation of Three Candidate Nutrient Delivery Systems for a Portable, Lightweight Plant Growth Chamber," NASA SLSTP student presentation, 2004.

Williams, J., J. Elmer, and O. Monje, "Evaluating a Reusable Filter for Controlling VOCs in Plant Growth Chambers," NASA SLSTP poster presentation, NASA Kennedy Space Center, Florida, 2005.

References

1. R.D. MacElroy, M. Kliss, and C. Straight, "Life support systems for Mars transit," *Advances in Space Research,* Vol. 12, No. 5, 1992, pp. 159–166.
2. A.J. Hanford, M.K. Ewert, and D.L. Henninger, "ALS Baseline Values and Assumptions Document (BVAD)," Document No. CTSD-ADV-484, Crew and Thermal Systems Division, National Aeronautics and Space Administration, Lyndon B. Johnson Space Center, Houston, Texas, 2002.
3. O. Monje, G.W. Stutte, G.D. Goins, D.M. Porterfield, and G.E. Bingham, "Farming in space: environmental and biophysical concerns," *Advances in Space Research,* Vol. 31, 2003, pp. 151–167.
4. J.L. James, T.F. Limero, H.J. Leano, J.F. Boyd, and P.A. Covington, "Volatile organic contaminants found in the habitable environment of the Space Shuttle: STS-26 to STS-55," *Aviat. Space Environ. Med.,* Vol. 65, 1994, pp. 851–857.
5. G.W. Stutte and R.M. Wheeler, "Accumulation and effect of volatile organic compounds in closed life support systems," *Advances in Space Research,* Vol. 20, 1997, pp. 1913–1922.
6. R.M. Wheeler, B.V. Peterson, J.C. Sager, and W.M. Knott, "Ethylene production by plants in closed environments," *Advances in Space Research,* Vol. 18, 1996, pp. 193–196.
7. R.M. Wheeler, J.C. Sager, R.P. Prince, W.M. Knott, C.L. Mackowiak, G.W. Stutte, N.C. Yorio, L.M. Ruffe, B.V. Peterson, G.D. Goins, C.R. Hinkle, and W.L. Berry, "Crop Production for Advanced Life Support Systems – Observations From the Kennedy Space Center Breadboard Project," NASA Technical Memorandum 2003-211184, 2003.
8. Jay Perry, personal communication, n.d.
9. F.B. Salisbury, "Growing Super-Dwarf wheat in space station Mir," *Life Support and Biosphere Science,* Vol. 4, 1997, pp. 155–166.
10. S. Klassen and B. Bugbee, "Sensitivity of wheat and rice to low levels of atmospheric ethylene," *Crop Sci.,* Vol. 42, 2002, pp. 746–753.
11. I. Eraso, G.W. Stutte, B.V. Peterson, and E.C. Stryjewski, "Effects of ethylene on the growth and development of radish," *Proc. Plant Growth Regulation of America,* Miami Beach, Florida, Vol. 28, 2001, pp. 118–123.
12. F.B. Abeles, P.W. Morgan, and M.S. Saltveit, Jr., *Ethylene in Plant Biology*, Academic Press, New York, 1992.
13. I. Eraso, G.W. Stutte, and E.C. Stryjewski, "Chronic exposure to ethylene induced stress symptoms in radish," in M. Vendrell et al. (eds.), *Biology and Biotechnology of the Plant Hormone Ethylene III,* IOS Press, 2003.
14. J.L. Perry, R.E. Curtis, K.L. Alexandre, L.L. Ruggiero, and N. Shtessel, "Performance Testing of a Trace Contaminant Control Subassembly for the International Space Station," SAE 981621, *Society of Automotive Engineers: 28th International Conference on Environmental Systems,* July 1998.
15. E.L. Cussler, *Diffusion, Mass Transfer in Fluid Systems*, 2nd ed., Cambridge University Press, 1997.

Planned Future Work

The CDDF-funded VOC Filter Cartridge project has been characterizing the chemical specificity of several COTS regenerable adsorbents for use in trace contaminant control technologies on nonmethane VOCs aboard spacecraft, such as CEV. The polymeric adsorbents studied complement a suite of other candidate filter media for use in CEV (e.g., regenerable amines, zeolites, activated carbon, CO catalysts, and chemisorbents). Future work will be directed toward evaluating the dynamic performance of these polymeric adsorbents so they can be evaluated for use in CEV air revitalization systems. An outline of proposed future work has been submitted to the Exploration System Mission Directorate – Applied Technology Development Division for funding and includes the following tasks:

- determining single-component capacity data,
- determining multicomponent capacity data,
- determining the effects of humidity on capacity,
- determining dynamic working capacity (i.e., regeneration duration),
- determining the kinetics of regeneration under both vacuum and thermal swing regeneration, and
- generating the appropriate data for sizing a trace contaminant control bed.

Aggregate Amount of Funding Authorized in FY 2004 and Earlier Years: $97K

Funding Authorized for FY 2005: $85K

Completion Date: March 2006

Center Director's Discretionary Fund Distribution for FY 2005	
Project	Authorized ($K)
Capacitance-Based Moisture Sensing	65.0
Commodity-Free Calibration	60.0
Application of Glow Discharge Plasma To Alter the Surface Properties of Materials	117.0
Extraction of Lead Compounds for Remediation of Lead-Based Paint	123.0
Development of Focused Metabolite Profiling Capability for Dissecting Cellular and Molecular Processes of Living Organisms in Space Environments	140.0
Physics of Rocket Exhaust Cratering	100.0
Smart Coatings for Corrosion Sensing and Protection	85.0
Model for Software Quality Diagnosis and Prognosis	10.0
Formulation of Specialty Polymeric Materials for Electrostatic Dissipation and Flame Retardancy	125.5
Electrostatic Method of Surface Charge Measurement	40.0
VOC Filter Cartridge for Biological Experiments in Space	85.0
Total CDDF Funding Allocated in FY 2005	950.5

National Aeronautics and Space Administration

John F. Kennedy Space Center
Kennedy Space Center, FL 32899
www.nasa.gov/centers/kennedy

www.nasa.gov

NASA Technical Publication 2007-214731